

# **Advanced Characterization of Photovoltaic Modules using Photoluminescence**

**Raghavi Bhoopathy**

A thesis in fulfilment of the requirements for the degree of  
Doctor of Philosophy



School of Photovoltaic and Renewable Energy Engineering  
Faculty of Engineering

November 2020



# Thesis/Dissertation Sheet

|  |   |
|--|---|
| Surname/Family Name  | : Bhoopathy   |
| Given Name/s   | : Raghavi   |
| Abbreviation for degree as give in the University calendar | : PhD   |
| Faculty  | : Engineering   |
| School   | : Photovoltaics and Renewable Energy Engineering                            |
| Thesis Title   | : Advanced characterization of photovoltaic modules using photoluminescence |

## Abstract 350 words maximum: (PLEASE TYPE)

Photovoltaic modules are prone to degradation during transportation, installation and operation. To operate photovoltaic power plants at maximum capacity, it is desirable to identify module failures in the **field** at the earliest possible stage.

Currently used field inspection methods cannot detect many types of faults that can have a significant impact on the extracted power from the module. Photoluminescence imaging is a very powerful characterization method that can provide high resolution spatially resolved information of cells and modules in a contactless manner. However, to date, one of the main challenges associated with luminescence-based **outdoor** module inspection is the detection of the weak luminescence signal from the much stronger ambient sunlight signal. This thesis presents the **first-ever** photoluminescence imaging system developed to characterize photovoltaic modules in full sunlight. The proposed methods overcome this challenge without any modification to the photovoltaic system. To achieve this, the proposed methods use an appropriate choice of optical filtering and modulation of the module between the normal operating point and open circuit condition. The modulation is performed by periodically changing the optical generation rate of at least one cell within the module. This changes the biasing condition of all other cells that are connected to the same bypass diode. The methods have the advantage that it can deliver high-quality images revealing faults in individual cell and the entire module, without requiring any changes to the electrical connections of the photovoltaic system.

To further investigate the cause of degradation, current-voltage measurements of individual solar cells in a degraded module can be used to obtain accurate information regarding the nature of degradation, leading to a detailed understanding of the underlying detrimental recombination mechanisms. However, non-destructive current-voltage measurement of individual cells in a module is currently very challenging. This thesis also addresses this challenge by developing a contactless and non-destructive method that is based on Suns-photoluminescence measurements to extract the current-voltage parameters under operating conditions in the field. The main advantages of the developed technique include its low cost and its fast and easy applicability.

The developed methods have the potential to revolutionise the traditional field inspection methods thereby enhancing the operations and maintenance of photovoltaic power plants.

## Declaration relating to disposition of project thesis/dissertation

I hereby grant to the University of New South Wales or its agents a non-exclusive licence to archive and to make available (including to members of the public) my thesis or dissertation in whole or in part in the University libraries in all forms of media, now or here after known. I acknowledge that I retain all intellectual property rights which subsist in my thesis or dissertation, such as copyright and patent rights, subject to applicable law. I also retain the right to use all or part of my thesis or dissertation in future works (such as articles or books).

.....  
Signature

.....  
Date

The University recognises that there may be exceptional circumstances requiring restrictions on copying or conditions on use. Requests for restriction for a period of up to 2 years can be made when submitting the final copies of your thesis to the UNSW Library. Requests for a longer period of restriction may be considered in exceptional circumstances and require the approval of the Dean of Graduate Research.

## ORIGINALITY STATEMENT

‘I hereby declare that this submission is my own work and to the best of my knowledge it contains no materials previously published or written by another person, or substantial proportions of material which have been accepted for the award of any other degree or diploma at UNSW or any other educational institution, except where due acknowledgement is made in the thesis. Any contribution made to the research by others, with whom I have worked at UNSW or elsewhere, is explicitly acknowledged in the thesis. I also declare that the intellectual content of this thesis is the product of my own work, except to the extent that assistance from others in the project’s design and conception or in style, presentation and linguistic expression is acknowledged.’

Signed: \_\_\_\_\_

Date: \_\_\_\_\_



## INCLUSION OF PUBLICATIONS STATEMENT

UNSW is supportive of candidates publishing their research results during their candidature as detailed in the UNSW Thesis Examination Procedure.

**Publications can be used in their thesis in lieu of a Chapter if:**

- The candidate contributed greater than 50% of the content in the publication and is the “primary author”, ie. the candidate was responsible primarily for the planning, execution and preparation of the work for publication
- The candidate has approval to include the publication in their thesis in lieu of a Chapter from their supervisor and Postgraduate Coordinator.
- The publication is not subject to any obligations or contractual agreements with a third party that would constrain its inclusion in the thesis

Please indicate whether this thesis contains published material or not:

☐

This thesis contains no publications, either published or submitted for publication  
*(if this box is checked, you may delete all the material on page 2)*

☒

Some of the work described in this thesis has been published and it has been documented in the relevant Chapters with acknowledgement  
*(if this box is checked, you may delete all the material on page 2)*

☐

This thesis has publications (either published or submitted for publication) incorporated into it in lieu of a chapter and the details are presented below

### CANDIDATE'S DECLARATION

I declare that:

- I have complied with the UNSW Thesis Examination Procedure
- where I have used a publication in lieu of a Chapter, the listed publication(s) below meet(s) the requirements to be included in the thesis.

| Candidate's Name | Signature | Date (dd/mm/yy) |
|------------------|-----------|-----------------|
|                  |           |                 |

## COPYRIGHT STATEMENT

‘I hereby grant the University of New South Wales or its agents the right to archive and to make available my thesis or dissertation in whole or part in the University libraries in all forms of media, now or here after known, subject to the provisions of the Copyright Act 1968. I retain all proprietary rights, such as patent rights. I also retain the right to use in future works (such as articles or books) all or part of this thesis or dissertation.

I also authorise University Microfilms to use the 350 word abstract of my thesis in Dissertation Abstracts International (this is applicable to doctoral theses only).

I have either used no substantial portions of copyright material in my thesis or I have obtained permission to use copyright material; where permission has not been granted I have applied/will apply for a partial restriction of the digital copy of my thesis or dissertation.’

Signed: \_\_\_\_\_

Date: \_\_\_\_\_

## AUTHENTICITY STATEMENT

‘I certify that the Library deposit digital copy is a direct equivalent of the final officially approved version of my thesis. No emendation of content has occurred and if there are any minor variations in formatting, they are the result of the conversion to digital format.’

Signed: \_\_\_\_\_

Date: \_\_\_\_\_

This thesis is dedicated to my beloved parents

*Vijaya and Bhoopathy*

for their constant support throughout my entire academic career



# Acknowledgement

I gracefully consider this opportunity to express my indebtedness towards my supervisors: Ziv Hameiri, Oliver Kunz and Thorsten Trupke. Thank you, Ziv, for your motivation and patience. During our numerous meetings throughout my PhD, you always made sure that I leave with a big smile. Thank you for motivating me in every step and encouraging me not to be afraid to fail. I was amazed to see how you always made yourself available whenever I asked for a meeting despite your busy schedule. You will always be my role model for your passion, sincerity and dedication towards saving the world. Thank you, Oli, for being more than a supervisor. From day one, you have guided and equipped me with numerous skills right from soldering to using an electric hand-saw and molding me into what I am today. Starting from almost having no knowledge in this field, I simply cannot imagine finishing my PhD without your help and guidance. Thank you for your insightful suggestions whenever progress took a toll. More than everything, your words of wisdom on life, in general, helped me sail through this challenging journey of PhD. Thank you, Thorsten, for your constant support and encouragement. Your honest and constructive feedback on my work has played an instrumental role in my intellectual growth.

Thank you, Harsh Parikh, for your contribution to the signal to noise analysis studies in Chapter 4 and for keeping up the Indian connection. It was fun performing the experiments with you. I would also like to thank the entire PL group at UNSW for their fruitful discussions and suggestions. A special mention to Mattias for the brainstorming sessions during the initial days of my PhD. A special thanks to my mates from the AC-DC group. Thank you, Germain Rey, Rhett Evans, Yan Zhu, Yoann Buratti for proof-reading this thesis and providing valuable comments. Thanks to Pei-Chieh Hsia for helping me generously to fabricate the mini-modules used in this thesis. I would like to thank Ly Mai, Alex Kirichenko, Nino Borojevic and others from Solar Industrial

## Acknowledgement

Research Facility team for their help. Thanks to the lab development and operation team and the administrative teams at SPREE for ensuring an amazing research experience.

I would like to take this opportunity to thank my friends in Sydney: Giti, Sharad, Sweta, Suvigya, Vishal, Laxmi, Sumit, Saloni, Shekhar, Ruchira, Bhanu, Rammy, Maithily, Vaishnavi, Anisha, Yashoda, Chhaya and the entire Aikido club at UNSW. All of you made me eagerly look forward to weekends and holidays. A special thanks to the entire Art of Living community in Sydney.

I am forever grateful to my parents for their consistent support and love throughout my life. Shantanu, you are the man behind this thesis. There would not have been a better person than you who could exactly understand what I was going through and thank you for giving your shoulders to lean on at difficult times.

I finally bow down to the feet of my beloved Guru for all the blessings bestowed upon me which made this thesis see the light of day. Jai Gurudev!

# Contents

|   |            |
|---|------------|
| <b>Acknowledgement.....</b>                       | <b>ix</b>  |
| <b>Contents .....</b>                             | <b>xi</b>  |
| <b>Abbreviations and Symbols.....</b>             | <b>xiv</b> |
| Abbreviations.....                                | xiv        |
| Symbols .....                                     | xvi        |
| <b>Abstract.....</b>                              | <b>xix</b> |
| <b>List of publications.....</b>                  | <b>xxi</b> |
| Journal publications.....                         | xxi        |
| Conference publications .....                     | xxi        |
| <b>Chapter 1 Introduction.....</b>                | <b>25</b>  |
| 1.1 Motivation.....                               | 25         |
| 1.2 Thesis objectives .....                       | 27         |
| 1.3 Thesis outline .....                          | 28         |
| <b>Chapter 2 Background and Review .....</b>      | <b>31</b>  |
| 2.1 Photovoltaic system.....                      | 31         |
| 2.1.1 Photovoltaic technologies.....              | 31         |
| 2.1.2 Photovoltaic module components .....        | 32         |
| 2.1.3 Photovoltaic inverters.....                 | 33         |
| 2.2 Degradation in fielded modules .....          | 34         |
| 2.2.1 Discoloration.....                          | 34         |
| 2.2.2 Delamination and corrosion.....             | 35         |
| 2.2.3 Interconnect failure .....                  | 35         |
| 2.2.4 Defective bypass diode.....                 | 36         |
| 2.2.5 Hotspots.....                               | 37         |
| 2.2.6 Cell cracking.....                          | 37         |
| 2.2.7 Potential induced degradation.....          | 39         |
| 2.2.8 Light and carrier induced degradation ..... | 40         |
| 2.3 Basic module inspection techniques.....       | 41         |
| 2.3.1 Visual inspection.....                      | 41         |

|  |           |
|--|-----------|
| 2.3.2 Current-voltage measurements .....   | 42        |
| 2.4 Imaging-based module inspection techniques.....                                      | 43        |
| 2.4.1 Ultraviolet fluorescence imaging .....   | 43        |
| 2.4.2 Infrared thermography.....   | 44        |
| 2.4.3 Luminescence imaging.....  | 46        |
| 2.5 Extracting the current voltage characteristics of individual cells in a module ..... | 52        |
| 2.5.1 Techniques based on LBIC.....  | 53        |
| 2.5.2 Techniques based on shading .....  | 53        |
| 2.5.3 Techniques using electroluminescence or infrared imaging .....                     | 54        |
| 2.6 Chapter summary.....   | 55        |
| <b>Chapter 3 Outdoor photoluminescence imaging .....</b>                                 | <b>57</b> |
| 3.1 Methodology .....  | 57        |
| 3.2 Proof of concept .....   | 60        |
| 3.3 Development of imaging system .....  | 63        |
| 3.4 Outdoor photoluminescence image .....  | 67        |
| 3.5 Bypass diode failure inspection using PL emission .....                              | 69        |
| 3.5.1 Modelling.....   | 69        |
| 3.5.2 Experiment.....  | 72        |
| 3.6 Impact of module-level power electronics.....  | 74        |
| 3.7 Chapter summary.....   | 77        |
| <b>Chapter 4 Batch measurement of outdoor photoluminescence imaging.....</b>             | <b>79</b> |
| 4.1 Methodology .....  | 79        |
| 4.2 Comparison between sequential and batch measurement.....                             | 81        |
| 4.3 Determination of camera noise parameters.....  | 85        |
| 4.4 Determination of SNR for outdoor PL images.....                                      | 92        |
| 4.5 Impact of different factors on outdoor PL image quality .....                        | 94        |
| 4.5.1 Impact of incident sunlight intensity .....  | 94        |
| 4.5.2 Impact of cell open-circuit voltage .....  | 97        |
| 4.5.3 Control cell shunt resistance .....  | 100       |
| 4.6 Comparison between outdoor PL and conventional EL imaging.....                       | 104       |
| 4.7 Local series resistance quantification .....   | 107       |
| 4.8 Solar car imaging.....   | 113       |
| 4.9 Application in Solar farms .....   | 115       |
| 4.10 Chapter summary.....  | 116       |



|   |            |
|---|------------|
| <b>Chapter 5 Implied current-voltage measurements of individual cells in a module</b> | <b>119</b> |
| 5.1 Introduction .....  | 120        |
| 5.2 Methodology .....   | 120        |
| 5.3 Calibration procedure .....   | 121        |
| 5.3.1 Suns-PL curves .....  | 121        |
| 5.3.2 Luminescence imaging .....  | 122        |
| 5.4 Experimental setup .....  | 123        |
| 5.5 Results and Discussion .....  | 125        |
| 5.5.1 Comparison between calibration methods.....                                     | 125        |
| 5.5.2 Indoor measurements .....   | 127        |
| 5.5.3 Outdoor measurements.....   | 134        |
| 5.5.4 Impact of temperature .....   | 139        |
| 5.6 Conclusions .....   | 140        |
| <b>Chapter 6 Summary and future works .....</b>                                       | <b>143</b> |
| 6.1 Summary .....   | 143        |
| 6.2 Contributions.....  | 145        |
| 6.3 Future works.....   | 146        |
| 6.4 Final remarks.....  | 147        |
| <b>References .....</b>   | <b>149</b> |

## Abbreviations and Symbols

### Abbreviations

|       |                                |
|-------|--------------------------------|
| PV    | Photovoltaics                  |
| PL    | Photoluminescence              |
| OC    | Open circuit                   |
| BPD   | Bypass diode                   |
| LID   | Light induced degradation      |
| PID   | Potential induced degradation  |
| MPPT  | Maximum power point tracking   |
| I-V   | Current-voltage                |
| Si    | Silicon                        |
| c-Si  | Monocrystalline silicon        |
| mc-Si | Multicrystalline silicon       |
| EVA   | Ethylene vinyl acetate         |
| DC    | Direct current                 |
| AC    | Alternating current            |
| MLPE  | Module level power electronics |
| MPP   | Maximum power point            |
| SC    | Short circuit                  |

|         |                                     |
|---------|-------------------------------------|
| IR      | Infrared                            |
| STD     | Signal Transmission Device          |
| EL      | Electroluminescence                 |
| CID     | Carrier induced degradation         |
| BO      | Boron-oxygen                        |
| FeB     | Iron-boron                          |
| FF      | Fill factor                         |
| UV      | Ultraviolet                         |
| LIT     | Loc-in thermography                 |
| SNR     | Signal to noise ratio               |
| VIM     | Voltage imaging of the PV module    |
| DSLR    | Digital single-lens reflex camera   |
| InGaAs  | Indium gallium arsenide             |
| LBIC    | Laser beam induced current          |
| li-LBIC | Limiting laser beam induced current |
| DLIT    | Dark lock-in thermography           |
| OP      | Operating point                     |
| RMS     | Root mean square                    |
| LED     | Light emitting diode                |
| PERC    | Passivated emitter and rear cell    |
| Al-BSF  | Aluminium back-surface field        |
| ICF     | Intensity correction factor         |

## Abbreviations and Symbols

|     |                               |
|-----|-------------------------------|
| SNR | Signal to noise ratio         |
| ADC | Analogue-to-digital converter |

## Symbols

|                   |  |
|-------------------|--|
| $R_s$             | Series resistance  |
| $V_{oc}$          | Open circuit voltage   |
| $R_{sh}$          | Shunt resistance   |
| $J_{02}$          | Saturation current of the second diode in the two-diode model, responsible for the recombination in the depletion region |
| $I_{sc}$          | Short-circuit current  |
| $\eta$            | Efficiency   |
| $\varphi$         | Photon flux of luminescence emission   |
| $V$               | Terminal voltage   |
| $C$               | Proportionality constant   |
| $V_T$             | Thermal voltage  |
| $k$               | Boltzmann constant   |
| $q$               | Elementary charge  |
| $T$               | Temperature  |
| $\varphi_i^{max}$ | Maximum luminescence intensity of the $i^{\text{th}}$ cell within a module   |
| $N_{cell}$        | Total number of cells in the module  |
| $V_{mod}$         | Module terminal voltage  |
| $J_{01}$          | Saturation current of the first diode in the two-diode model, responsible for the diffusion current component            |

|                  |   |
|------------------|---|
| $J_0$            | Saturation current of a solar cell  |
| $I_{MPP}$        | MPP current of a solar cell   |
| $I_{MPP,system}$ | MPP current of a PV system  |
| $I_{sc,control}$ | Short-circuit current of the control cell   |
| $S_{OC}$         | Spectral intensity measured at open circuit   |
| $S_{SC}$         | Spectral intensity measured at short circuit  |
| $S_t$            | Average pixel count of all the captured images after subtracting the camera bias offset |
| $\sigma_{ro}$    | Readout noise   |
| $\sigma_s$       | Shot noise  |
| $\Phi_s$         | Flux resulting from the sample intensity  |
| $t_{exp}$        | Exposure time   |
| $\sigma_d$       | Dark noise  |
| $\Phi_d$         | Flux resulting from the thermal electrons created in the sensor                         |
| $\sigma_{diff}$  | Variance of the difference image  |
| $G$              | Camera gain   |
| $S_o$            | Camera offset bias  |
| $A_i$            | Fraction of the area of the isolated region relative to the overall cell area           |
| $iV_{oc}$        | Implied open circuit voltage  |
| $\varphi_{PL}$   | Photon flux of photoluminescence emission   |
| $M$              | Number of measured cells in the string  |
| $N$              | Total number of cells in the string   |

## Abbreviations and Symbols

|                    |   |
|--------------------|---|
| $\varphi_i$        | Integrated PL intensity of the $i^{th}$ cell  |
| $\bar{\Phi}_{1-M}$ | Average PL intensity of all the measured cells (from 1 to $M$ ) at the same illumination                                      |
| $V_{oc,string}$    | String open-circuit voltage   |
| $V_{oc,module}$    | Module open-circuit voltage   |
| $V_{mod}$          | Module terminal voltage   |
| $J$                | Terminal current density  |
| $J_L$              | Light-generated current density   |
| $m$                | Ideality factor   |
| $2Dfit$            | Two-diode model fit   |
| $3Dfit$            | Three-diode model fit   |
| $J_{0H}$           | Saturation current of the third diode in the three-diode model, responsible for the resistance limited enhanced recombination |

## Abstract

Photovoltaic modules are prone to degradation during transportation, installation and operation. To operate photovoltaic power plants at maximum capacity, it is desirable to identify module failures in the **field** at the earliest possible stage.

Currently used field inspection methods cannot detect many types of faults that can have a significant impact on the extracted power from the module. Photoluminescence imaging is a very powerful characterization method that can provide high resolution spatially resolved information of cells and modules in a contactless manner. However, to date, one of the main challenges associated with luminescence-based **outdoor** module inspection is the detection of the weak luminescence signal from the much stronger ambient sunlight signal. This thesis presents the **first-ever** photoluminescence imaging system developed to characterize photovoltaic modules in full sunlight. The proposed methods overcome this challenge without any modification to the photovoltaic system. To achieve this, the proposed methods use an appropriate choice of optical filtering and modulation of the module between the normal operating point and open circuit condition. The modulation is performed by periodically changing the optical generation rate of at least one cell within the module. This changes the biasing condition of all other cells that are connected to the same bypass diode. The methods have the advantage that it can deliver high-quality images revealing faults in individual cell and the entire module, without requiring any changes to the electrical connections of the photovoltaic system.

To further investigate the cause of degradation, current-voltage measurements of individual solar cells in a degraded module can be used to obtain accurate information regarding the nature of degradation, leading to a detailed understanding of the underlying detrimental recombination mechanisms. However, non-destructive current-voltage measurement of individual cells in a module is currently very challenging. This thesis also addresses this challenge by developing a contactless and non-destructive method that is based on Suns-photoluminescence measurements to extract the current-voltage

## Abstract

parameters under operating conditions in the field. The main advantages of the developed technique include its low cost and its fast and easy applicability.

The developed methods have the potential to revolutionise the traditional field inspection methods thereby enhancing the operations and maintenance of photovoltaic power plants.



## List of publications

### Journal publications

1. **Bhoopathy, R.**, Kunz, O., Juhl, M., Trupke, T. and Hameiri, Z., 2018. Outdoor photoluminescence imaging of photovoltaic modules with sunlight excitation. *Progress in Photovoltaics: Research and Applications*, 26(1), pp.69-73. **(Awarded Top Downloaded Article 2017-2018 Certificate by WILEY publication)**
2. **Bhoopathy, R.**, Kunz, O., Juhl, M., Trupke, T. and Hameiri, Z., 2019. Outdoor photoluminescence imaging of solar panels by contactless switching: Technical considerations and applications. *Progress in Photovoltaics: Research and Applications*, 28(3), pp.217-228. **(Featured article on the front cover of the journal in March 2020 issue).**
3. **Bhoopathy, R.**, Kunz, O., Dumbrell, R., Trupke, T. and Hameiri, Z., 2020. Outdoor implied current-voltage measurements of an individual encapsulated cell in a module. *IEEE Journal of Photovoltaics*. **(Accepted for publication in the next issue)**
4. **Bhoopathy, R.**, Parikh, H.R., Rey, G., Kunz, O., Spataru, S., Kerekes, T., DezsoSera, Trupke, T. and Hameiri, Z., 2020. Evaluation of image quality for outdoor luminescence imaging techniques. **(Under internal review; Equal contribution with Parikh, H.R.)**

### Conference publications

1. **Bhoopathy, R.**, Kunz, O., Juhl, M., Trupke, T. and Hameiri, Z., 2017, Outdoor photoluminescence measurements of photovoltaic modules under full sunlight illumination. In *27th International Photovoltaic Science and Engineering Conference*.
2. Hameiri, Z., **Bhoopathy, R.**, Kunz, O., Zafirovska, I., Juhl, M., Trupke, T., 2018. Outdoor and indoor luminescence imaging of photovoltaic modules. In *Photovoltaic Reliability Workshop*.

3. Hameiri, Z., **Bhoopathy, R.**, Chung, D., Dumbrell, R., Juhl, M., Kunz, O., Lee Chin, R., Paduthol, A., Zafirovska, I., Zhu, Y. and Trupke, T., 2018. Progress in photoluminescence-based characterisation of silicon bricks, wafers and modules. In *European Advanced Energy Materials and Technology Congress*.
4. **Bhoopathy, R.**, Kunz, O., Dumbrell, R., Trupke, T. and Hameiri, Z., 2018. Contactless extraction of implied I-V curves of individual solar cells in fully assembled modules using photoluminescence. In *7th World Conference on Photovoltaic Energy Conversion* (pp. 3578-3602).
5. **Bhoopathy, R.**, Kunz, O., Juhl, M., Trupke, T. and Hameiri, Z., 2018. Inspecting series resistance effects and bypass diode failure using contactless outdoor photoluminescence imaging. In *7th World Conference on Photovoltaic Energy Conversion* (pp. 0377-0380). **(This study won the Best Poster Award)**
6. **Bhoopathy, R.**, Kunz, O., Juhl, M., Trupke, T. and Hameiri, Z., 2018. Photoluminescence based characterization techniques for photovoltaic modules in the field. In *28th Annual NREL Silicon Workshop*. **(Invited talk)**
7. **Bhoopathy, R.**, Kunz, O., Juhl, M., Trupke, T. and Hameiri, Z., 2018. Photoluminescence imaging of field deployed modules using contactless switching. In *Asia Pacific Solar Research Conference*. **(Invited talk)**
8. **Bhoopathy, R.**, Kunz, O., Juhl, M., Trupke, T. and Hameiri, Z., 2019. A simplified contactless method for outdoor photoluminescence imaging. In *46th IEEE Photovoltaic Specialists Conference* (pp. 2571-2574). **(This study was selected as Best Student Award Finalist)**
9. **Bhoopathy, R.**, Kunz, O., Dumbrell, R., Trupke, T. and Hameiri, Z., 2019. Application of suns-photoluminescence to extract implied I-V curves of individual cells in modules installed in the field. In *36th European Photovoltaic Solar Energy Conference and Exhibition*.
10. Zhang, S., **Bhoopathy, R.**, Gentle, A., and Hameiri, Z., 2019. Investigation of the temperature dependence of the optical properties of silicon nitride anti-reflection coating on silicon photovoltaic modules. In *36th European Photovoltaic Solar Energy Conference and Exhibition*.

11. Zhang, S., **Bhoopathy, R.**, Gentle, A., and Hameiri, Z., 2019. Investigation of the temperature dependence of the optical properties of silicon nitride anti-reflection coatings. In *Asia Pacific Solar Research Conference*.
12. **Bhoopathy, R.**, Kunz, O., Dumbrell, R., Trupke, T. and Hameiri, Z., 2019. Outdoor non-contact measurement of pseudo I-V curves of solar cells in a module. In *Asia Pacific Solar Research Conference*.
13. Jordan, D.C., Sulas-Kern, D.B., Johnston, S., Moutinho, H.R., Xiao, C., Young, M., Deline, C., Repins, I., **Bhoopathy, R.**, Kunz, O., Dumbrell, R., Trupke, T. and Hameiri, Z., Sainsbury, C., Sinha, A., Schelhas, L., 2020. High efficiency module degradation – from atoms to systems. In *37th European Photovoltaic Solar Energy Conference and Exhibition*.



# Chapter 1

## Introduction

### 1.1 Motivation

We live in the age of anthropogenic (human-induced) climate change [1]. In fact, 11,000 scientists from 153 different countries have declared a climate emergency in 2017, sending a clear and urgent sign for the necessary major transformations in the way our global society functions and interacts with natural ecosystems [2]. The transition from burning fossil fuels to using renewable energy, particularly solar photovoltaics (PV) the production of electricity directly from sunlight, is one of the most promising avenues to reduce greenhouse gas emissions and thereby, avert some of the most feared effects of climate change. A recent report claims that installing about one terawatt of PV per annum will substantially reduce the global carbon dioxide emission [3]. The reduction is expected to be equivalent to the reduction needed to keep the average global temperature rise below two degrees.

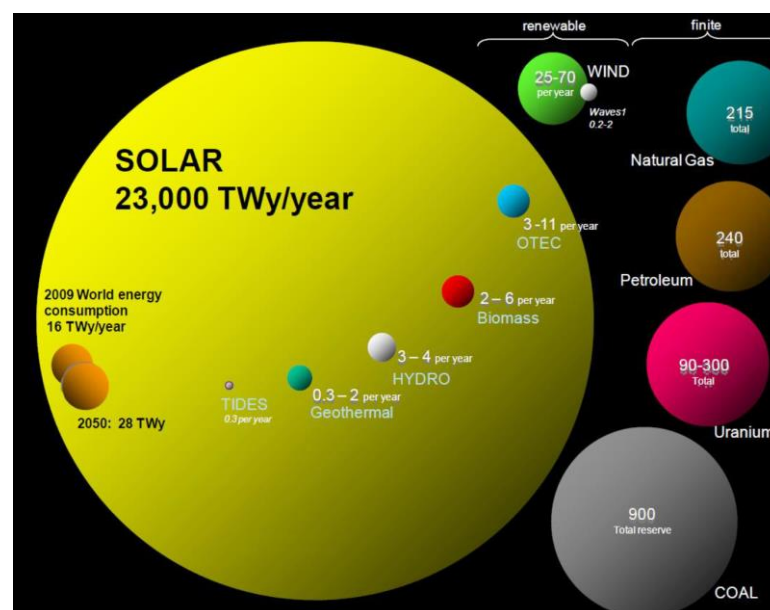


**Figure 1.1** Comparing finite and renewable planetary energy reserves (Terawatt/year) [4].

Figure 1.1 presents a comparison between the non-renewable and renewable energy reserves available, the former in absolute terms and the latter in terms of per annum. The

## 1 Introduction

brown circles in the very left represent the quantity of the world's primary energy consumption for the years 2009 and estimations for 2050. Although coal (gray circle on the right) is many times bigger than these demands, it is a **finite** resource and therefore it would only last for about another 30-40 years. This also means that even neglecting greenhouse gas emissions and the dramatic consequences they have for future generations, a transition to sustainable energy production will have to be managed long before we run out of fossil fuels.

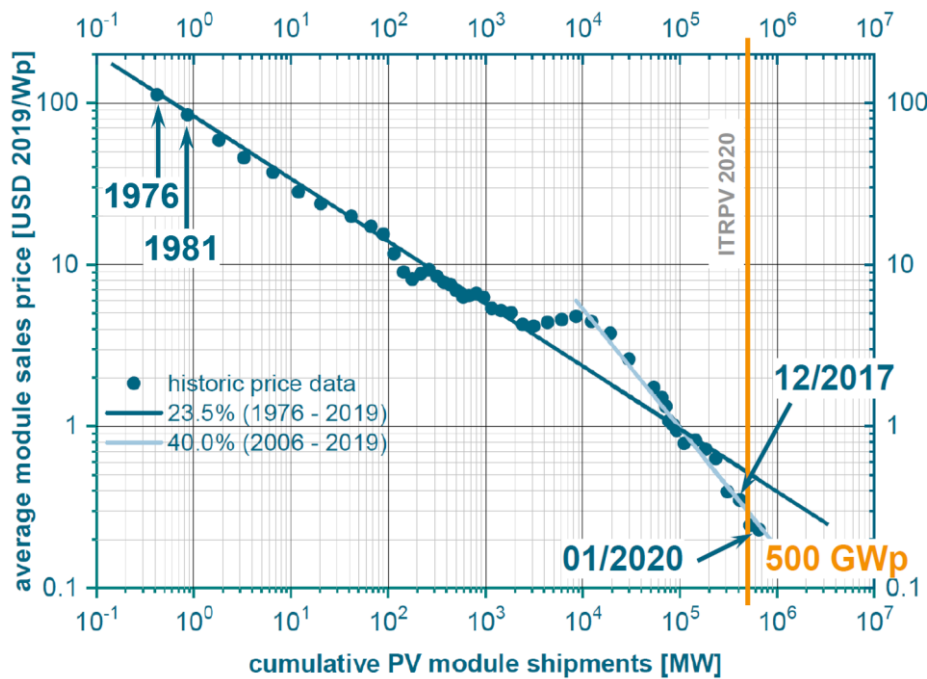


**Figure 1.2** PV learning curve reproduced from ITRPV 2020 [5].

Among all the energy sources presented, **solar energy** is by far the most abundant sustainable resource revealing its huge potential for the future of electricity. Another compelling reason for considering solar PV is its continuous rapid cost reduction. The learning curve of solar PV is presented in Figure 1.2 (taken from Ref. [5]). It shows a price reduction of a **factor of 500** from the year 1976 to the year 2020, with a current solar module price of 0.21 US\$/Wp [6]. Solar PV is now the cheapest form of electricity generation, considering both retail and wholesale, beating the price of electricity generation from fossil fuels [7].

As a result of this cost reduction and increasing environmental concerns, the total worldwide installed PV capacity has increased from 1 MWp in 1981 to 500 GWp in 2020, which is an increase by a **factor of 500,000** [5], [8]. The uptake of solar PV has been so extraordinary that in 2017, for the first time, the global installed PV capacity was larger

than that of fossil fuels and nuclear combined [9]. Even if neglecting urgent environmental concerns, for purely economic reasons solar will continue to rapidly grow and it can be expected that installation volumes will increase by at least two orders of magnitudes [7].

With the currently ~400 million solar modules being installed every year and considering the rapid future increase in installation volumes, it is important to maintain the quality and high performance of PV modules throughout their lifetimes in the field (currently the performance warranty period of modules are 25 years). This need becomes even more critical considering the very rapid technological changes that we have seen in recent years and can expect in the future.

Since PV modules are prone to degrade during transportation, installation, and operation, it is important to monitor the quality at their final destinations and not only during their production. Reliable system performance increases the system lifetime and reduces the power plant financing costs, lowering the Levelised Cost of Electricity (LCOE) [10]–[12]. Therefore, it is highly desirable to inspect PV modules in solar farms to identify defective modules and module degradations to ensure reliable power production. Based on these inspections and investigations, it is also important to provide the industry with feedback to assist technological decisions regarding the future.

## 1.2 Thesis objectives

Luminescence-based inspection technique is an immensely powerful characterization method that can provide high resolution spatially resolved information of cells and modules and is capable to identify most of the degradation modes [13]–[18].

Since its inception in 2005 [13], photoluminescence (PL) has contributed significantly for the breathtaking technological PV development [19]–[23]. It is used to inspect quality of solar cells from bricks [21] to final modules [22]. **The main objective of this thesis is to expend the capabilities of this technology to routine inspection of solar farms, the ultimate destination of PV modules.**

The main limitation for **outdoor** applications of luminescence-based techniques is the difficulty of detecting the weak luminescence signal in the presence of a much stronger ambient sunlight signal. Hence, the main objectives of this thesis include:

## 1 Introduction

1. Developing an easy and contactless PL-based inspection system that provides spatially resolved images to investigate modules installed in the field.
2. Investigating the impact of different measurement conditions on the image quality of resultant PL images.
3. Demonstrating the applicability of the outdoor PL imaging system to inspect a wide variety of fault mechanisms, such as cell cracks, open-circuit (OC) bypass diode (BPD) failure, and series resistance ( $R_s$ ) losses.
4. Developing a complementary characterization tool that uses the injection dependent behavior of individual cells that are encapsulated and field-deployed to provide a deeper understanding of the degradation.
5. Demonstrating the applicability of the tool proposed in (4) to investigate degradation mechanisms such as cell shunting, light-induced degradation (LID) and potential-induced degradation (PID) in real-world outdoor conditions.

### 1.3 Thesis outline

In Chapter 2, the background knowledge required to understand the proposed novel contactless modulation of PL is reviewed. Different degradation mechanisms in current PV technologies are discussed as well as existing module inspection techniques. The gaps in knowledge and capabilities are identified by reviewing the advantages and disadvantages of these techniques. Some of these gaps will be addressed in this thesis.

In Chapter 3, the development of a novel outdoor PL imaging system based on the methodology of *sequential* imaging approach is presented. **This is the world-first tool demonstration of a system that allows a large area luminescence imaging without electrically contacting the module terminals.** The capability of the developed system to investigate OC BPD failures is also demonstrated. However, it is demonstrated that the *sequential* switching approach is incompatible with PV systems containing module-level maximum power point tracking (MPPT).

In Chapter 4, a simplified approach (the *batch* measurement) is developed to overcome the problem of *sequential* measuring systems with MPPT. An advanced approach to correct for the sunlight changes during the measurement is proposed. The impact of factors such as time of the measurement, cell open-circuit voltage ( $V_{oc}$ ) and control cell



shunting on the outdoor PL image quality is studied. Finally, the applications of the proposed technique to quantify  $R_s$  losses in solar modules and to characterize PV panels on a solar car and in a large solar farm is presented.

In Chapter 5, a complimentary and detailed characterization technique based on the Suns-PL method [24] capable of extracting the current-voltage ( $I$ - $V$ ) characteristics of individual solar cells that are incorporated in field-deployed solar modules is proposed. The proposed method is demonstrated to be contactless, non-destructive and capable of identifying the extent of various degradation mechanisms.



## Chapter 2

### Background and Review

This chapter introduces the background theory that may aid the understanding of the novel work presented in this thesis along with a discussion regarding the relevant literature. Section 2.1 provides an introduction to PV systems and their important components. Section 2.2 provides an overview of the degradation and failure modes present in PV modules. Sections 2.3 and 2.4 review existing module inspection techniques that are used to assess the quality and longevity of fielded modules. The applicability of these methods to fielded modules is also discussed. Fielded modules refer to the modules installed in the PV field. To gain a deeper understanding of the underlying degradation mechanisms and its most plausible cause, it is helpful to characterize the individual cells encapsulated in the module. The commonly used encapsulated cell inspection techniques are discussed in Section 2.5. Finally, Section 2.6 summarizes the identified gaps in the literature among which some will be covered in the next chapters of this thesis.

#### 2.1 Photovoltaic system

##### 2.1.1 Photovoltaic technologies

There are four major types of PV technologies, namely crystalline, thin-film, compound and nanotechnology [25]. Among these, the market is dominated by crystalline silicon (Si) with about 80% of the market share as shown in Figure 2.1 [5], [26]. Crystalline Si technology is further divided into monocrystalline Si (mono-Si) and multicrystalline Si (mc-Si) [26]. Because of the continuous reduction in cost, the mono-Si market share increased to 65% whereas mc-Si holds 35% of the share in 2020 [5]. It is widely assumed that Si-based technology will continue to lead the market in the next decade [5]. This thesis explores the inspection of both mono-Si and mc-Si modules.

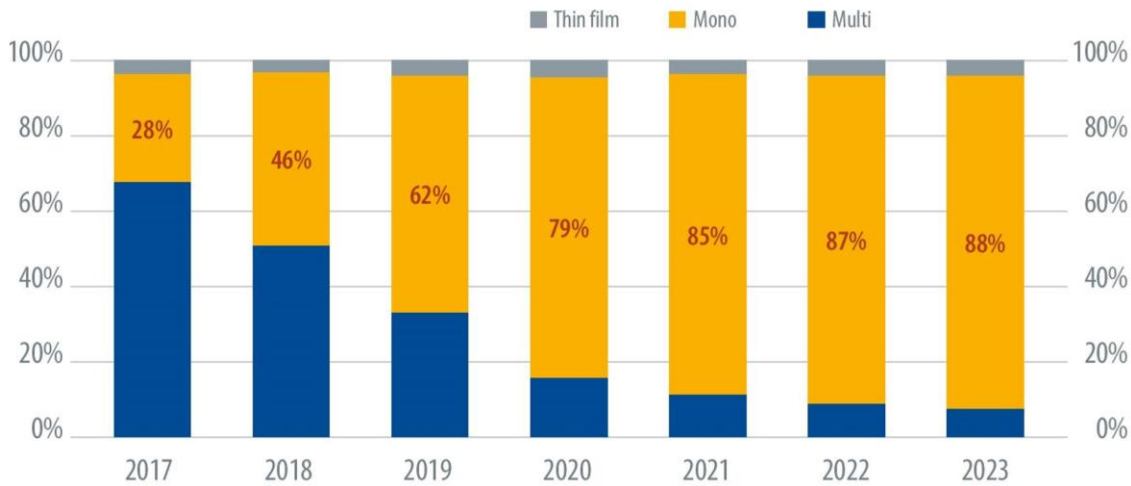


**Figure 2.1** Market share of major PV technologies [26].

### 2.1.2 Photovoltaic module components

The main component of PV system is the PV modules. The operational life cost of the system depends on the long term performance of the modules [27].

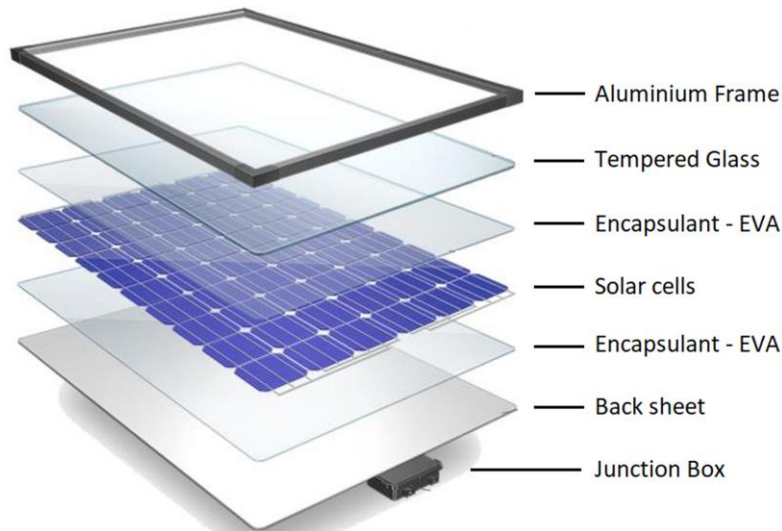


**Figure 2.2** Components of a PV module [28].

Terrestrial PV module consists of solar cells sandwiched between protective *tempered glass* on the front, and a glass or *polymer* on the rear using *encapsulant* as shown in Figure 2.2, protecting the solar cells from the weather, hail or airborne debris [29]. An aluminium frame often provides a strong structure that helps in mounting and provides strength to withstand external stresses [30]. A commonly used encapsulant is ethylene vinyl acetate (EVA) which is designed to provide longevity and prevents moisture ingress [29]. However, polydimethyl siloxane, polyvinyl butyral and silicones are used as well [29], [31]. A schematic of the electric circuit of a typical PV module is shown in Figure 2.3. It

consists of solar cells connected in a series configuration. Typically, a module consists of three BPDs that are connected in parallel to a section of series connected cells [32]. In the context of this thesis, we define a section of cells connected to the same BPD as a sub-string. The junction box encloses both BPD and cables used to interconnect the panels.

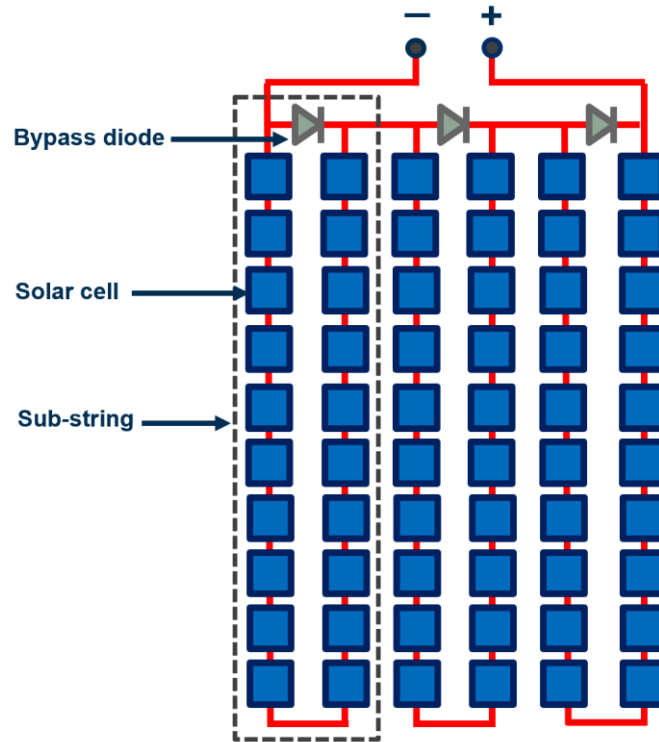


**Figure 2.3** Schematic of a PV module.

### 2.1.3 Photovoltaic inverters

Often several PV modules are connected in series to form a PV *string*, series connection is used to increase the string's direct current (DC) voltage output [33]. The variable DC output is then converted into sinusoidal alternating current (AC) with the required frequency of typically 50 Hz (outside the USA) using an inverter which facilitates the grid connection. Using an MPPT, the inverter also ensures that maximum power is extracted from the string despite continuing change of the operating conditions. In the past, central inverters were popular [34]. However, they are limited by power loss due to mismatch between modules, as the MPPT is centralized. In recent years, the most commonly used inverter technology is the *string* inverter [34]. With this type of inverters, the MPPT is performed at the string level, reducing the power loss due to partial shading [34]. Residential PV systems that are commonly installed on rooftops frequently suffer from shading due to trees, nearby buildings, poles, antennas or dormers [35]. Module-level power electronics (MLPEs) including microinverters and

DC/DC power optimizers are used in these scenarios [35]. These devices are capable of monitoring the maximum power point (MPP) of each individual module; thus, making the PV system most robust to partial and intermittent shading conditions which cannot be done with central or string invertors [36].

### 2.2 Degradation in fielded modules

There is a large variety of degradation and failure modes that could potentially affect fielded PV modules [37]–[40]. Degradation refers to the deterioration of appearance, performance or safety of a PV module [41]. There are several degradation types; they are mostly influenced by temperature, humidity, altitude, thermal cycling, snow load and air salinity [37], [38]. This section discusses common degradation mechanisms present in fielded modules.

#### 2.2.1 Discoloration

Encapsulant discoloration is one of the most apparent degradation found in PV fields [42]. Often, this effect is noticeable visually even before a reduction in module current is detected (Figure 2.4 [43]). Usually, the exposure of the polymeric encapsulant to ultraviolet light at elevated temperatures results in discoloration and loss of the elastic properties that further causes embrittlement [44]. Mikofski *et al.* showed that modules mounted on rooftops degrade ~0.4% per year in efficiency, whereas those on open-rack mounts degrade ~0.1% per year demonstrating the higher temperature of the rooftop arrays results in more severe EVA discoloration [45]. To avoid EVA discoloration, module manufacturers have been recommended to use formulations that do not contain additives that have been determined to cause discoloration, such as Naugard P [46].



**Figure 2.4** A power plant at Hahwa Island showing encapsulant discoloration issues [42].

### 2.2.2 Delamination and corrosion



**Figure 2.5** Optical image of a module (a), showing different regions (b) to (d) with delamination and moisture ingress [47].

Delamination usually occurs at the interface between the encapsulant and solar cell when there is a loss in adhesion [29]. It is expected to occur more severely in hot and humid climates [48]. One of the reasons behind delamination is the formation of bubbles due to gases released from EVA at high temperatures [49]. Due to delamination, moisture ingress can be formed which in turn can lead to the accumulation of small water droplets at the interface between the EVA sheet and solar cell, as shown in Figure 2.5 [47], [50]. The water droplets create and accelerate corrosion of the internal parts of the module [51]. The corrosion affects the resistance of the solder joints, cell metallization, interconnects and junction-box [42]. It, therefore, correlates with a reduction in the performance of the PV module [47], [52].

### 2.2.3 Interconnect failure

Cell interconnects are used for series connecting the cells using string interconnect ribbons [39] as shown in Figure 2.6. In some cases, these interconnects break causing disconnection in the circuit [39]. This degradation occurs when there is a change in either the structure or geometry of the interconnect solder joints [53]. Fatigue due to thermal



stress, poor soldering and mechanical stress like wind loading can lead to damaged interconnects [39], [54]. This damage usually increases the series resistance, causing heating and may lead to hotspots and fire hazard [55].

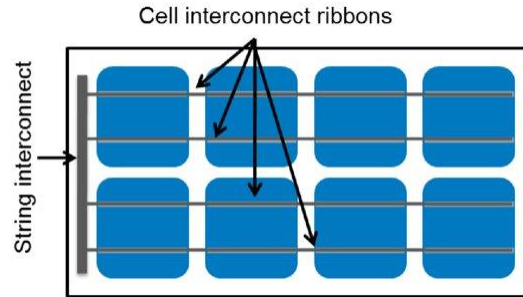


**Figure 2.6** Cell and string interconnects [39].

### 2.2.4 Defective bypass diode

Bypass diodes are vital to protect against hotspots and to reduce the power loss caused by partial shading of the PV module [56]. BPD failure is very common in PV systems and has two modes: OC and short circuit (SC) [57]. BPD can fail due to three main reasons [57], [58]:

- (1) Severe environment condition,
- (2) Low power rating, and
- (3) Overloaded by nearby lightning strikes.

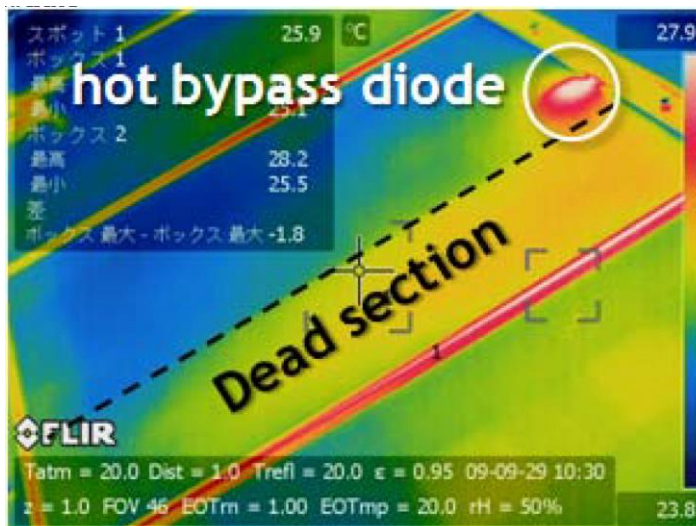


**Figure 2.7** Infrared image of a module with hot bypass diode and a dead sub-string [59].

A BPD failed in SC results in one-third of the module's power to be lost and is largely non-destructive [56]. An infrared (IR) image of a module with hot BPD and a



disconnected sub-string is presented in Figure 2.7. Usually, modules with BPD failed in SC is sent to the manufacturer for a more detailed investigation [56]. In contrast, BPD failed in OC mode has no impact at all on the module operation in normal operating conditions [58]. Therefore, detecting this failure is more challenging since the module power remains the same. However, it can cause module destruction, or even pose a fire hazard, under partial shading conditions or with malfunctioning cells in a sub-string [58], [60]. Signal Transmission Device (STD) proposed by Kato [61] is capable of detecting OC BPD failure and any local disconnection of interconnect ribbons in PV modules. Alternately, it can also be identified using magnetic field imaging [62] that extracts the current flow maps in a solar cell or module in a contactless manner. This thesis will present a novel cost-effective technique to detect this failure in a contactless manner.

### ***2.2.5 Hotspots***

If a solar cell is reverse biased with a higher voltage than it is rated or designed for, it may result in hotspots [56]. This can occur when a sub-string of solar cells without BPD or with BPD failed in OC is partially shaded [63]. Another cause for hotspots is the presence of shunting in the cell's p-n junction [64], [65]. Hotspots can lead to very high temperatures in the localised region of the solar cells and can thus cause browning, burn marks (Figure 2.8), or, in the worst case, fire [66].



**Figure 2.8** Burn marks as a result of hotspots [59].

### ***2.2.6 Cell cracking***

Solar cell material can crack, which is not noticeable to the naked eye, in most cases [67]–[69]. As solar cells are made from brittle Si material, cell cracks are often caused

due to mechanical loading on the modules. Although PV modules are tested against the IEC 61215 standard [70] which includes a static mechanical load test with 2400 Pa that simulates snow loads, this does not simulate all the possible mechanical loads that impact the PV module during its operation [71]. Cell cracks can occur at various stages right from manufacturing [72], transportation [73], installation [39] and during its operation [74], [75]. In the manufacturing process, it can occur at various stages like wafer slicing, cell production [76], stringing and the embedding process [72]. Inappropriate methods of transportation and mishandling create cracks that can be minimized by improving the packaging with additional protection and padding [77]. Furthermore, the occurrence of cracks is more common in the PV modules that are horizontally stacked compared to vertically stacked transportation choices [78]. During installation or maintenance, modules that have been walked-on may experience cracking [78]. Following proper protocols for installation can significantly mitigate crack formation. During operation in the field, cracks are usually formed by wind stresses [74] and snow [75]. Generally, these cracks are identified using electroluminescence (EL) imaging (see Section 2.4.3) during manufacturing. However, to investigate crack formation during transportation, installation or operation, field inspection is necessary.

The impact of a crack on the cell output power depends on the severity of the crack. The power output loss due to cracks is impacted by the size of the affected regions and the resistance between the affected regions and the rest of the cell [79]. If the power loss is significant, it can result in a mismatch of current between the cells in the sub-string. Hence, the cracked cell can be reverse biased by other cells in the sub-string increasing the hotspot risk. Cracks are classified into three modes depending on their degree of isolation based on the IEC/TS 60904-13 standard [79]:

(1) Mode A: cracks that do not generate inactive cell areas, and therefore do not contribute to cell power loss [80].

(2) Mode B: cracks that partially isolate a cell area and limit the current flow from the isolated region to the rest of the cell, causing a power loss.

(3) Mode C: cracks that completely isolate a cell area, where there is no current flow between the isolated area and rest of the cell resulting in a power loss proportional to the isolated cell area.

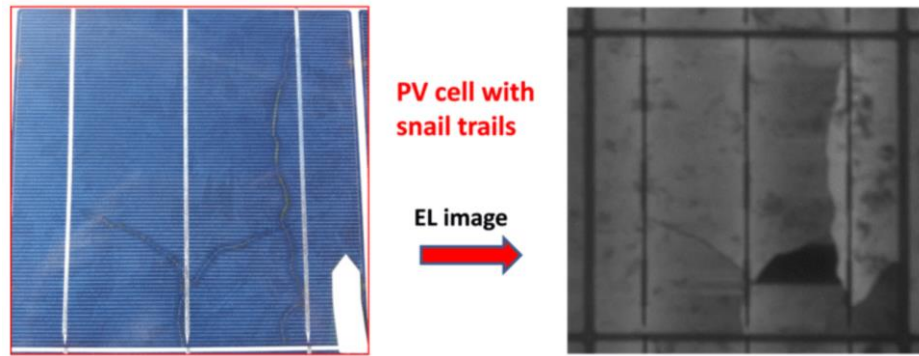


**Figure 2.9** Snail trail visible to the naked eye (left) and its corresponding EL image (right) revealing cell cracks [81].

The long time existence of cell cracks sometimes causes “snail trails” that are visible to the naked eye since they are the result of discoloration that occurs at the edge of the solar cell and along the cell cracks, as shown in Figure 2.9 [39], [81].

### ***2.2.7 Potential induced degradation***

Typically, modules are connected in series to form a PV system with a maximum voltage. The metallic frames of the modules are typically maintained at fixed ground potential to avoid electric shock to humans [82]. The difference in potential between the frame and the individual modules in the string creates a leakage current and high voltage stress across the different module components resulting in a degradation known as PID [83]. PID affects solar cells near the module edge more severely than those in the centre and modules at the end of a string [82], [83]. PID decreases the shunt resistance ( $R_{sh}$ ) and increases the recombination in the depletion region (saturation current density of the second diode,  $J_{02}$ ) in the solar cells [84] as demonstrated in Figure 2.10 (note the higher degradation of edge cells compared to the centre cells).

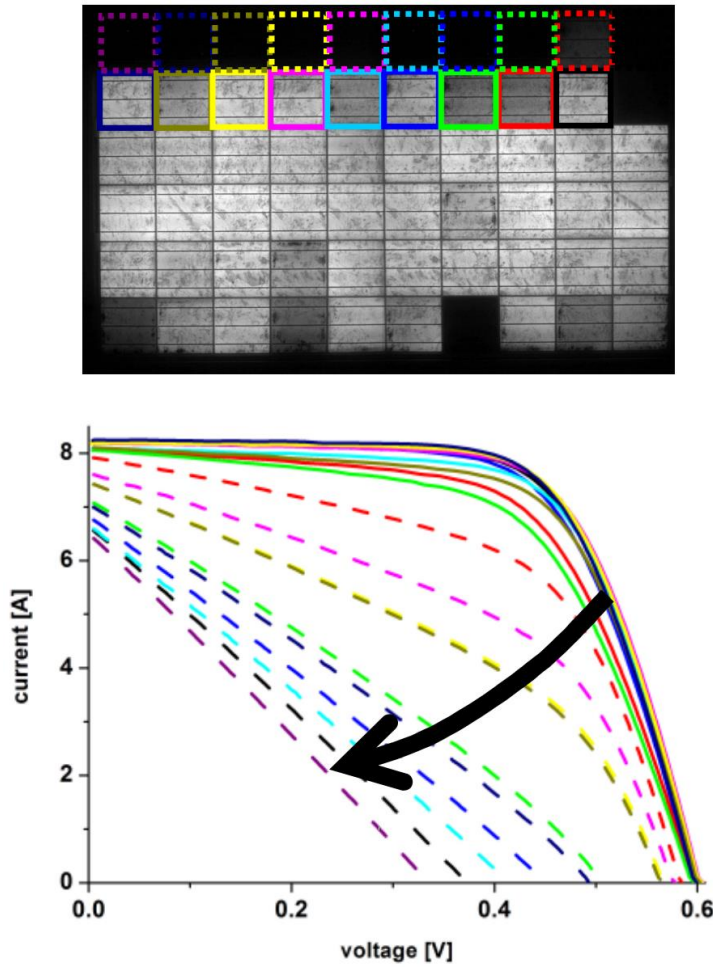


**Figure 2.10** EL image of a PID affected module (top) and  $I$ - $V$  characteristic of corresponding cells [82].

### 2.2.8 Light and carrier induced degradation

Some solar cells degrade due to the injection of carriers, either by light or current; this degradation is referred to as LID [85] or carrier induced degradation (CID) [86]–[89]. As a result of these degradations, the effective minority carrier lifetime in solar cells decreases. There are a significant number of studies investigating LID observed in p-type mono-Si material [90]. The cause of LID in this material is because of the formation of the recombination active boron-oxygen (BO) complex [86]. Although the reason behind CID in mc-Si solar cells is not exactly understood, it has been shown that they are not due to BO complex [91] or iron-boron (FeB) dissociation [89], [92], [93]. One of the possible explanations is that it is due to a high concentration of hydrogen into silicon wafers, released from hydrogenated dielectric layers during the firing process [88]. It has been observed that this degradation accelerates with higher injection densities or increased temperature as represented in Figure 2.11 [86]. Therefore, it is faster under the OC

condition compared to the SC condition [86]. Although the cells are expected to recover after attaining the maximum degradation (brown curve in Figure 2.11), the recovery time in the field is too long compared to the module warranty period [86]. Light and elevated temperature induced degradation (LeTID) is another type of degradation with rates of several hundreds to thousand hours (5–20 years depending on the location), which cannot be explained by BO complex formation or FeB dissociation [86]. LeTID is prominent in passivated emitter and rear contact (PERC) solar cells made of mc-Si wafers [94]. While the exact cause of this degradation is still unknown, it may be caused by an oversupply of hydrogen into the silicon wafers, released from hydrogenated dielectric layers during firing [88].

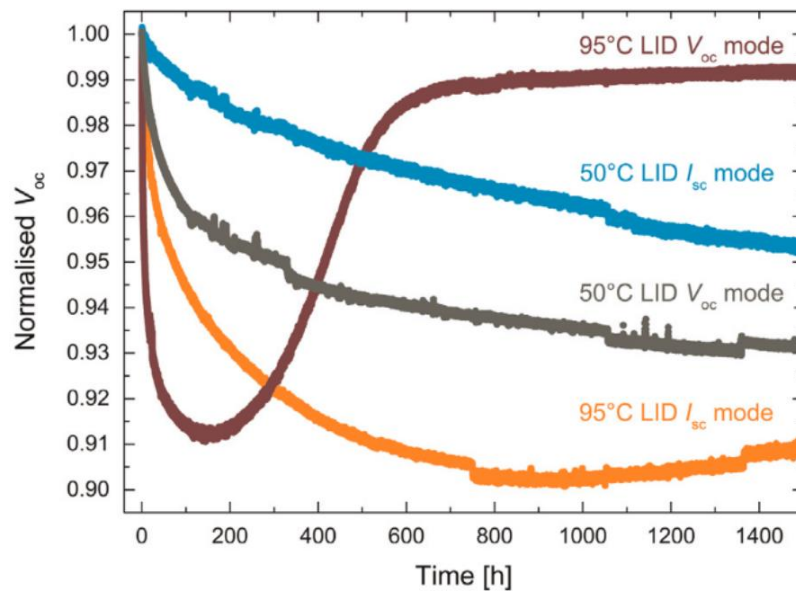


**Figure 2.11** Open-circuit voltage of mc-Si cells affected by CID with different temperatures and operating conditions [86].

## 2.3 Basic module inspection techniques

Several module characterisation techniques are often used to assess module quality and durability. This section provides a short review of the basic techniques, whereas Section 2.4 focuses on imaging-based inspection techniques.

### 2.3.1 Visual inspection

Visual inspection is one of the simplest and quickest module inspection techniques. According to the IEC 61215 standard [70], visual inspection is done using naked eyes while the illumination is above 1000 lux. The inspection is done from multiple angles to have a correct understanding of the fault and to avoid errors due to reflection. Faults such

as discoloration, delamination, bubble formation, snail trails and burnt cells are detected and documented using this method [54], [95]. Visual inspection is usually not sufficient to identify many electrical faults, such as degraded busbars, cell and string interconnects, wiring failure, junction box connection fault, and more. Although, sometimes they can be identified if they produce a visually noticeable consequence like burn marks or corrosion.

### 2.3.2 Current-voltage measurements

Current-voltage measurements are used to extract important electrical parameters, such as short-circuit current ( $I_{sc}$ ),  $V_{oc}$ , fill factor (FF),  $R_s$ ,  $R_{sh}$  and (efficiency) [95]. Table 2.1 which of the  $I$ - $V$  parameters is affected by some of the common degradation modes discussed in Section 2.2. Thus,  $I$ - $V$  measurements can be used to identify a few of the degradation modes.

Table 2.1:  $I$ - $V$  parameter affected by different degradation

| Degradation   | Parameter           |
|---|---------------------|
| Optical degradation: encapsulant discoloration, delamination, soiling or glass corrosion/breakage | $I_{sc}$            |
| Degraded interconnect   | $R_s$               |
| Broken interconnect   | $R_s$               |
| BPD failed in SC  | $V_{oc}$            |
| Cell cracks   | $I_{sc}$            |
| PID   | $R_{sh}$ , $V_{oc}$ |
| CID   | $V_{oc}$            |

Although they provide valuable information on module level degradation, it is challenging to perform them on individual modules when they are connected to a larger PV string in the field. Furthermore, with those measurements, only the overall module performance can be determined, failing to provide information regarding the specific performance-limiting region within the module. Therefore, they have only limited capabilities to identify the root cause of the power loss. This thesis presents a method that aims to address this gap.

## 2.4 Imaging-based module inspection techniques

### 2.4.1 Ultraviolet fluorescence imaging

Ultraviolet (UV) fluorescence imaging can detect cell cracks and EVA discoloration [96]. When a PV module is irradiated by a UV light source, the chromophores present in the EVA encapsulant are excited and emit fluorescence light (with wavelengths between 325 and 800 nm). The chromophores change to a non-fluorescent product when they are exposed to oxygen or UV for a long time, a process which is known as photobleaching [97]. Therefore, the cell edges and cell cracks, where oxygen can diffuse and reach the chromophores to degrade them, appear dark in the UV fluorescence image [68].

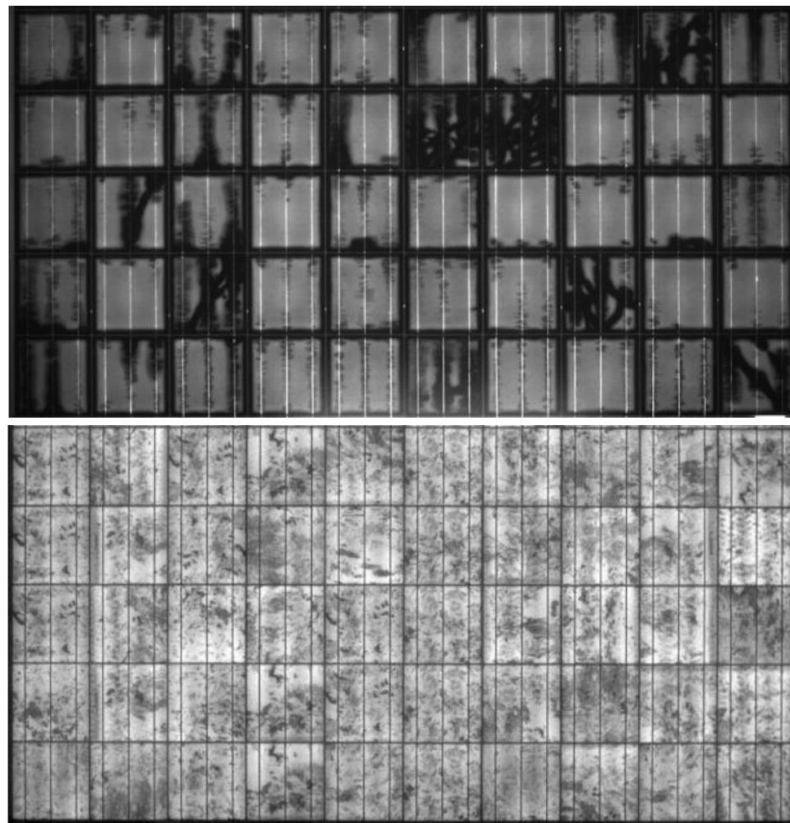


**Figure 2.12** UV fluorescence image (top) and the corresponding EL image (bottom) of the same module having cell cracks [98].

UV fluorescence imaging is limited to a specific time regime of field exposure since the chromophores require time to emit a sufficient fluorescent signal. Typically, after exposure to 80 kWh/m<sup>2</sup> UV dose for 1-2 years, the modules are expected to emit a detectable fluorescent signal [39]. This usually prevents the use of this method for the critical times of before or directly after module installation. On the other hand, it is preferred not to use this method for modules that are installed for many years as the cell

areas near the cell edges stop to emit fluorescence due to photobleaching; thus, restricting the identification of cracks in those areas as shown in Figure 2.13.

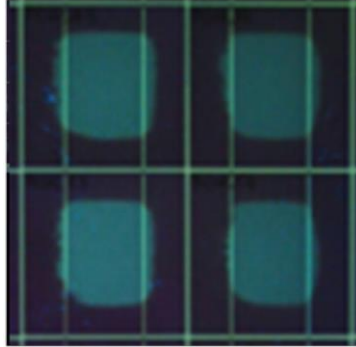


**Figure 2.13** UV fluorescence image of part of a module exposed in the field for approximately five years [97].

### 2.4.2 Infrared thermography

IR thermography identifies defects by capturing the emitted IR radiation (wavelengths between 800 and 1400 nm) from the modules which are dependent on the temperature distribution across it [99], [100].

Table 2.2: Different degradation modes identified by steady-state thermography

| Degradation                                    | Identification   |
|--|--|
| Broken cell interconnect                       | Low temperature due to restricted current flow through the broken cell interconnect, whereas high temperature (9-16 °C) around the neighboring interconnect as the entire externally injected current flows through them. Higher temperature of the junction box compared to nominal operation, due to current flow through the BPD.                             |
| BPD failed in SC or broken string interconnect | Higher temperature (2-6 °C) in the bypassed sub-string due to recombination of all the generated carriers.   |
| Hotspots or shadowing effects                  | High temperatures in the areas around the hotspot.   |
| Cell cracks                                    | Non-isolating cracks (Mode A) do not show temperature difference and are thus, not detectable.<br><br>Whereas, the electrically isolating cracks (Modes B and C) experience low temperature in the isolated area and high temperature in the unaffected adjacent area. The larger the size of isolated area, the higher is the temperature of the adjacent area. |
| Shunted cells                                  | Slightly higher temperature (1-2 °C) compared to the unaffected cells.   |
| PID  | Slightly higher temperature (2-3 °C).  |



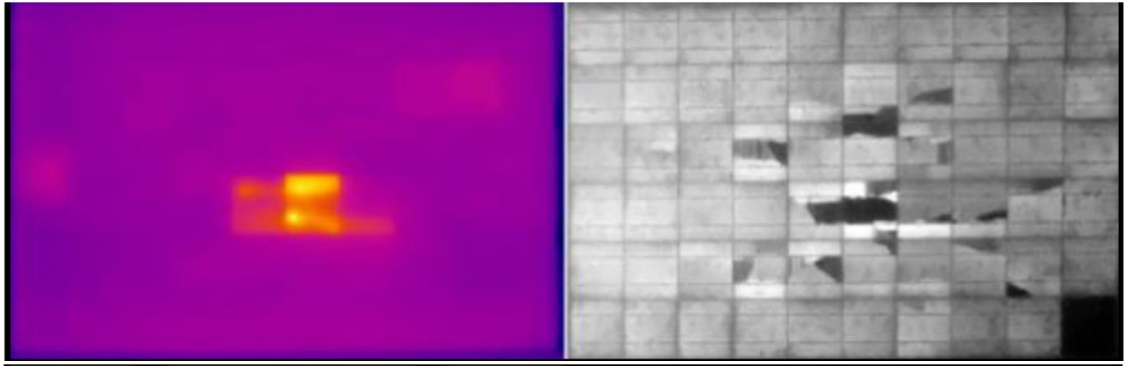


**Figure 2.14** Steady-state IR thermography (left) and EL images (right) of a degraded mc-Si module [98].

The method uses an IR camera that measures the heat dissipated to directly identify the areas of power loss in the modules [101]. To avoid misleading results, the angle of view and the correct emissivity should be considered. The ideal angle of view is in the range 60°-90° and the typical emissivity is 0.85 for glass and 0.95 for backsheet [102], [103]. There are three types of IR thermography:

1. Steady-state thermography
2. Lock-in thermography
3. Pulse thermography

Among these, steady-state thermography is the most widely used technique, as it can be applied to modules in the field under working conditions and is a contactless measurement [39]. The different degradation modes are identifiable using steady-state thermography and are summarized in Table 2.2 [104]–[106].

In lock-in thermography (LIT), the signal to noise ratio (SNR) is enhanced by exciting the module and detecting at a controlled frequency [107]. Whereas, in pulse thermography, an external heat source is used to generate a dynamic heat flux in the module to obtain the thermographic images [39]. LIT and pulse thermography are used when more detailed information is needed. However, these two methods are limited to lab conditions and demand an expensive high speed and high resolution infrared camera [39].

Although field inspection using steady-state IR thermography is cost-effective, fast and contactless, it is limited to identify only defects that cause heating of the modules, i.e. defects that cause reduced power output [39], [106], [107]. This method also suffers from

low sensitivity and resolution compared to the below mentioned methods such as luminescence imaging as demonstrated by Figure 2.14 [98].

### 2.4.3 Luminescence imaging

Luminescence-based characterization techniques, such as EL and PL imaging, can provide more detailed information than the above-mentioned methods [39]. They can provide high resolution spatially resolved information that can be related to the power loss within a string of modules [108]–[110], including: cracks [111], series resistance effects [112], bypass diode failure [39], LID [16], PID [15] and CID [18], [113].

EL imaging was first demonstrated by Fuyuki *et al.* [114] by applying a forward current to a solar cell and measuring the light emitted due to the radiative recombination of the generated carriers. PL imaging on the other hand uses an illumination light source to generate carriers, as first demonstrated by Trupke *et al.* [115] on Si wafers. The emitted light, the luminescence emission, has a typical spectrum as shown in Figure 2.15 (for Si at 25 °C).

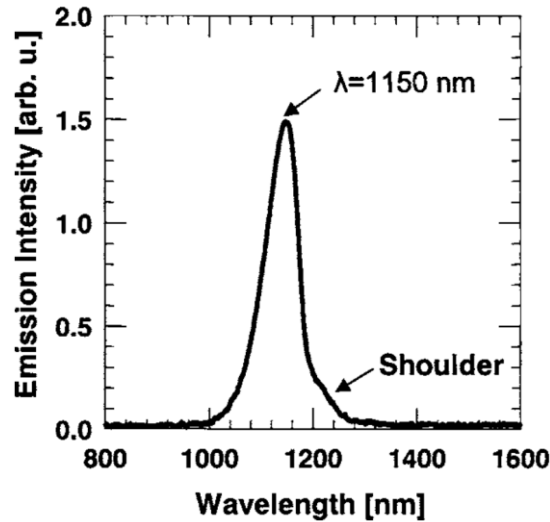


**Figure 2.15** Luminescence emission from Si solar cells [114].

The intensity of the luminescence emission ( $\Phi$ ) can be approximated by the exponential of the solar cell diode voltage  $V$  [36], [116]:

$$\phi = C \exp\left(\frac{V}{V_T}\right) \quad (2.1)$$

where  $C$  is a calibration constant mainly depending on optical characteristics of the solar cell and the measurement system and  $V_T$  is the thermal voltage (about 25.8 mV at room

temperature).  $V_T$  is given by  $kT/q$  where  $k$  is the boltzmann constant ( $8.617 \times 10^{-5} \text{ eV} \cdot \text{K}^{-1}$ ),  $T$  is the temperature (K) and  $q$  is Elementary charge, ( $1.602 \times 10^{-19} \text{ A} \cdot \text{s}$ ). Determination of  $C$  for cells in a module is challenging as there is no access to the individual cell terminals. Potthoff *et al.* [117] proposed the “voltage imaging of the PV module” (VIM) method to determine this value using an EL image of the module using two observations:

1. The operating voltage of an individual solar cell is proportional to the highest EL signal emitted from them.
2. The sum of all the cell’s operating voltages is equal to the module terminal voltage.

In this method, EL image is acquired with low current injection (less than 10% of  $I_{sc}$ ) to minimize series resistance effects, and therefore minimize voltage losses across the wire interconnects and module terminals.  $C$  is then estimated using the following relationship [117]:

$$C = N_{cell} \sqrt{\frac{\prod_{i=1}^{N_{cell}} \phi_i^{\max}}{\exp(V_{mod} / V_T)}} \quad (2.2)$$

where  $N_{cell}$  is the total number of cells in the module,  $V_{mod}$  is the module terminal voltage and  $\phi_i^{\max}$  is the maximum luminescence intensity of the  $i^{th}$  cell in the module. Using the  $C$  estimated from Equation 2.2, the operating voltage of the solar cells is calculated using Equation 2.1 with a maximum relative error of  $\pm 1.3\%$ . Köntges *et al.* [118] improved this method with an additional heuristic image manipulation approach which subtracts a mean intensity to reduce the influence of blurring effects of the camera. This decreased the error of the estimation of operating solar cell voltage to  $\pm 0.6\%$ . Guo *et al.* [119] suggested using the pixel with the maximum intensity *after* excluding the top 0.1% pixels with the maximum intensity is effective in eliminating the noise and thus, can yield a more accurate estimation of  $C$ .

One of the main challenges for performing EL or PL imaging in the field is the presence of strong ambient sunlight reflected from the module during image acquisition [15]. As shown in Figure 2.16, the ambient sunlight signal (solid black line) during the measurement is in orders of magnitude larger than the weak luminescence signal (solid

maroon plot) measured by the camera. Therefore, there were few luminescence imaging systems proposed for low light or night time applications as discussed below.

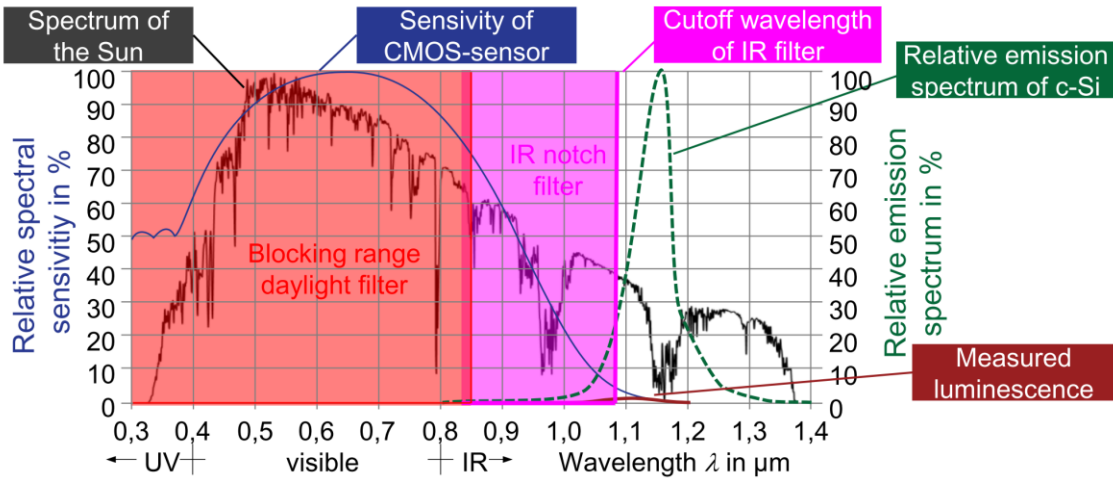


**Figure 2.16** Strong sunlight spectrum and the weak luminescence spectrum (barely noticeable in the dark red line) [120].

Koch *et al.* [98] developed a drone based EL imaging system in cooperation with Fladung aerial PV inspection [121] that operates at night or when the ambient light is low ( $<100 \text{ W/m}^2$ ) using an octocopter drone as shown in Figure 2.17. Mertens *et al.* [120], [122] developed an EL imaging system by modifying a digital single-lens reflex camera (DSLR) camera with a sunlight blocking and IR notch filter that is also used at night. However, night measurements are often not preferred due to safety and other practical considerations.



**Figure 2.17** High resolution EL camera with an octocopter drone for field inspection [98].

Benatto *et al.* [123] demonstrated outdoor EL imaging under different sun irradiation levels ranging from 300 to  $800 \text{ W/m}^2$  using an indium gallium arsenide (InGaAs) detector camera. Benatto *et al.* [124] demonstrated drone-based EL imaging under solar

irradiances greater than  $100 \text{ W/m}^2$  for the first time. A unique technique called AC+DC electrical modulation was proposed to obtain EL images with higher SNR even during motion, such as in the case of drone imaging. The drone used and the image quality after postprocessing are shown in Figure 2.18.

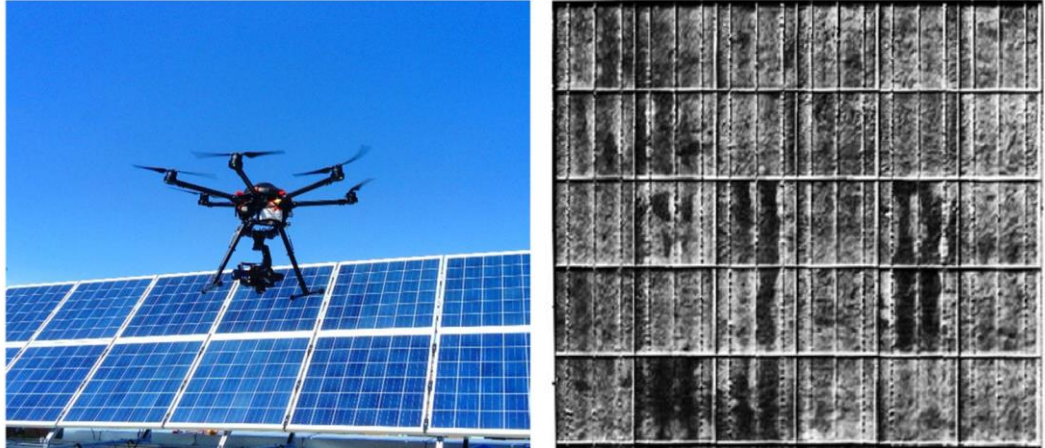


**Figure 2.18** Drone used with the corresponding EL image obtained outdoors using AC+DC electrical modulation [124].

One of the main limitations of the above-mentioned methods is that they need a high-power DC supply to bias the modules for EL imaging. On the other hand, PL imaging can provide the same benefits without any modification to the array [125]–[127]. Similar to steady-state IR thermography, PL imaging is electrically contactless and does not require any change in the wiring or an external power supply, as needed for EL imaging [128]. However, the requirement for a uniform high-power large-area illumination source makes it difficult to use PL for module inspection in the field although it has the additional benefit of being contactless.

Outdoor PL imaging for fielded modules by using the sun as the excitation has been demonstrated by several research groups. Silverman *et al.* [129] performed PL imaging with two different configurations:

1. Open-circuit outdoor PL: switching between OC and SC with the help of a modulator, directly connected to the PV module.
2. Constant-circuit outdoor PL: switching between  $0.7 I_{sc}$  and SC by connecting a DC load in parallel with the modulator and PV module.

The resulting PL images are shown in Figure 2.19. Parra *et al.* [130] obtained the PL images by switching the module operating conditions between OC and SC. They also

## 2 Background and Review

developed a software that uses image histogram information to enable adjustment of the image contrast and automatic selection of the largest exposure time, while avoiding saturation of the camera. Kropp *et al.* [131] use a modulator and capacitor configuration to achieve the image acquisition. One of the capacitors is charged and the power is boosted to a higher voltage by another capacitor before it is fed back into the module to create luminescence. Although these methods overcome the limitation of the requirement of a power supply by using the sun's illumination for generating luminescence, they still demand access to the string terminals to change its configuration.

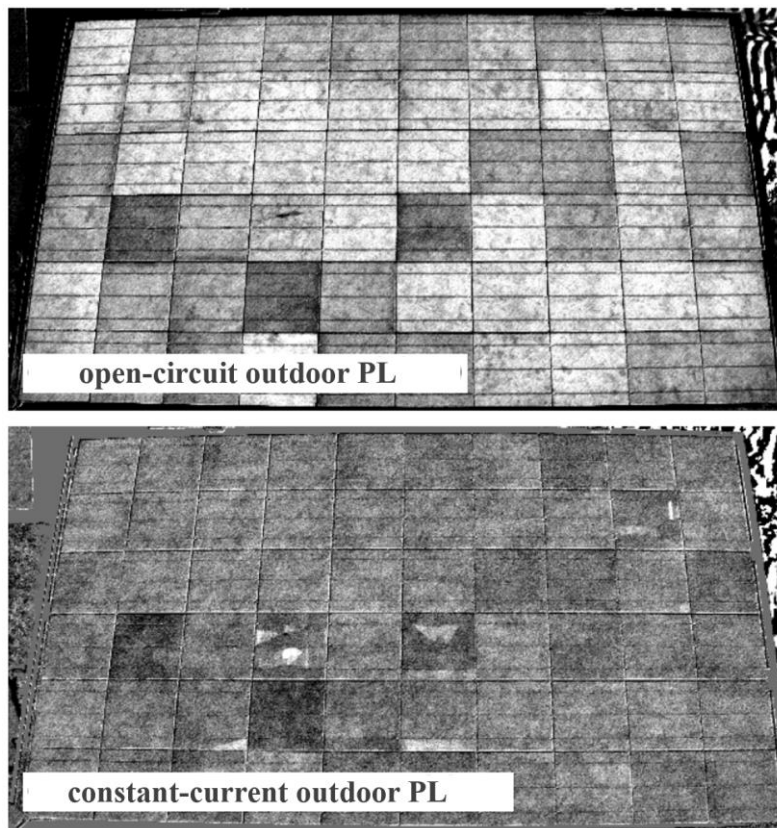


**Figure 2.19** PL images from the two configurations used by Silverman *et al.* [129].

Peng *et al.* [132] proposed a module PL imaging system that can be applied to cleaning robotic devices for tracing panel defects after cleaning the modules, as shown in Figure 2.20. Johnston [110] demonstrated a contactless EL imaging in which a localized area is illuminated (where excess carriers are optically generated) while the non-illuminated region of the cell is imaged (where the voltage is induced). Both of these contactless methods are limited since they can only image one cell at a time and can only be used at night-time and thus are not commercially viable to use for fielded modules.

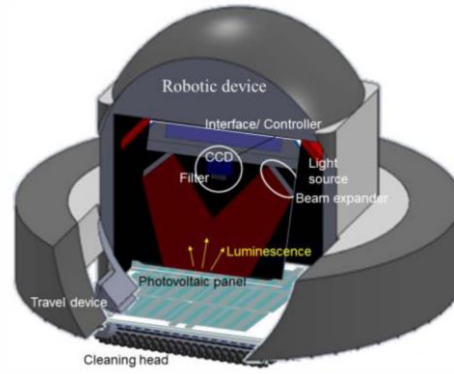


**Figure 2.20** PL imaging system proposed by Peng *et al.* [132].

There are a few commercially available services like DaySy [15], LumiSolar [133], Fladung ariel PV inspection [121], Sensors Unlimited [134], MBJ [135], and MRP Energy [136] for outdoor luminescence imaging.

To summarize, the existing luminescence-based techniques for outdoor inspection are limited either by:

1. The need to avoid strong ambient sunlight and only test at low light conditions [98], [110], [120], [132],
2. The requirement for special hardware for biasing [15], [123], [131], [133],
3. The ability to image only one cell at a time [110], [132], or
4. The need to contact the module or string terminals [15], [98], [135], [136], [121]–[123], [129]–[131], [133], [134].

The main advantages and disadvantages of different inspection techniques are summarized in Table 2.3.

Table 2.3: Main advantages and disadvantages of different inspection techniques

| Inspection technique | Advantages  | Disadvantages   |
|----------------------|---|---|
| Visual inspection    | Simple and quick<br><br>Identifies faults such as discoloration, delamination, bubble formation, snail trails and burnt cells | Identifies only faults that are visible to the naked eye<br><br>Cannot identify most of the electrical faults |
| I-V measurements     | Extracts important electrical parameters ( $I_{sc}$ , $V_{oc}$ , FF, $R_s$ , $R_{sh}$ and )                                   | Cannot measure individual modules (cells) in a string (module)  |

|                         |   |  |
|-------------------------|---|--|
|                         | Identifies faults caused by optical degradation, degraded/broken interconnects, BPD SC failure, cell cracks, PID and CID        | Only the overall string (module) performance can be determined                                     |
| UV fluorescence imaging | Identifies cell cracks and EVA discoloration  | Limited to a specific time regime of field exposure (>80 kWh/m <sup>2</sup> UV dose for 1-2 years) |
| IR thermography         | Cost-effective, fast and contactless  | Identifies only defects that cause heating   |
|                         | Steady-state IR thermography identifies broken cell interconnects, BPD SC failure, hotspots, cell cracks, shunted cells and PID | Low sensitivity and low resolution compared to luminescence imaging                                |
| EL imaging              | provides high resolution spatially resolved information   | Requires power supply to inject current  |
|                         | Identifies faults such as cracks, series resistance effects, bypass diode failure, LID, PID and CID                             |  |
| PL imaging              | Contactless measurement   | Requires an illumination source  |
|                         | Identifies faults such as cracks, series resistance effects, bypass diode failure, LID, PID and CID                             |  |

### 2.5 Extracting the current voltage characteristics of individual cells in a module

Techniques mentioned in Sections 2.3 and 2.4 have proven to be helpful in identifying performance limiting module faults. However, they all fail to provide more accurate and specific information regarding the nature of each fault [105], [137], [138]. In order to investigate the different degradation modes and their cause, *I-V* measurements of solar cells are generally highly desirable [139]. From such measurements, both the injection dependent lifetime [140] and the ideality factor [141] can be obtained, leading to a detailed understanding of the underlying detrimental recombination mechanisms [141].

Currently, it is challenging to extract the *individual* cell *I-V* information when cells are embedded in finished solar modules, as their terminals cannot be accessed electrically. This section discusses the different methods in the literature that aims to extract this information and their limitations.



### 2.5.1 Techniques based on LBIC

Eisgruber *et al.* [142] presented a method using light beam induced current (LBIC) measurements to extract the photocurrent and shunt resistance of individual cells in thin-film modules. Vorasayan *et al.* [143] used a modified LBIC measurement, the limiting laser beam induced current (li-LBIC) which is performed with background illumination, to extract similar information.

### 2.5.2 Techniques based on shading

Several methods have been proposed to extract the  $I$ - $V$  characteristics of individual cells of fully encapsulated PV modules that use multiple  $I$ - $V$  measurements of the module assuming specific shading on individual cells so they limit the current within the sub-string. McMohan *et al.* [144] used complete shading and two terminal measurements with the lock-in technique to measure  $R_{sh}$  of individual cells. Alers *et al.* [139] used the method of partially shading individual cells in a module to determine  $R_{sh}$  and  $I_{sc}$  from a collection of  $I$ - $V$  curves of a module. By partial shading, a method to calculate  $R_s$  of individual cells was proposed by Kim *et al.* [145]. A technique for extracting dark  $I$ - $V$  curves of individual cells in modules using the shading approach was presented by Bernardez *et al.* [146]; the technique was then used to obtain the ideality factor and diode saturation currents ( $J_{01}$  and  $J_{02}$ ). The dark  $I$ - $V$  curves of two different cells in a module, namely Cells 7 and 4, are extracted using this method as presented in Figure 2.21. The method clearly demonstrates the lower  $R_{sh}$  for Cell 7 compared to Cell 4. Combinations of shading were achieved by Yandt *et al.* using shutters fitted to allow complete blocking or complete illumination of cells for concentrating PV modules as shown in Figure 2.22 [147]. This was done to extract individual cell degradation factors. An automated method to acquire current maps of PV modules and individual cell  $I$ - $V$  curve was demonstrated by Koutsourakis *et al.* [148] and it does not require mechanical shading on the cells. Instead, a commercial digital light processing projector and compressive sampling is used to achieve the same result. Blakesley *et al.* [149] recently presented a method to extract individual cell's  $I$ - $V$  parameters by shading each cell with many well-defined irradiance levels and using a least-squares inverse problem to solve the electrical parameters of the equivalent circuit.

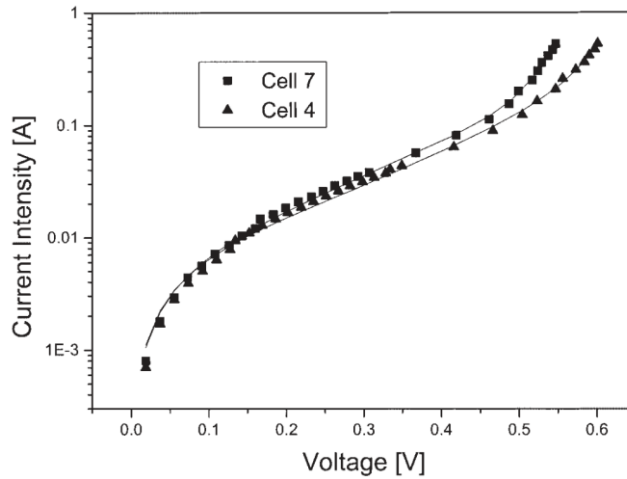


**Figure 2.21**  $I$ - $V$  curves of two different cells in a module extracted using the method proposed by Bernardez *et al.* [146].

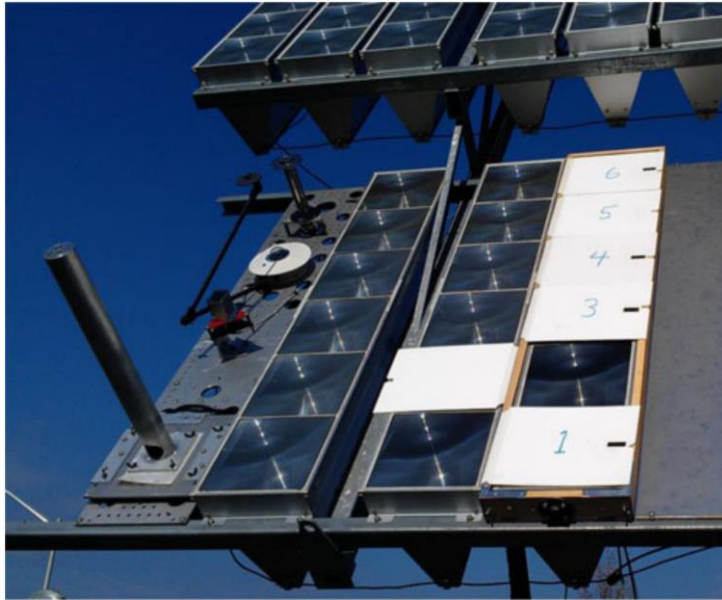


**Figure 2.22** Remotely operated shutters fitted to enable complete blocking or complete illumination of cells in any combination [147].

### 2.5.3 Techniques using electroluminescence or infrared imaging

This section discussed the studies that use EL and IR imaging along with module-level  $I$ - $V$  data to extract the individual cell performance parameters.

Fruehauf *et al.* [150] developed a method to determine the individual cell parameters, such as ideality factors and diode saturation currents in a module by analyzing ratios of EL intensities between pairs of cells, together with the module  $I$ - $V$  curve. Köntges *et al.* [118] and Potthoff *et al.* [117] proposed methods to obtain the voltage distribution of individual cells based on the measured EL signal. Guo *et al.* [119] used the method proposed in these two studies to construct the dark  $I$ - $V$  curves of individual cells by

calculating the operating voltage of individual solar cells for EL images acquired at different current injection conditions. However, this method is time consuming considering that many images are needed with a different current injection. Recently, Rajput *et al.* proposed a fast and simple technique that can determine  $R_s$  and dark saturation current density ( $J_0$ ) of each cell by extracting two EL images with a different current injection which enables classification of cell's performance into 'good', 'under' and 'bad' categories.

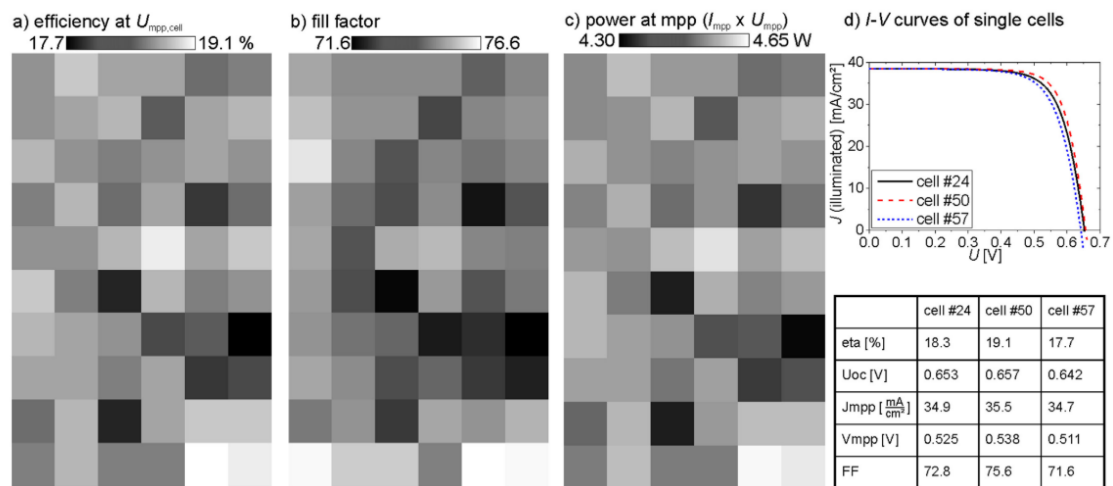


**Figure 2.23** Cell performance parameters: (a) efficiency at MPP, (b) FF, (c) power at MPP and (d) illuminated  $I$ - $V$  curve [151].

Bauer *et al.* [151] developed a method to provide more detailed spatially resolved performance parameter data of cells in a module using EL, IR and DLIT imaging. Using the proposed method, the obtained performance parameter such as  $\eta$ , FF, power and  $I$ - $V$  curve of cells in the module is presented in Figure 2.23. Although this method provides detailed information, it is complicated as it demands many different measurements.

Note that all the methods discussed so far are limited by the necessity of accessing the module terminals for the extraction of information.

## 2.6 Chapter summary

This chapter reviewed the important components of the PV system. It also reviewed the variety of degradation modes found in fielded modules along with several inspection techniques currently used to identify them. Different cell inspection techniques that extract the  $I$ - $V$  characteristics and enable a deeper understanding of the associated degradation modes are also discussed.

## 2 Background and Review

From the review, it has been observed that the basic inspection techniques involving visual inspections are limited to identifying only the faults that produce visually noticeable consequences, while the module  $I$ - $V$  measurements are limited in providing information regarding the specific performance limiting region within the module. It is understood that UV fluorescence is applicable only with modules with a specific time regime of field exposure, whereas IR thermography is a cost-effective, fast and contactless imaging-based technique but limited to identifying only the defects that cause temperature changes. The reviewed existing luminescence-based imaging techniques are found to be limited in terms of low light operation, need for special hardware, time consuming cell by cell imaging or the need for contacting the module terminals.

This thesis presents a novel PL imaging technique for fielded modules that overcomes all the above-mentioned limitations as presented in Chapters 3 and 4.

From the review on different encapsulated cell inspection techniques, it has been found that the existing techniques require accessing the module terminals for extracting the degradation information which demands a qualified electrician and sometimes sophisticated equipment and methods. This requirement limits or even prevents the use of these methods for a routine inspection of fielded modules.

This thesis presents an innovative technique that is fast, simple, cost-effective and contactless in Chapter 5 to obtain implied  $I$ - $V$  curves from encapsulated cells in a module.

## Chapter 3

### Outdoor photoluminescence imaging<sup>1</sup>

It was established in Chapter 2 that PL imaging is a potentially useful characterization technique to inspect solar modules in the field. In this chapter, the development of a novel outdoor PL imaging system will be presented. This is the world-first tool to allow contactless (without the need for contacting the module terminals electrically) outdoor PL imaging. The system developed in this thesis uses the sun as the sole illumination source to obtain PL images by separating the weak luminescence signal from the much stronger ambient sunlight signal. The proposed method contactlessly modulates the operating point of cells within a module.

#### 3.1 Methodology

Acquiring PL images during daylight is challenging since the ambient reflected sunlight from the measured modules is orders of magnitudes stronger than the peak of the luminescence spectrum of crystalline Si devices at room temperature. Nevertheless, the reflected sunlight is relatively low in the peak PL wavelength range due to the fortunate fact that an atmospheric water vapor absorption dip exists in the spectral range 1100-1160

---

<sup>1</sup> This Chapter is partially based on:

**Bhoopathy, R.**, Kunz, O., Juhl, M., Trupke, T. and Hameiri, Z., “Outdoor photoluminescence imaging of photovoltaic modules with sunlight excitation,” *Progress in Photovoltaics: Research and Applications*, 26(1), pp.69-73, 2018.

**Bhoopathy, R.**, Kunz, O., Juhl, M., Trupke, T. and Hameiri, Z., “Inspecting series resistance effects and bypass diode failure using contactless outdoor photoluminescence imaging” in 7th World Conference on Photovoltaic Energy Conversion, pp. 0377-0380, 2018.

**Bhoopathy, R.**, Kunz, O., Juhl, M., Trupke, T. and Hameiri, Z., 2019. A simplified contactless method for outdoor photoluminescence imaging. In *46th IEEE Photovoltaic Specialists Conference* (pp. 2571-2574).

nm as shown in Figure 3.1. This dip is influenced by humidity, clouds, zenith angle of the sun and the albedo of the earth's surface [152].

Studying the dependence of the luminescence emission from a Si solar cell at different operating points, the intensity of the PL emission,  $\phi_{PL}$  can be closely approximated by the exponential of the cell's implied voltage,  $V_i$  (Equation 2.1).

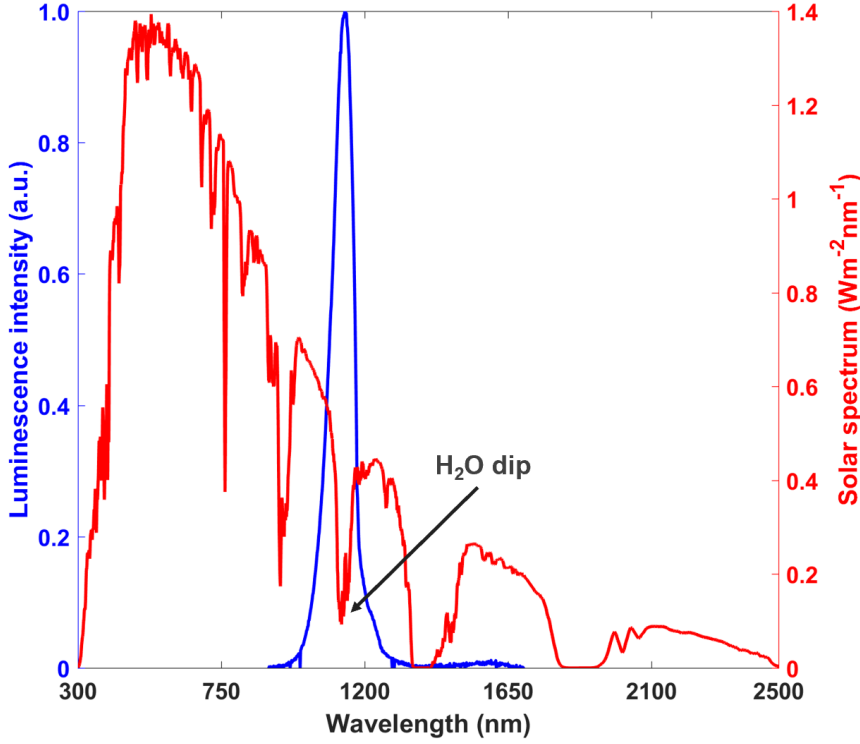


**Figure 3.1** Normalized solar cell luminescence spectrum compared with the typical solar spectrum.

Under OC condition, the cell voltage is higher than the voltage under operating conditions with current extraction, thus, stronger PL emission is expected at OC. Extraction of carriers from the device results in a lower device voltage and hence, lower PL emission. When the module is in SC or MPP condition, almost 100% or 95% of the carriers are extracted, respectively (leaving only the so called voltage independent carriers in the cell [153]), consequently resulting in a significant reduction in the PL emission compared to OC condition. In other words, the PL emission at SC or MPP is proportional to the carriers extracted in  $I_{sc}$  or MPP current ( $I_{MPP}$ ), respectively.

Hence, by switching the operating conditions of the cells in a module, their PL emission can be modulated. This principle allows separation of the Si PL emission from the strong background sunlight during outdoor PL measurements, as will be explained below.

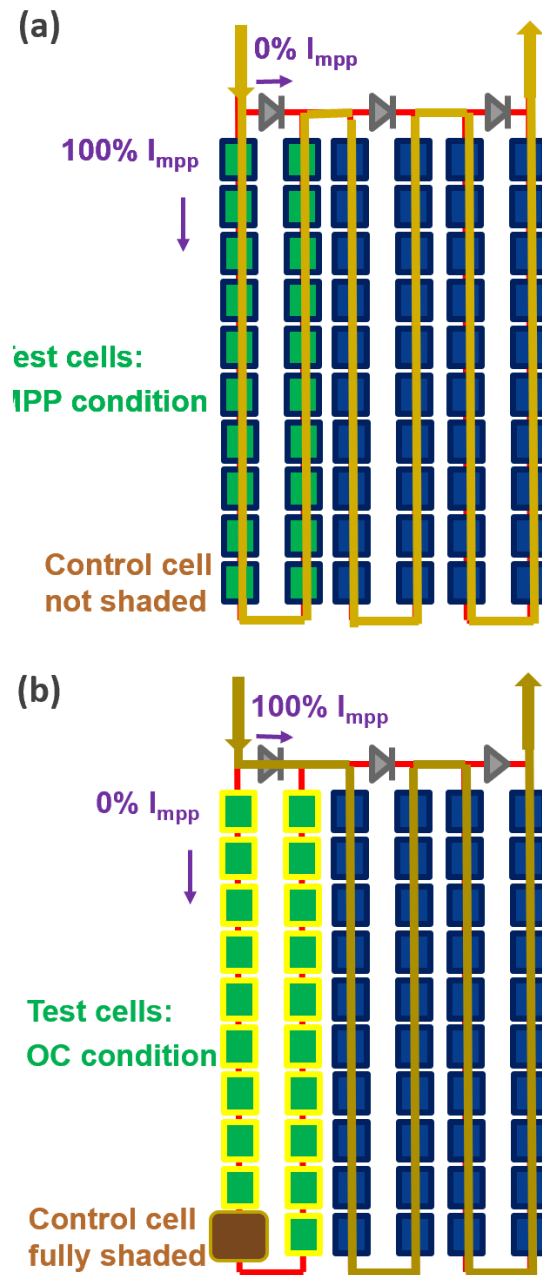


**Figure 3.2** Contactless PL modulation by (a) not shading and (b) shading of a control cell, when the module is operating at MPP.

For the following discussion, the module is assumed to be a part of a larger PV system, with several modules connected in series and a string inverter keeping the entire string at its MPP. Under standard operation, the MPP current ( $I_{MPP,system}$ ) flows through all cells as shown in Figure 3.2(a). All cells in the module are connected in series, and hence, the current flowing through an individual cell is determined by the current flowing through the cell with the lowest light induced current that is connected to the same BPD. Therefore, if the optical generation in one cell (from hereafter referred as the *control cell*) is zero (fully shaded), it restricts the current flow through all other cells in the same sub-string

### 3 Outdoor photoluminescence imaging

(referred as the *test cells* in the rest of the thesis) forcing them to switch to OC condition (or very close to it, as determined by the reverse current of the control cell). In this case, the current flows via the alternative path through the BPD of the shaded sub-string, as shown in Figure 3.2(b) [154]. Moreover, the current in the test cells can be limited to any value lower than the module's  $I_{sc}$  by setting the appropriate optical generation rate in the control cell. For example, if the control cell is illuminated with 0.75 Sun-equivalent light intensity, the current extracted from the test cells in this sub-string will be 75% of the short circuit current of the control cell  $I_{sc,control}$ . This will force the test cells to their respective cell voltages at this current, while the excess current ( $I_{MPP,system} - 75\% \times I_{sc,control}$ ) is bypassed through the BPD. It should be noted that whenever the illumination intensity on the control cell is sufficiently small so  $I_{sc,control} < I_{MPP,system}$ , the control cell is reverse-biased by the other cells in the same sub-string. This is typically the case when the illumination on the control cell is less than 95% (relative) of one Sun-equivalent intensity. For a fully functioning module, this operating condition is considered safe as each cell that is integrated into a module is tested during production to have a reverse breakdown voltage higher than the sum of the forward voltages of all other cells in a sub-string. Reverse bias of around -15V is expected for a fully shaded control cell in a typical 72 cells PV module with  $V_{oc}$  of 650 mV [155]. However, since this reverse voltage is applied to the control cell, a small leakage current flows can be measured in some cases (depending on the cell reverse bias characteristics), even when the control cell is fully shaded. This leads to a slight deviation from OC condition in the test cells, and thus to a quasi OC condition. However, care needs to be taken if the corresponding BPD has an OC failure, as discussed in Section 3.5.

Therefore, by exploiting a modulation of the carrier generation in the control cells, different biasing conditions can be deliberately obtained in the test cells. Thus, in normal field operation, the test cells can be switched between quasi OC condition (when the control cell is completely in the dark) and any other operating point (OP) between quasi OC condition and MPP, since the latter is the common condition for an operational PV system when all cells are fully illuminated.

### 3.2 Proof of concept

In order to demonstrate the proposed method and to investigate the effect of ambient sunlight intensity on outdoor measurements, spectral measurements are performed with



a near-infrared spectrometer [156] pointing at a test cell on an outdoor PV module under ~one Sun illumination in the month of April in Sydney.

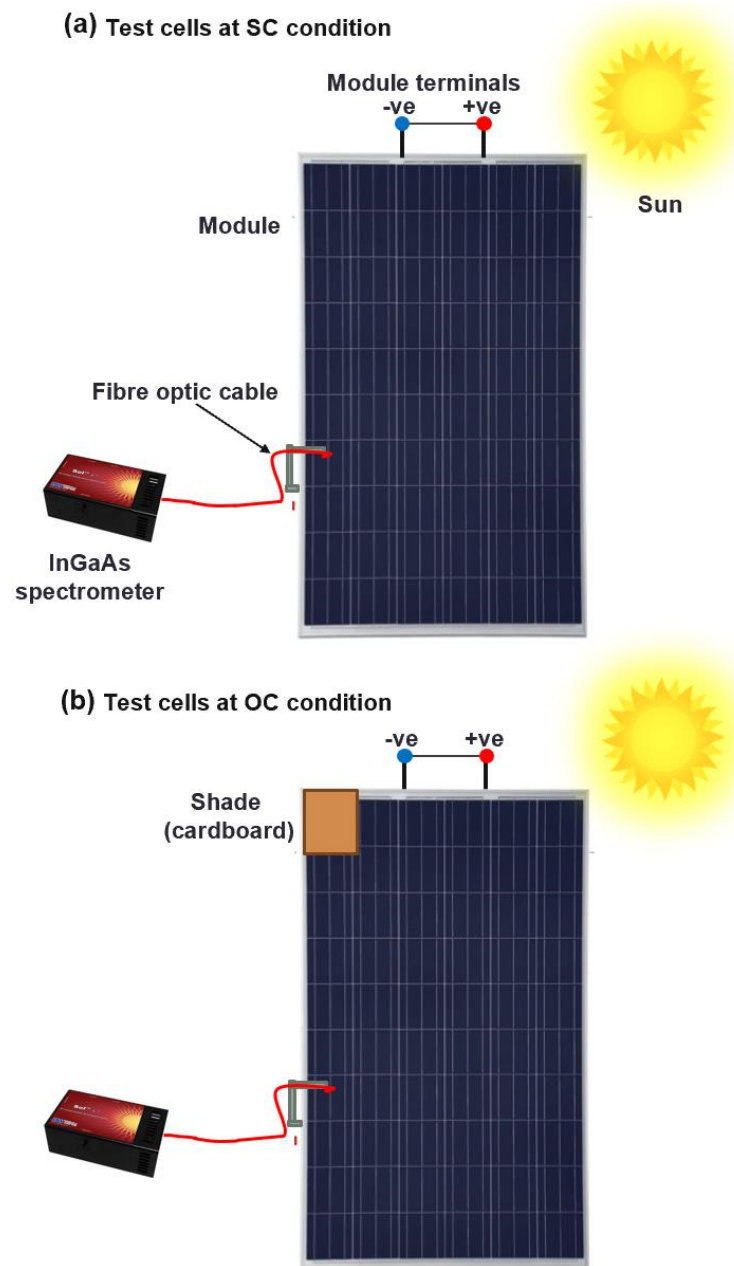


**Figure 3.3** Experimental setup for measurement of reflected spectra from one of the test cells, while the control cell is (a) fully illuminated and (b) fully shaded.

A 60 cell ( $156 \text{ mm} \times 156 \text{ mm}$ ) commercial mc-Si module is investigated. The module has a peak power output rating of 260 W and a cell voltage of 645 mV. The spectra of a representative test cell in the module are measured with diffused and specular reflection with **shorted** module terminals. Since switching between SC and OC is simpler and is expected to result in higher PL emission compared to switching between MPP and OC, the initial proof of concept was performed using those conditions. Two conditions are

### 3 Outdoor photoluminescence imaging

tested: (i) control cell is not shaded (fully illuminated by the sun), and (ii) control cell is completely shaded (zero illumination) (Figure 3.3).

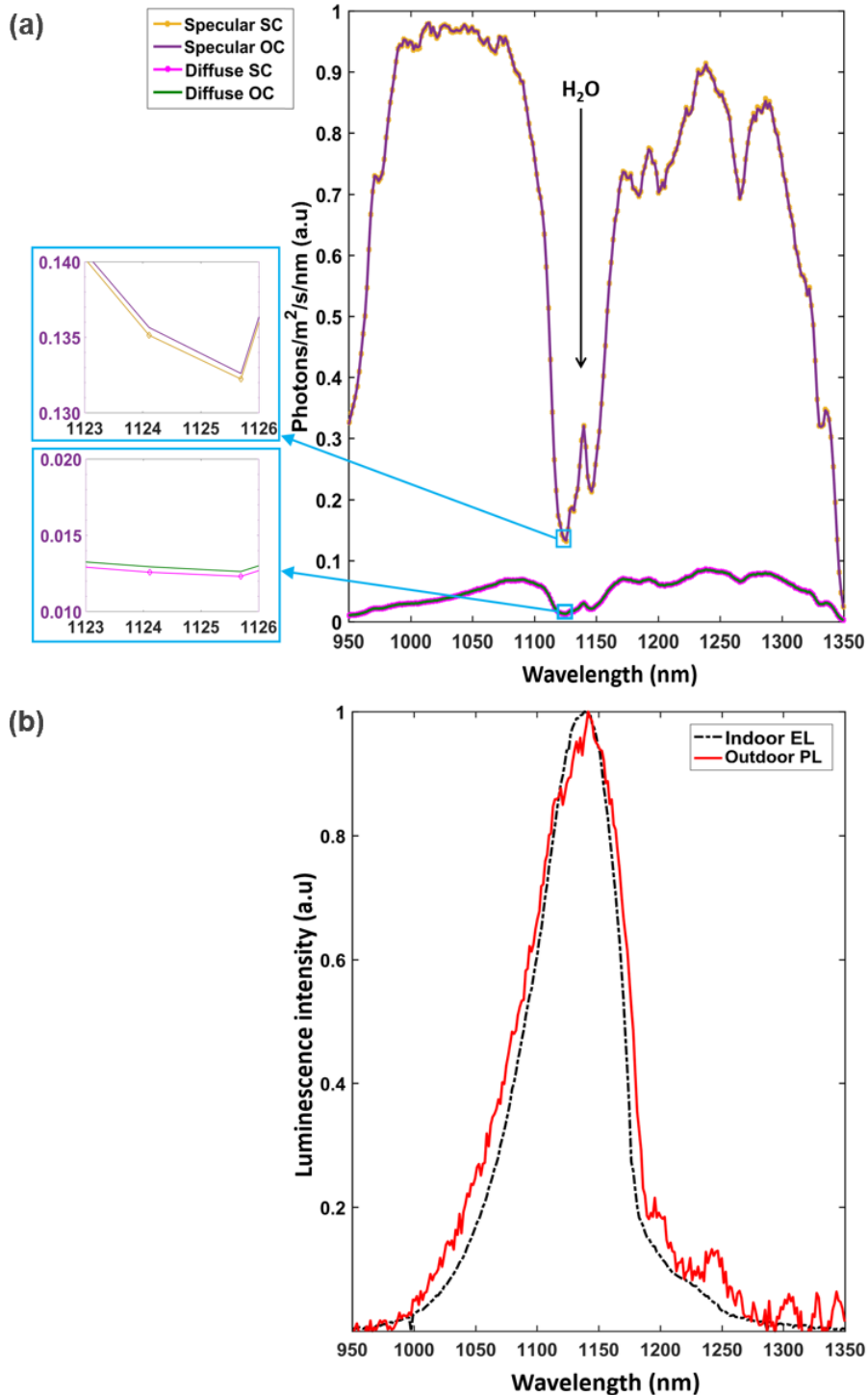


**Figure 3.4** (a) Measured spectra while the test cell is in OC and SC with diffuse and specular+diffuse reflection; (b) extracted outdoor PL spectrum and indoor EL spectrum.

By changing the illumination conditions of the control cell, the test cells are switched between OC and SC conditions. The spectra displayed in Figure 3.4(a) are measured under two conditions: (i) specular reflection of direct sunlight from the module along with

the diffuse reflection and (ii) only diffuse reflection. These measurements reveal that for specular reflection [Scenario (i)], the measured ambient sunlight is about one order of magnitude greater than that of Scenario (ii), highlighting that direct specular reflection of sunlight into the detection system should be avoided for outdoor measurements. Note that the sunlight spectrum strongly drops towards shorter wavelengths ( $<1100$  nm), due to the strong decrease in the reflectivity of PV modules at shorter wavelengths.

Measurements at SC and OC lead to two slightly distinct spectra in the 1000-1300 nm wavelength band, where higher values are measured under OC conditions due to the additional emitted Si luminescence. This small distinction between the spectra, shown in the close-up inserts of Figure 3.4(a), reveals that the detected PL signal is very weak compared to the ambient sunlight signal.

The Si luminescence spectrum can be extracted by subtracting the spectra obtained in SC from OC. The comparison of this intensity difference to the EL spectrum taken indoors is shown in Figure 3.4(b). Very good agreement is achieved with an average root mean square (RMS) deviation of less than 7% in the wavelength range of 1000 to 1200 nm, which is noteworthy, given the small magnitude of the PL signal compared to the ambient sunlight.

This preliminary experiment proves the feasibility of the proposed contactless modulation concept, achieved here with a simple baffle placed over the control cell. Note that similar results are measured if the cell is modulated between OC and MPP. The experiment also provides evidence that a sufficient PL signal is present. It can be measured even under the presence of very strong ambient sunlight. This is encouraging and leads to the next section where the development of the imaging system is discussed.

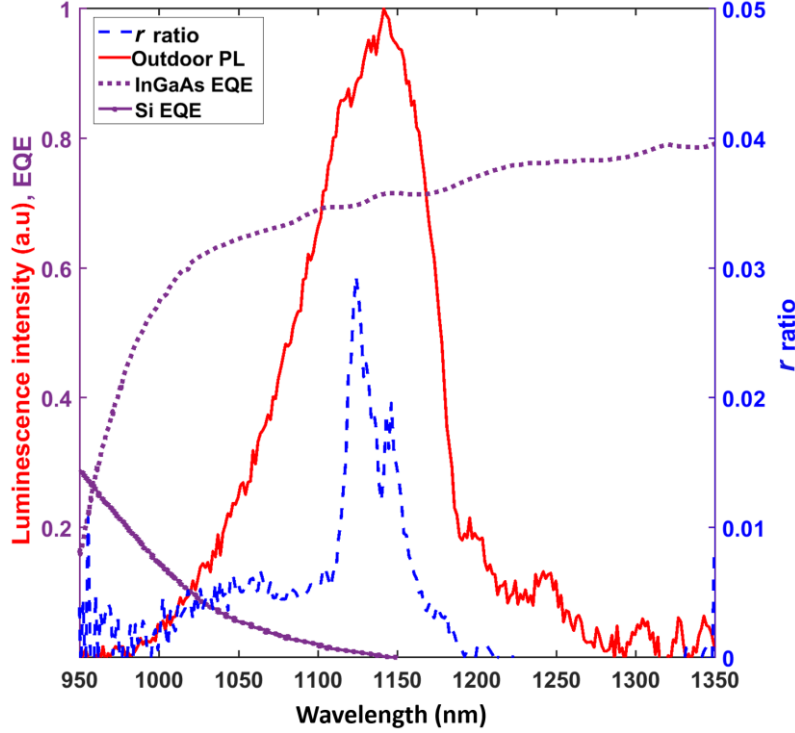
### 3.3 Development of imaging system

For camera-based PL measurements, one of the key parameters is the ratio of the desired PL signal to the total measured signal, which needs to be high. In this thesis, the ratio is defined as:

$$r = \frac{S_{OC}(\lambda) - S_{SC}(\lambda)}{S_{OC}(\lambda)} \quad (3.1)$$

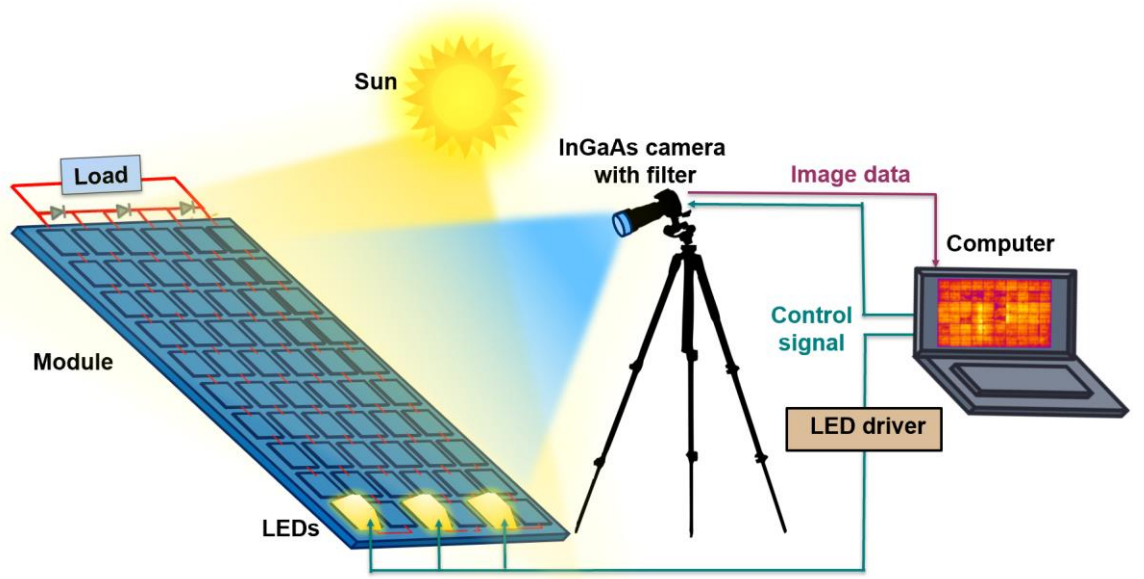
where  $S_{OC}$  and  $S_{SC}$  represents the measured spectral intensity at OC and SC, respectively.

Figure 3.5 presents this ratio together with the external quantum efficiencies (EQE) of typical Si and InGaAs cameras [157]. The outdoor PL spectrum, taken from Figure 3.4(b), is also presented. It can be seen that  $r$  peaks at a wavelength of 1124 nm. This is because at that particular wavelength, the PL signal is relatively large while the sunlight signal is relatively low, due to the dip in the solar spectrum as a result of water vapor absorption as shown in Figure 3.1.



**Figure 3.5** Camera EQEs and the  $r$  ratio as a function of wavelength.

The difficulty of taking PL measurements in the sun increases with decreasing  $r$ . InGaAs cameras are most appropriate for outdoor PL measurements since  $r$  peaks at wavelengths greater than 1100 nm, where Si cameras have a very poor quantum efficiency of less than 2%. Due to the steep drop in  $r$  at both longer and shorter wavelengths, a commercially available bandpass filter with cut-on and cut-off wavelengths of 1125 nm and 1150 nm, respectively, is chosen to be mounted in front of the camera lens.



**Figure 3.6** Schematic diagram of the experimental outdoor PL setup.

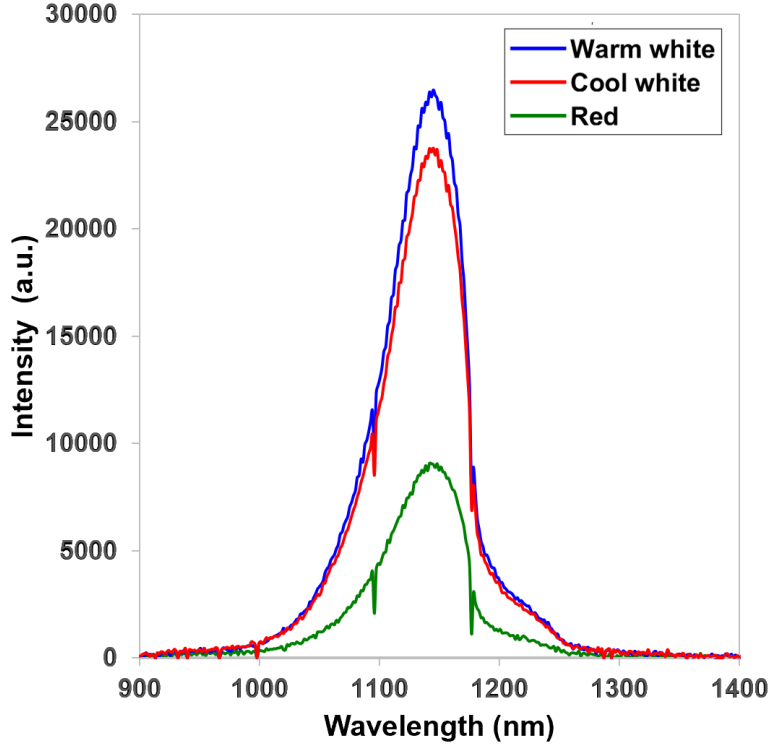
The proposed modulation approach is implemented in an outdoor PL system, as schematically shown in Figure 3.6. The system consists of a thermoelectrically cooled InGaAs camera [158], [159] with the aforementioned optical bandpass filter. The InGaAs camera has a sensor resolution of  $640 \times 512$  pixels, an analog to digital conversion resolution of 14 bits, a quantum efficiency greater than 60% in the relevant wavelength range, and a maximum frame rate of 25 frames per second. An external frame grabber [160] with a frame buffer of 120 MB is used to temporarily store and transfer the images to a computer through a USB 3.0 bus.

Table 3.1: Light generated current for different LED

| LED          | Parameter            |
|--------------|----------------------|
| Warm white   | $I_{sc}$             |
| Cool white   | $0.91 \times I_{sc}$ |
| Red (660 nm) | $0.45 \times I_{sc}$ |

A high-power light emitting diode (LED) is chosen to be placed on top of the control cell instead of a baffle, to physically block the sunlight from the control cell and therefore imposing OC condition in test cells. Turning the LED ON (irradiating the control cell with one sun or slightly above one sun equivalent light intensity) and OFF toggles the test cells between MPP and OC, respectively, while the module is operating in MPP condition by an electronic load [161] connected to its terminals. Using LEDs has the advantages of

(i) precisely changing the irradiation on the control cell and (ii) achieving a high frequency switching that can be synchronized with the camera capture. Another option to shade instead of LED is to use percentage mesh-based shading to achieve different irradiation.



**Figure 3.7** Measured PL spectra obtained with different LEDs.

To select the appropriate LED, three different 500 W commercially available LED's arrays namely "warm white", "cool white" and "red" (660 nm) are investigated. The LEDs are mounted on top of a reference cell and the PL spectrum is measured using an InGaAs spectrometer [156] when the cell is at OC condition, as shown in Figure 3.7. Additionally, the light generated current for each LED is measured while the reference cell is in SC condition, as presented in Table 3.1.

Since the warm white LED generated most carriers, it is selected for the system. The LED's switching time is measured and the turn ON and turn OFF delay are found to be 40  $\mu$ s and 3 ms, respectively. Due to the LED ability for fast switching, it does not constrain the image acquisition rate to 25 frames per second. Since the BPD is a passive electronic component, it reacts very quickly (less than 10  $\mu$ s) to the variations in illumination intensity on the control cell, enabling the above optical modulation to be carried out with sufficiently high frequency. The camera acquisition is synchronized with the LED switching to acquire the outdoor PL image pairs using a control signal from the

computer. The use of the developed imaging system to obtain successful outdoor PL images is discussed in the next section.

### 3.4 Outdoor photoluminescence image

The proposed method is subsequently applied to a commercial mono-Si PERC module ( $V_{oc} = \sim 660$  mV/cell). Figure 3.8 presents the image of the module exposed to  $\sim$ one Sun illumination captured by the outdoor PL system. The module is operated at MPP condition using an electronic load [161] maintained at MPP voltage. During the measurement, the test cells are switched between OC and MPP. As observed in Figure 3.8(a-b), even with suitable optical filtering, the emission captured by the camera under both conditions is dominated by the ambient diffused sunlight. Only after subtracting the MPP image from the OC image, eliminating the large fraction of almost constant ambient light, the PL image is obtained [Figure 3.8(c)]. In this thesis, the two images taken at different operating points are referred to as an ‘*image-pair*’ and the PL image obtained from them as an *outdoor PL* image. Note that, in this process, the PL information of the control cells is lost. It can, however, be obtained by repeating the same process selecting different cells as control cells and stitching them into a single image. Therefore, at least two images are required to image the entire module.

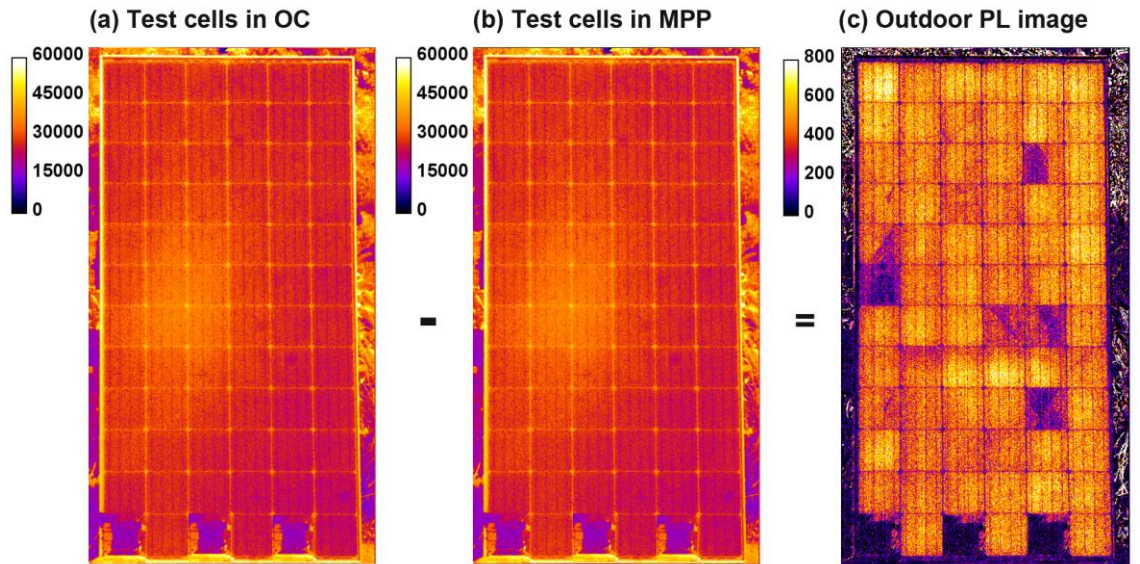


**Figure 3.8** Image captured by the outdoor PL system while the test cells are switched between (a) OC and (b) MPP and the corresponding (c) difference image; The scale on the left represents the intensity in counts.



### 3 Outdoor photoluminescence imaging

The outdoor PL image quality can be enhanced by obtaining multiple image pairs. To obtain multiple image pairs, the LEDs are sequentially turned ON and OFF during the synchronized image acquisition. This measurement procedure is referred to as *sequential* measurement in this thesis. The average pixel counts from sequentially captured images under approximately one sun condition are shown in Figure 3.9 (a). An increase in the pixel counts is observed while the LED is OFF, representing the additional PL signal on top of the constant ambient sunlight signal. In this case, the additional signal is about 1.6% of the ambient signal. Note that the change in the overall measured average pixel counts is due to the change in sunlight intensity during the measurement. In the case of multiple image-pair acquisitions, the resultant outdoor PL image is obtained from the difference between the average of all images taken with the LED OFF and the average of all images taken with the LED ON.

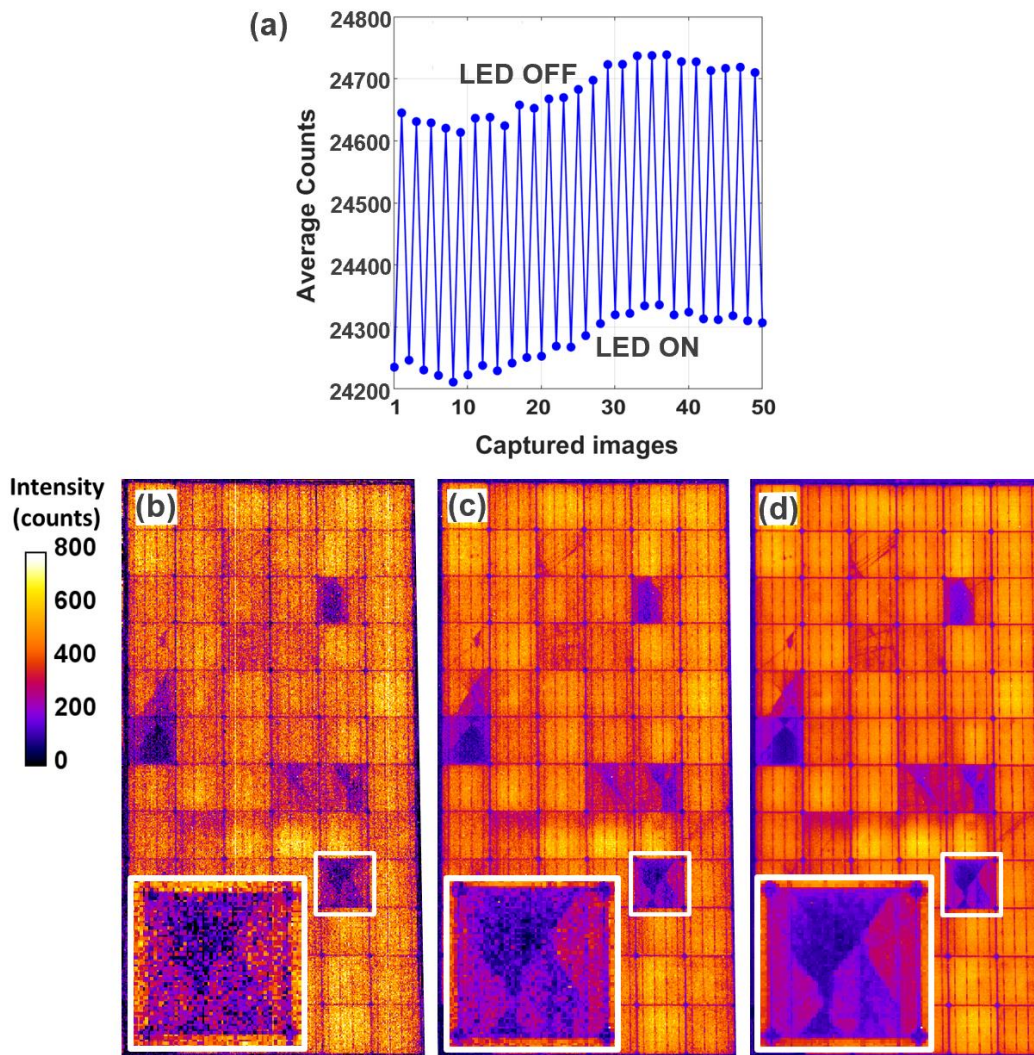


**Figure 3.9** (a) Measured average pixel counts of images of a mono-Si PERC module. Resulting average outdoor PL image of the module considering (b) 1, (c) 4, and (d) 25 image-pairs (close-up of the highlighted cell is shown as an insert in the bottom left corner).



The impact of the number of the taken image pairs on the quality of the outdoor image is shown in Figure 3.9(b-d). The insert in the bottom left corner presents a close-up of the highlighted cell, illustrating the capability of the proposed method to provide detailed outdoor images of defects even at the cell level. In this measurement, the field of view of the camera was set to the entire module size, which corresponds to a spatial resolution of about  $3 \times 3 \text{ mm}^2$  per image pixel. The figure qualitatively illustrates that although the image quality is improved when a larger number of image-pairs are averaged, averaging of only four image pairs (total image acquisition time of 320 ms) is sufficient to clearly identify severe module defects, such as cracks and isolated regions. It is noteworthy that overall poorly performing cells can already be identified with only a single image-pair. As future cell technologies obtain higher voltages, the PL intensity significantly increases; hence, a shorter acquisition time will be required in the near future to obtain high-quality images. A detailed quantitative analysis of the image quality will be provided in Chapter 4.

### 3.5 Bypass diode failure inspection using PL emission

Bypass diode failure is very common in PV systems [57] and poses an increased hot spot risk that stems from the fact that no BPD protection exists in the affected sub-string as discussed in Chapter 2. In this section, I propose a method to contactlessly identify OC bypass diode failure in the field.

The basic idea for contactless BPD testing is related to the imaging approach discussed above. Essentially, the variation in luminescence intensity in the test cells of a particular sub-string relies on the presence of a functioning BPD. If the BPD is in OC or missing, then the modulation of the illumination intensity of the control cell will *not* result in a modulation of the operating point of the test cells, and therefore no variation of the luminescence emission will be detected. In this case, the normal maximum power current is forced through the control cell, exactly the scenario that the BPD is designed to avoid. This approach assumes that the system is sensitive enough to measure the change in emitted luminescence that would occur from switching, as well as that there is enough voltage to reverse bias a single cell. Both assumptions are generally fulfilled in typical PV systems.

#### 3.5.1 Modelling

LT-Spice [162] is used to simulate a 72 cell PV module in the field for different control cell shading fractions, in the presence or absence (equivalent to BPD at OC) of a BPD, as

shown in Figure 3.11. The shading fraction is changed in the simulation by changing the light generated current  $I_L$  of the control cell, while the module is kept at MPP voltage.

In the presence of the BPD (solid lines), as shading is increased, the light generated current in the control cell, and therefore the sub-string current decreases linearly once the intensity on the control cell drops by more than approximately 5% as shown in Figure 3.11(a). As a result, the operating point of the test cells shifts from MPP towards OC, and the emitted PL from the test cells increases correspondingly. Note that the emitted PL, in this case, is calculated from the cell terminal voltage as it is exponentially related (from Equation 2.1).

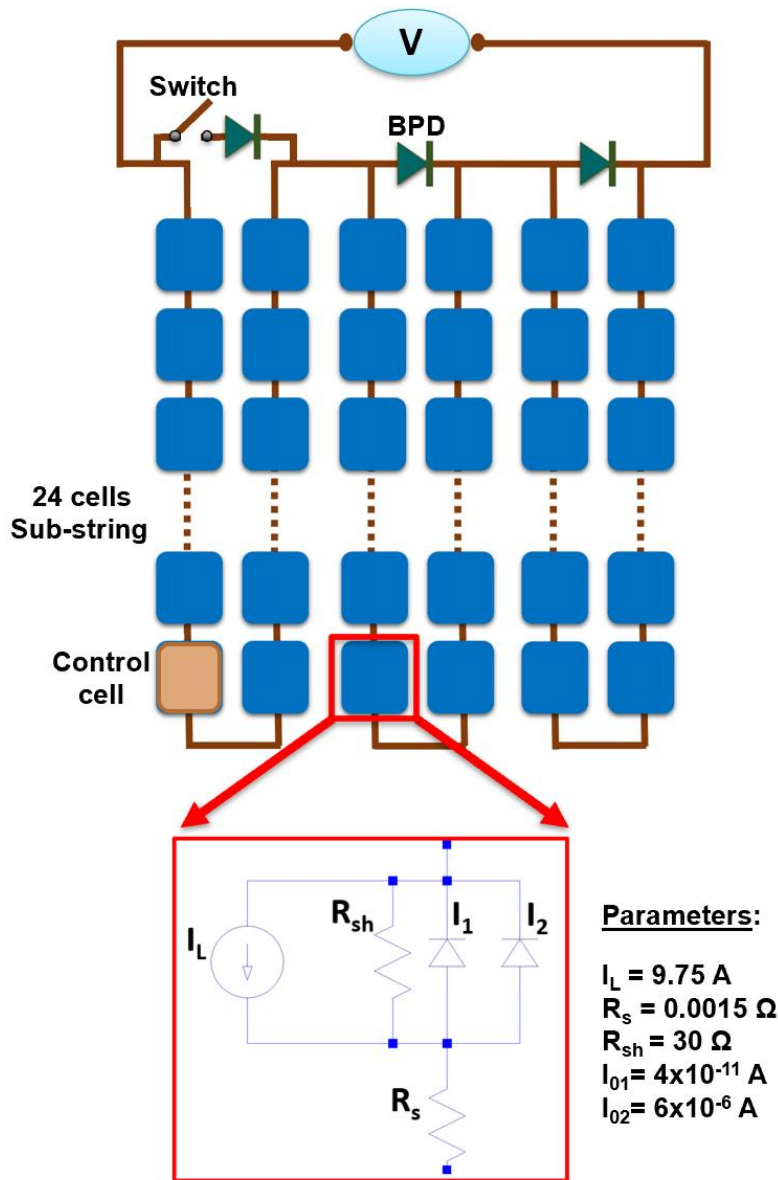


**Figure 3.10** Schematic of simulation used in LTSpice to understand the impact of OC BPD failure when the control cell illumination is changed.

In contrast, without BPD (equivalent to BPD in OC), shading of the control cell does not change the current through the sub-string, but instead, the shaded cell enters full reverse breakdown and the sub-string current (dashed blue line) remains constant. In this case, the PL emission from the test cells (dashed purple line) remains unchanged, thereby making the BPD OC failure detectable.

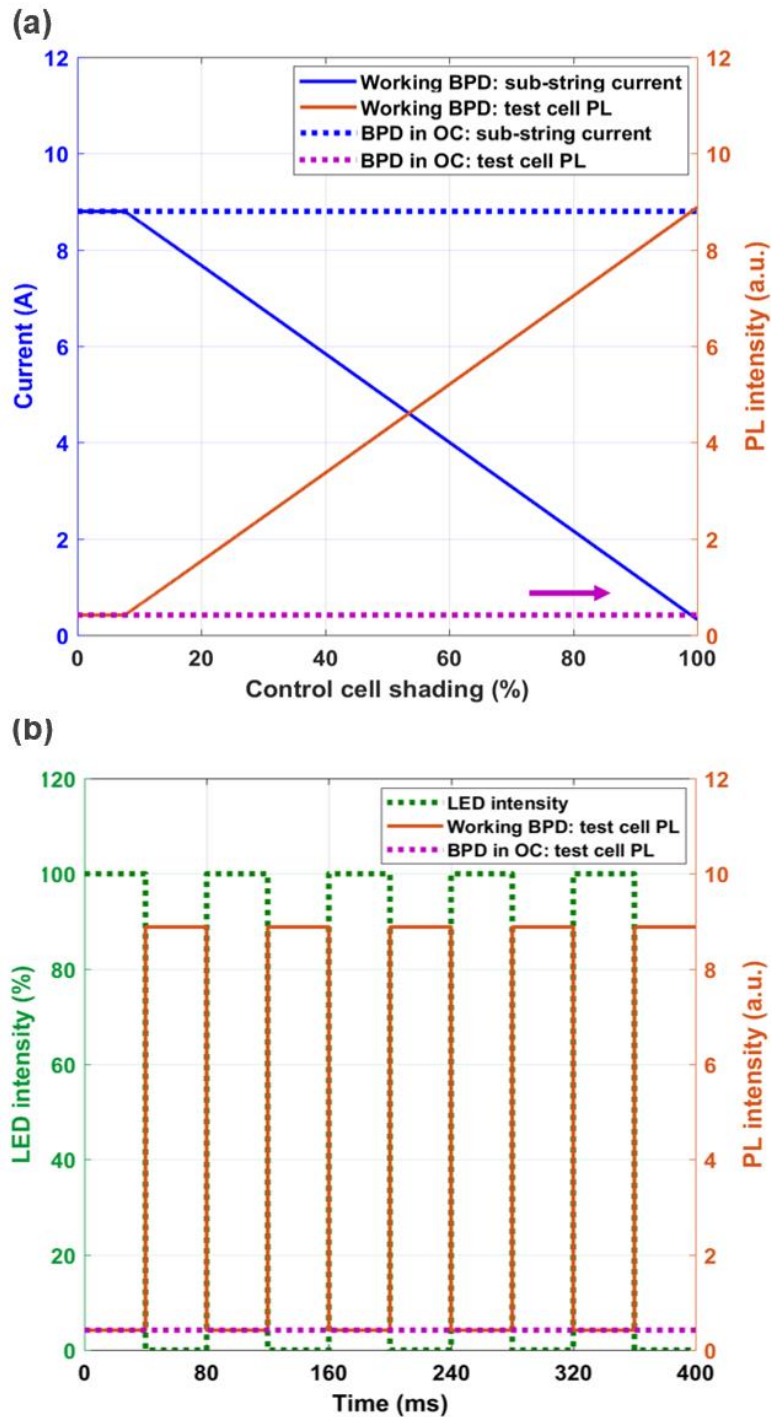


**Figure 3.11** (a) Sub-string current and PL intensity from test cells as a function of the shading fraction of the control cell with working BPD and BPD with OC failure; (b) test cell PL and control LED intensity as a function of time for *sequential* switching.

Figure 3.11(b) illustrates the resulting PL signal when the sub-string undergoes the *sequential* switching procedure with functioning BPD (solid orange line) and with BPD in OC failure (dashed purple line). In the presence of a functional BPD, the modulation of the control cell modulates the luminescence emission from the test cells between ~99% (similar to the emission at OC) and ~5% of the maximum PL emission (equivalent to the emission at MPP). On the other hand, with the BPD failed in OC, the luminescence from the test cells remains unchanged at ~5%, resulting in zero PL signal in a outdoor PL image.

#### 3.5.2 Experiment

The proposed BPD OC failure test is experimentally demonstrated outdoors under full sun-light using a nine cell mini-module, by connecting and disconnecting a BPD across its terminals as shown in Figure 3.12. During the tests, the module is operated at its  $I_{MPP}$  using an electronic load [161]. The PL emission is measured from one of the test cells using an InGaAs photodiode with the bandpass filtering (1125-1150 nm) and a current pre-amplifier, as spatial information is not required for this test. The results, as displayed in Figure 3.13, agrees well with the modelling shown in Figure 3.11(b). Note that when the LED is ON, the measured intensity (~4.26 a.u.) is the sum of PL intensity at  $I_{MPP,system}$  (~5% PL compared to the maximum PL at  $V_{oc}$ ) and the large constant ambient signal that reaches the detector.

Additionally to the approach using an InGaAs photodiode the BPD failure identification is also demonstrated using outdoor PL imaging as shown in Figure 3.14. The experimental data confirm the modelling as no PL signal is measured from the *test cells* with the BPD absent (or in OC).

In summary, OC BPD failure reveals itself during outdoor PL imaging through the inability to contactlessly switch the sub-string from MPP to any other biasing condition and the resulting lack of PL in the difference image. Compared to the existing methods discussed in Chapter 2, this method is cost-effective and is easily applied as it is contactless. Note that the PL imaging technique proposed here is not capable of detecting BPD failed in SC.

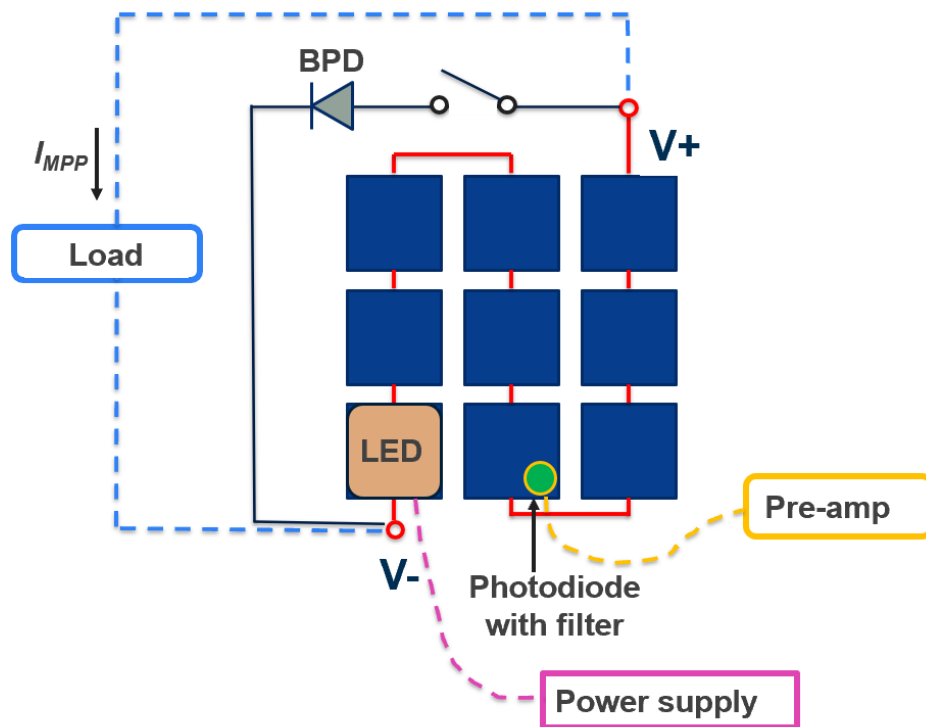


**Figure 3.12** Experimental setup for OC BPD testing using a photodiode.

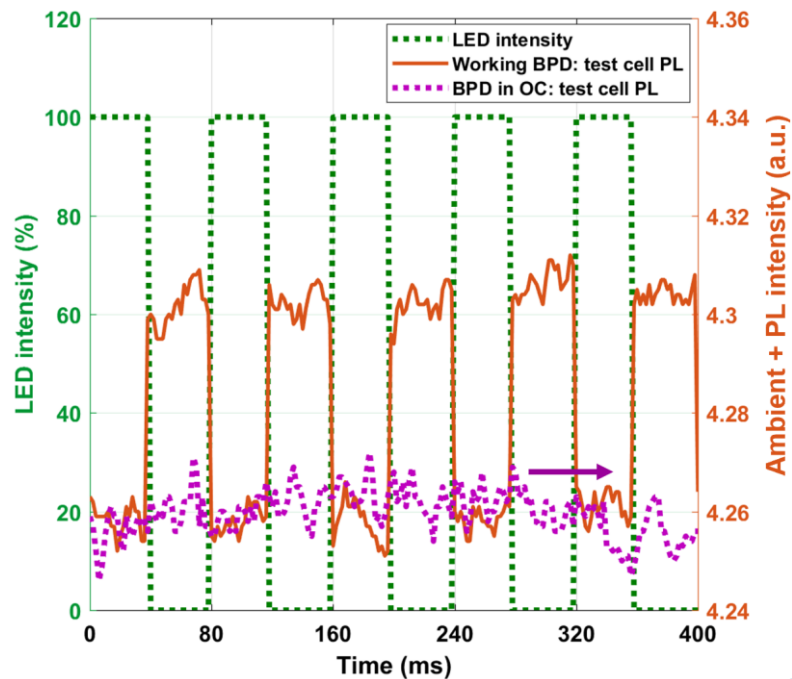


**Figure 3.13** Test cell signal (PL + diffusely reflected ambient sunlight) and control LED intensity, as a function of time during *sequential* switching. The measurement is performed using a mini module with BPD (a) working and (b) failed in OC condition.



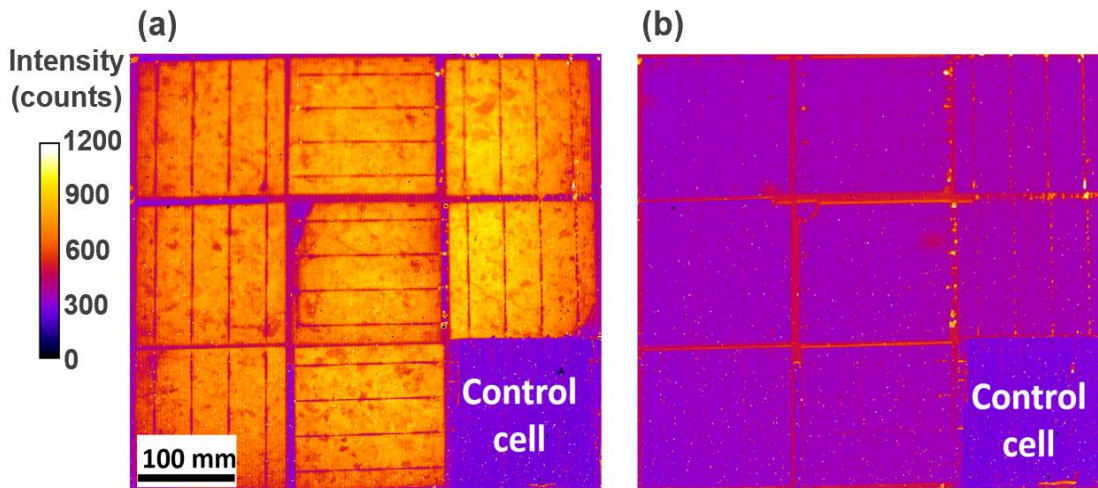


**Figure 3.14** Outdoor PL image of a test module with bypass diode (a) intact and (b) failed in OC condition.

### 3.6 Impact of module-level power electronics

String and central inverters are commonly used in large scale PV power systems [163], as discussed in Chapter 2. MLPE, including micro-inverters and DC-DC power optimizers, have become popular for systems with partial shading issues due to their ability to maximize the system power output [164]. Since modules incorporating these technologies are more resilient to power loss and hot-spot formation under partial shading conditions, they are commonly used in roof-top systems and systems that are likely to be affected by shading [35].



**Figure 3.15** Outdoor PL testing on 12 kW east-west facing solar array in Australia.

If a string or a central inverter is connected to a large-scale PV system, it may not react to the loss of a third of a single module power (shading of the control cell in a sub-string), since the MPP tracking is done at the string level or system level. Thus, with these types of inverters, the proposed approach of *sequential* measurement is expected to work well.

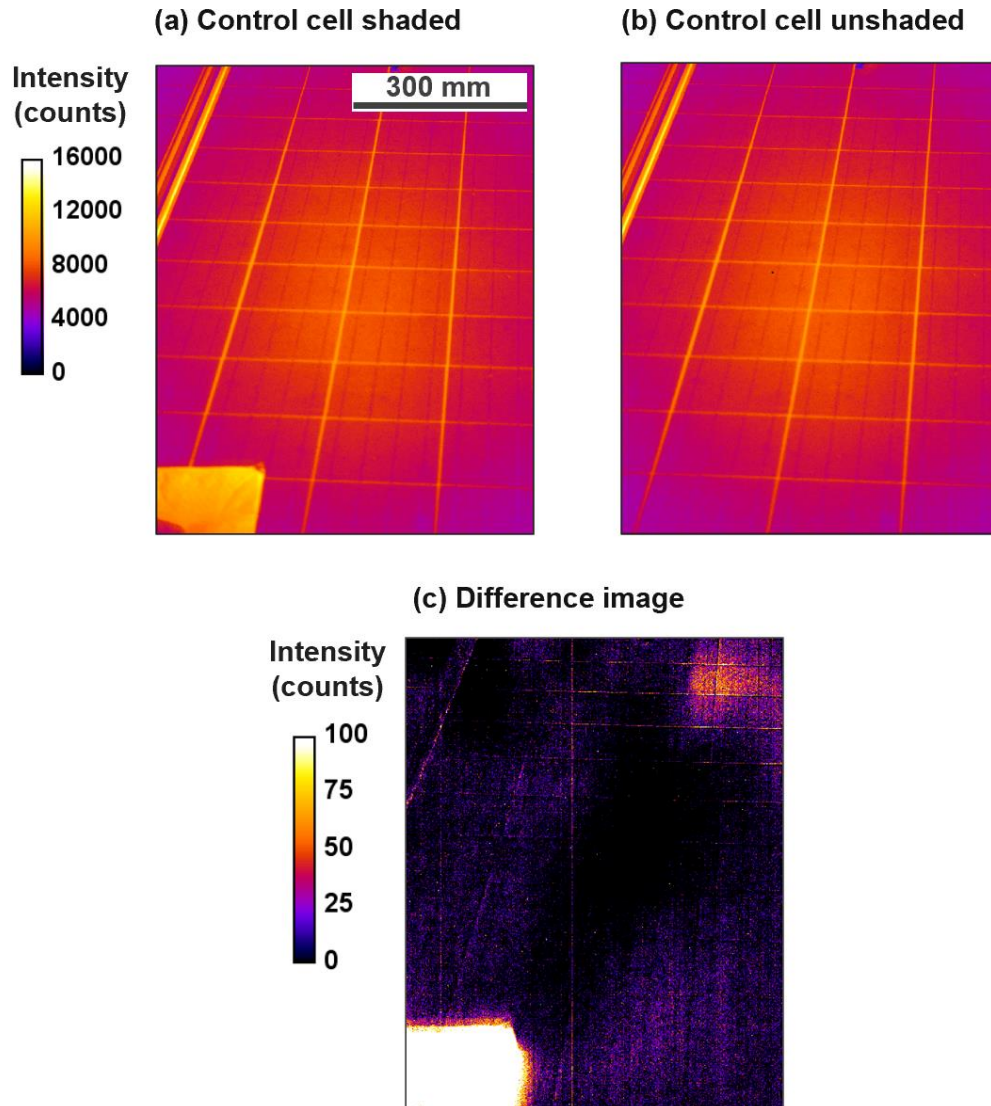


**Figure 3.16** Image captured by the outdoor PL system while the control cell is (a) shaded and (b) unshaded and their corresponding (c) difference image.

To test the developed method with MLPE, measurements are done using a 5B [165] east-west facing 12 kW foldable solar array consisting of mc-Si PERC module, as shown in Figure 3.15. The system consisted of two 5 kW string inverters [166] and a DC-DC power optimizer [167] connected to each module. The images captured by the system are shown in Figure 3.16, while the control cell is shaded and unshaded using a baffle. It seems the developed outdoor method is unable to provide high-quality outdoor PL images of this particular PV system. Note that different scales are used in this figure. Although

the baffle looks bright in the difference image, its mean intensity counts are just ~95 counts.

To investigate the applicability of the *sequential* measurement in the case of systems with MLPE, the terminal current of a 190 W mono-Si Al-BSF module connected to a micro-inverter (UNIV-M248 from Suzhou Universal-Power [168]) is measured while the LED placed on the control cell is switched from ON to OFF and back to ON (Figure 3.17). When the LED is turned OFF, the module current switches to zero essentially instantly. However, when the LED is turned ON again, it takes approximately six seconds for the current to reach MPP. Note that the noise in Figure 3.17 in the measured current might be due to the micro-inverter electronics constantly tracking the MPP of the module. The current drop to zero is attributed to the internal safety features of the microinverter. However, switching the LED to ON (similar to un-shading the control cell) doesn't allow the module to return to its MPP condition instantaneously. This could be because as such a dramatic and instantaneous change in MPP requires the MLPE to perform a global rather than a local MPP sweep. Such a long delay and the possible change in ambient sunlight condition in this time frame, makes the previously proposed *sequential* measurement technique (with a typical LED switching time of 40 ms) incompatible with systems with MLPE.

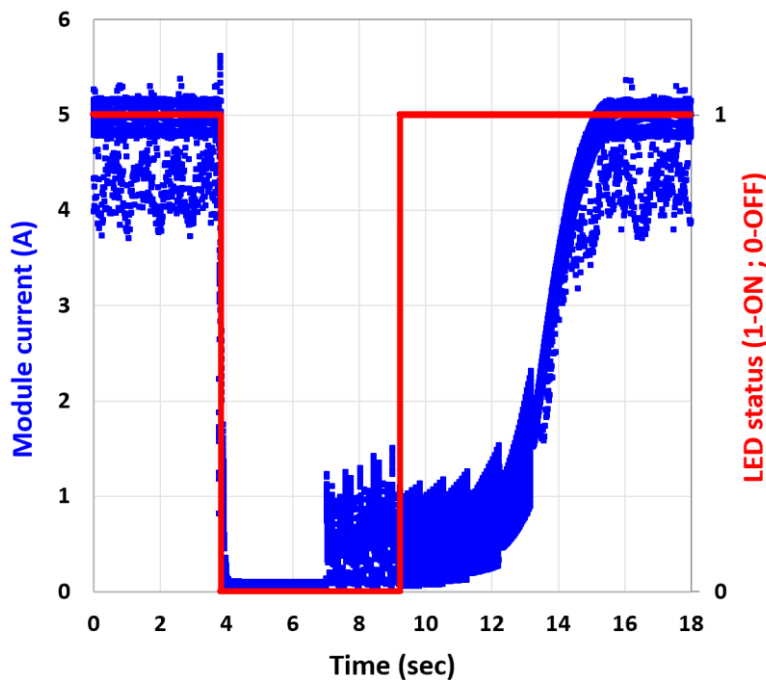


**Figure 3.17** The current output of an Al-BSF module connected to a micro-inverter when the LED on top of the control cell is switched from ON to OFF and back to ON.



### 3.7 Chapter summary

This chapter described the methodology, design and development of a novel outdoor PL imaging system that can acquire PL images of solar modules during daylight conditions in a contactless manner. It is also presented how PL emission on field installed solar modules can be used to detect BPD OC failure in the field with a cost effective and simple method. Finally, a problem of onboard electronics of MLPE is discussed in the context of not allowing the switching between OC to MPP, as required by the proposed method.

To overcome this problem, the next chapter proposes a new contactless method called *batch* measurement. This measurement approach is simpler to apply than the *sequential* method and is expected to work with all types of electronics currently used for implementing MPP tracking and DC to AC conversion.

### 3 Outdoor photoluminescence imaging

## Chapter 4

# Batch measurement of outdoor photoluminescence imaging: Technical considerations and applications<sup>2</sup>

This chapter proposes a simplified approach for outdoor PL imaging, called *batch* measurement. This approach overcomes some of the problems of the *sequential* approach presented in the previous chapter, including its main limitation of being incompatible with PV systems featuring module-level maximum power point tracking. The obtained image quality by the two approaches is analysed quantitatively and compared with the standard EL method. This chapter also investigates the impact of several factors, such as time of day of the measurement,  $V_{oc}$  and  $R_{sh}$  of the control cell. Additionally, it discusses the use of the proposed technique to quantify  $R_s$  losses in PV modules. Finally, the method is demonstrated using a solar race car and outdoor imaging of modules.

### 4.1 Methodology

For the *sequential* measurement explained in Chapter 3, the operating condition of the module is switched between two consecutive images. In contrast, for the *batch*

---

<sup>2</sup> This Chapter is partially based on:

**Bhoopathy, R.**, Kunz, O., Juhl, M., Trupke, T. and Hameiri, Z., “Inspecting series resistance effects and bypass diode failure using contactless outdoor photoluminescence imaging” in 7th World Conference on Photovoltaic Energy Conversion, pp. 0377-0380, 2018.

**Bhoopathy, R.**, Kunz, O., Juhl, M., Trupke, T. and Hameiri, Z., “Photoluminescence based characterization techniques for photovoltaic modules in the field” in 28th Annual NREL Silicon Workshop, 2018.

**Bhoopathy, R.**, Kunz, O., Juhl, M., Trupke, T. and Hameiri, Z., “Photoluminescence imaging of field deployed modules using contactless switching” in Asia Pacific Solar Research Conference, 2018.

**Bhoopathy, R.**, Kunz, O., Juhl, M., Trupke, T. and Hameiri, Z., “A simplified contactless method for outdoor photoluminescence imaging” in 46th IEEE Photovoltaic Specialists Conference, pp. 2571-2574, 2019.

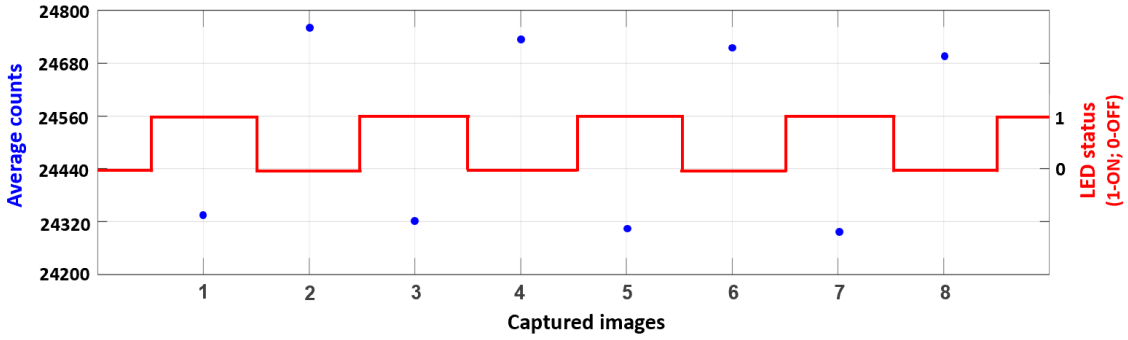
**Bhoopathy, R.**, Kunz, O., Juhl, M., Trupke, T. and Hameiri, Z., “Outdoor photoluminescence imaging of solar panels by contactless switching: Technical considerations and applications” Progress in Photovoltaics: Research and Applications, 28(3), pp.217-228, 2019.

#### 4 Batch measurement of outdoor photoluminescence imaging

measurement, the first set of images is taken when the control cell is illuminated, while the second set of images is taken when it is shaded. In this approach, the test cells are switched *only once* from MPP (or any other operating point) to OC to create the final image. The final outdoor PL image is obtained from the difference between the average of all images taken with the LED OFF (test cells in OC condition) and the average of all images taken with the LED ON (test cells in MPP condition) equivalent to the *sequential* approach.

The difference between the two measurement approaches is illustrated in Figure 4.1 with the average pixel counts calculated from eight images using a mono-Si PERC module with a cell  $V_{oc}$  of 660 mV (as used before in Section 3.4).

(a) Sequential measurement



(b) Batch measurement

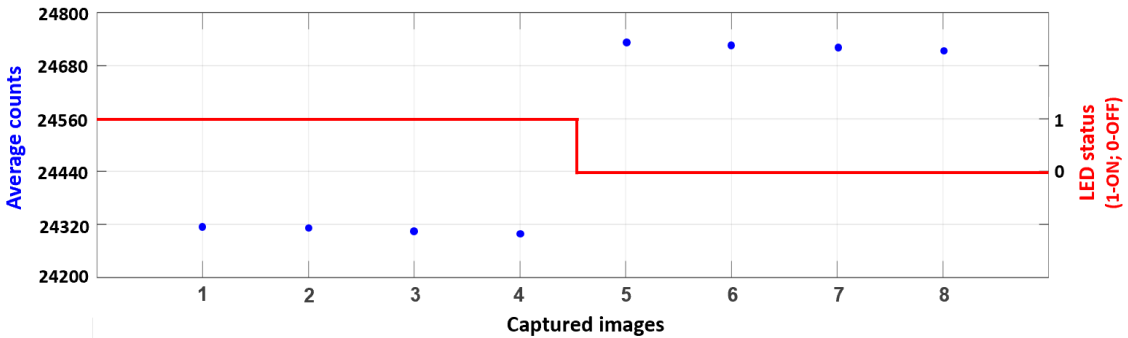


**Figure 4.1** Average pixel counts (blue circles) from the module area obtained from (a) *sequential* and (b) *batch* measurements with the corresponding LED status. Note that LED ON corresponds to MPP and LED OFF to OC condition, respectively.

The average pixel counts while the LED is ON (around 24,320 counts) is proportional to the diffuse ambient sunlight reflected from the module during the measurement. The additional average pixel counts (around 420 counts) observed when the LED is OFF compared to the case when the LED is ON, is due to the emitted PL signal at OC condition, as observed before in Figure 3.10(a). From the data, the PL component is calculated as

~5% which is the difference between two images measured with LED is ON and LED is OFF, respectively divided by the bias offset corrected signal in a single image:

$$\frac{420}{24320 - 16499} \times 100 = 5.37\% \quad (4.1)$$

The bias offset (16499 counts) presented in Equation 4.1 is explained in detail including its measurement procedure in Section 4.3. However, this component can differ significantly depending on various factors as will be discussed in Section 4.5.

A qualitative comparison of the image results between the proposed methods is provided in the next section.

## 4.2 Comparison between sequential and batch measurement

The two proposed measurement approaches are compared in this section using the mono-Si PERC module from Section 3.4.

To ensure a valid comparison between both approaches, a single image dataset of 400 images obtained at close to one Sun illumination condition using the *sequential* measurement approach (*Sequential* parent data) is used. From this dataset, two subsets of 200 images are selected to reproduce (a) a *sequential* and (b) a *batch* measurement data set. During the measurement, the module current is kept constant at  $I_{MPP}$  of the unshaded module while the test cells are modulated by the control cell illumination between OC and MPP. The average pixel counts (average signal from all test cells) from the parent *sequential* dataset and constructed *sequential* and *batch* subsets are shown in Figure 4.2 as a function of the number of captured images. The close-up shown in the bottom graph corresponds to the ten captured images on either side of the central switching point (indicated by the vertical purple dashed line in Figure 4.2).

To assess the image quality, outdoor PL images were determined from each of the constructed datasets (*sequential* and *batch*) of 100 image pairs from the difference between the average of all images taken with the LED OFF and the average of all images taken with the LED ON. The constructed datasets and the corresponding outdoor PL images are shown in Figure 4.3 displayed on the same intensity scale. For *batch* mode, the resultant outdoor PL image is significantly darker than the image obtained in *Sequential* mode. This intensity offset is caused by the variation in sunlight intensity (decreasing intensity) during the measurement, impacting the individual image intensities which in turn changes the intensity of the final outdoor PL image. The pixel values along

#### 4 Batch measurement of outdoor photoluminescence imaging

a cross-section of each image (as marked in Figure 4.3) are shown in Figure 4.4. The figure reveals a difference of about 50% between the *Sequential* and *Batch* measurements. This effect can be easily corrected for as will be demonstrated below.

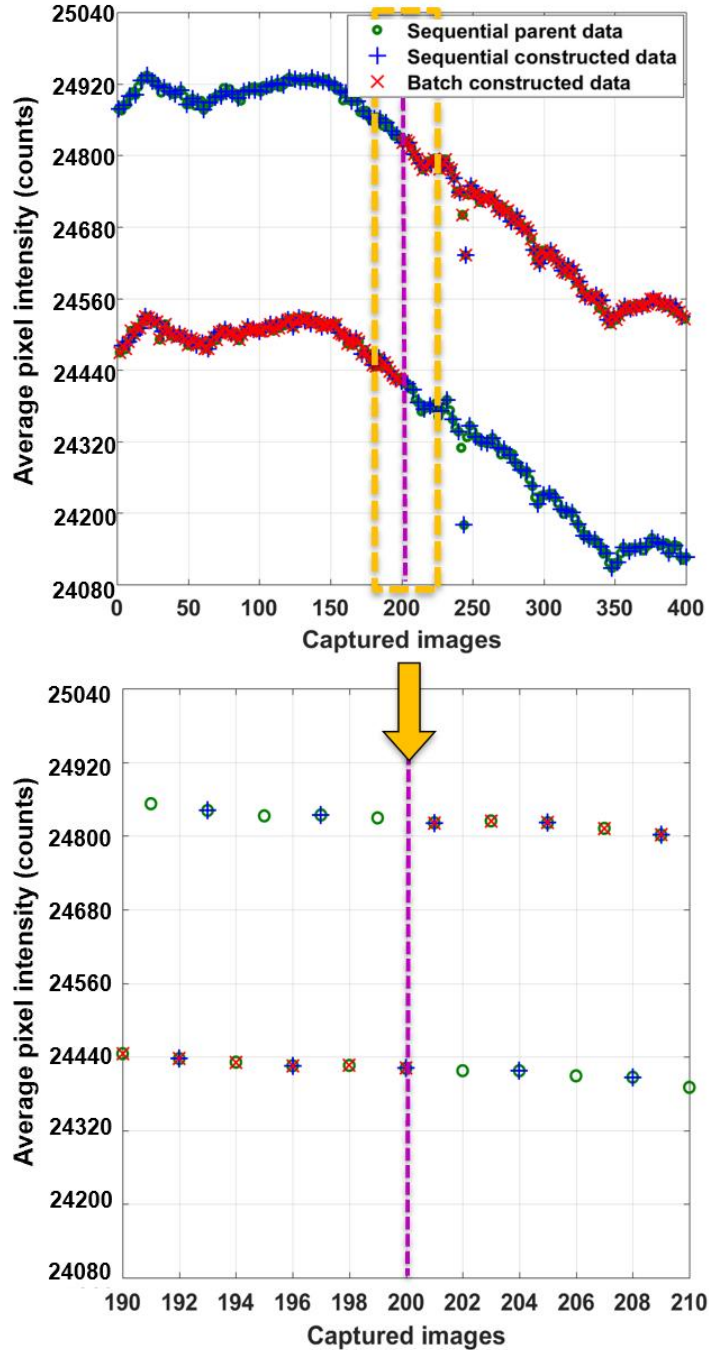


**Figure 4.2** Measured average pixel counts of captured images during the parent *sequential* dataset (green circles) from which the *sequential* (blue pluses) and *batch* (red crosses) measurement data sets with equivalent sunlight conditions are constructed. The bottom plot represents a close-up of the top plot with ten captured images on either side of the central switching point indicated by the purple dashed line.

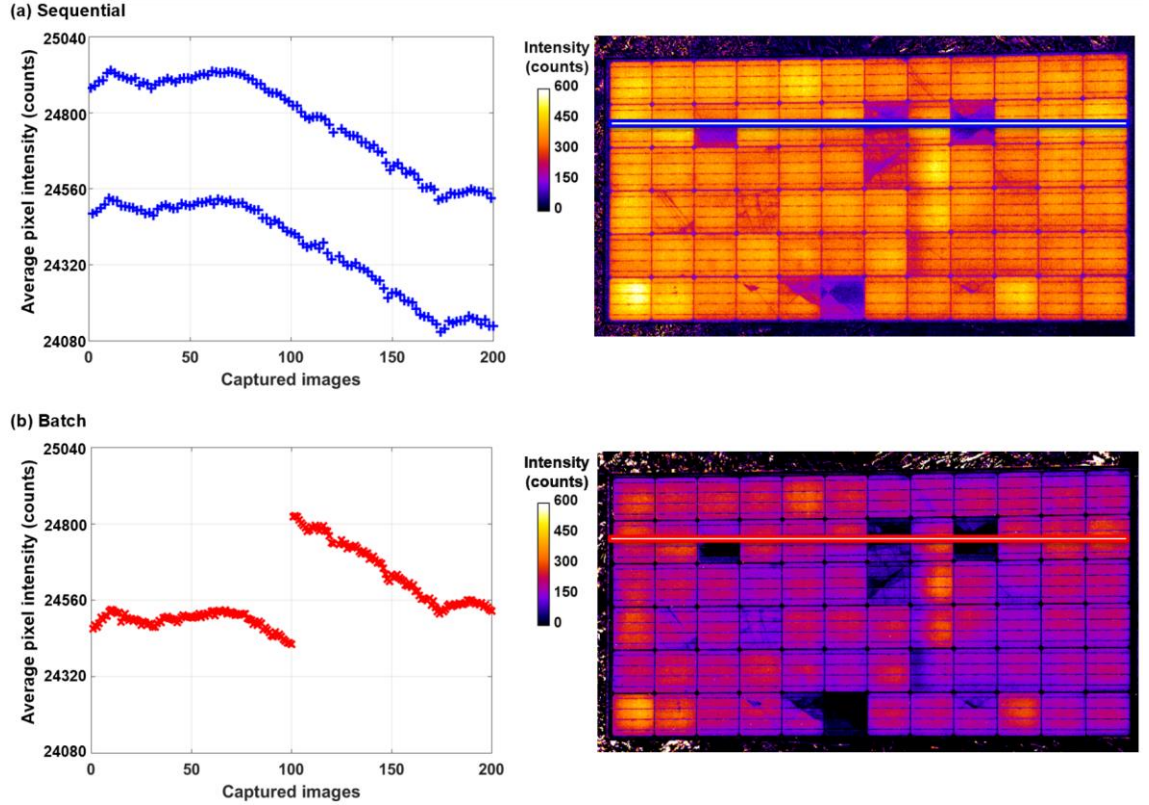


**Figure 4.3** Measured average pixel counts of captured images (left) and the corresponding outdoor PL images (right) taken using (a) *sequential* and (b) *batch* methods for 100 image-pairs.

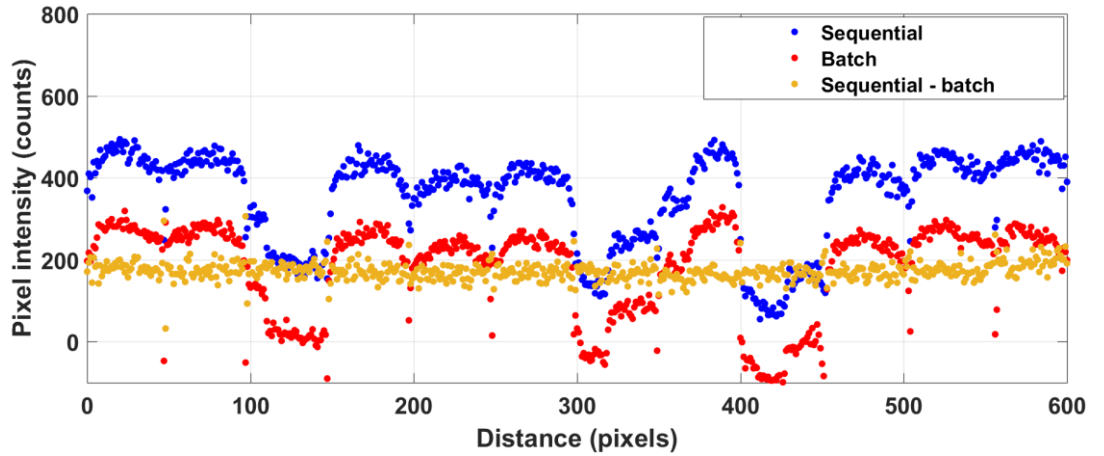


**Figure 4.4** Average pixel value across the highlighted cross-sections (blue and red lines) of the *batch* and *sequential* outdoor PL images in Figure 4.3 (right).

The changes in sunlight intensities during the measurement can be corrected for by dividing each individual image by an *intensity correction factor (ICF)* resulting in an “*offset corrected batch*” measurement as shown in Figure 4.5.

The *ICF* is calculated for the  $i^{th}$  image as the ratio between the average pixel count of the  $i^{th}$  image,  $S_{i\_i}$ , and the average pixel count of all the captured images after subtracting the camera bias offset (as will be explained in Section 4.3), considering only an



#### 4 Batch measurement of outdoor photoluminescence imaging

*unmodulated* module area. Note that the term *unmodulated* refers to an area in the image from which luminescence emission is not expected, e.g. the backsheet between cells or areas of unmodulated sub-strings. The signal from these areas is a direct measure of the ambient sunlight intensity.

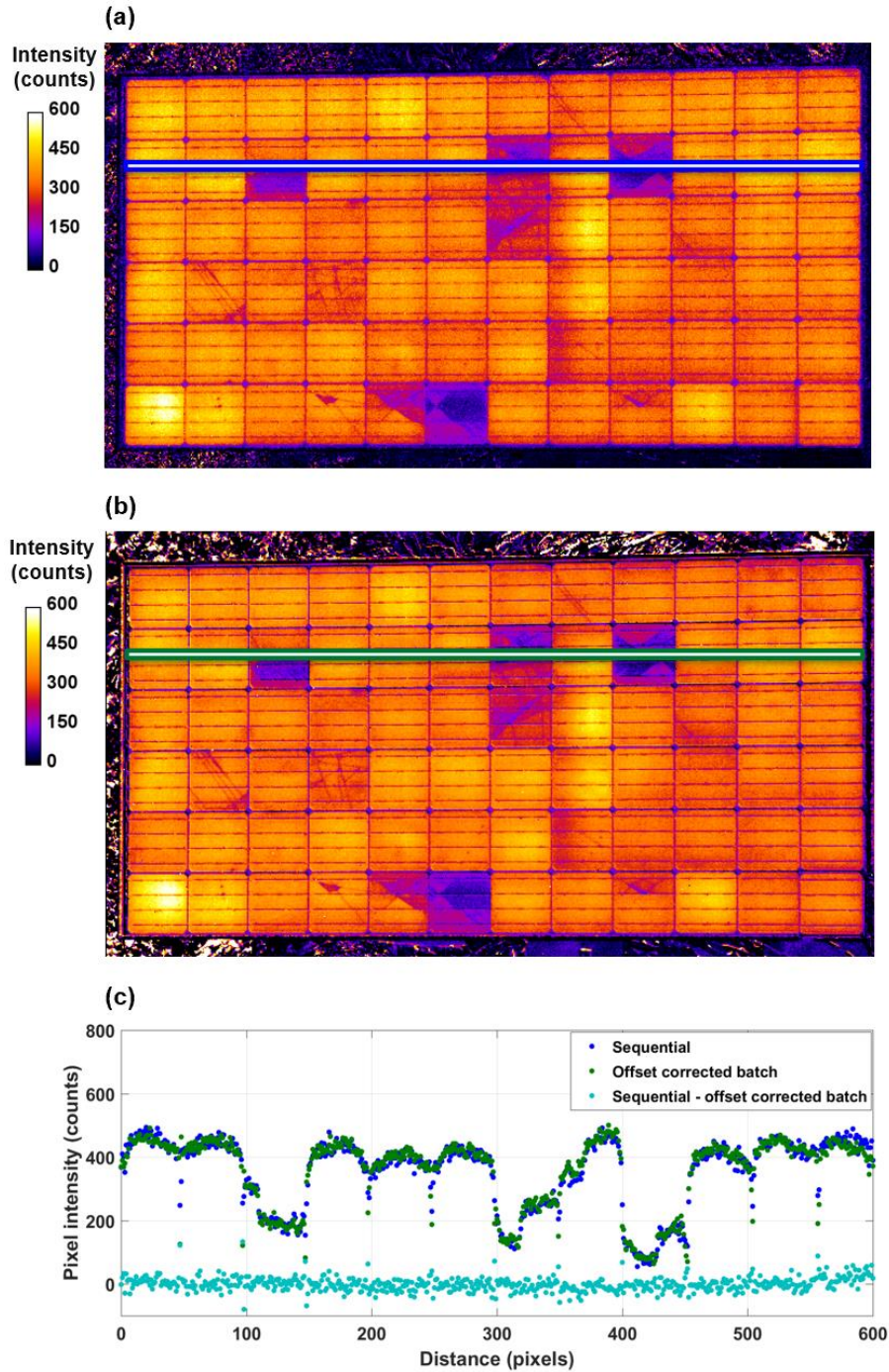


**Figure 4.5** Outdoor PL images resulting from (a) *sequential* and (b) *offset corrected batch* measurement for 100 image-pairs with their respective (c) average pixel value across the shown cross-sections highlighted in (a) and (b).



The following formula is used to calculate the *ICF* for the  $i^{th}$  image in the sequence, where  $(x,y)$  is the pixel index of the unmodulated image area with  $a \times b$  pixels:

$$ICF_i = \frac{\sum_{x=1}^a \sum_{y=1}^b S_{t,i}(x,y)}{\frac{1}{n} \sum_{j=1}^n \sum_{x=1}^a \sum_{y=1}^b S_{t,j}(x,y)}, \quad (4.2)$$

where  $n$  is the total number of images. Alternatively, the sunlight factor can be calculated using a reference detector constantly recording sunlight changes during the measurement. This offset could be minimised for a certain number of image-pairs by using a camera with a higher frame rate which will reduce the time interval between the consecutive image acquisition.

The image quality of the outdoor PL images obtained by these two measurement approaches is quantitatively compared in the following sections.

### 4.3 Determination of camera noise parameters

Signal to noise ratio (SNR) is a common metric used for evaluating and assessing image quality. For estimating the SNR of an image, quantification of the different noise sources and their contribution to the total noise are essential. This section aims to quantify the different noise parameters of the Xeva-1713 InGaAs camera used in this study [158]. Note that this camera is an old Xenics infrared camera and thus the camera specifications by the manufacturer is unavailable. The detailed noise analysis procedure presented here can be followed for noise quantification of other cameras used for indoor and outdoor imaging applications.

The photons incident on the camera detector generates the so-called *photoelectrons* that are converted to grey level digital units (counts) by an electronic readout circuit (amplifier) and the analogue-to-digital converter (ADC). The ratio of the number of photoelectrons and the counts is referred to as the *gain* that is commonly measured in units of electrons per count. In reality, the photoelectrons are not converted into the same number of grey levels making counts impractical for quantifying signal. Therefore, quantifying the signal in terms of photoelectrons (e) is recommended as these are real-world values for intensity measurement that allow consistent signal comparison between different types of cameras [169].

Noise in the acquired image can be classified into three different components as listed below:

#### 4 Batch measurement of outdoor photoluminescence imaging

1. Read noise,  $\sigma_{ro}$ : The noise is introduced due to the variability associated with the process of converting the photoelectrons to digital counts [169].
2. Shot noise,  $\sigma_s$ : Photons constituting the signal arriving one by one at random intervals constituting the signal and thus, carry a statistical variation in their arrival rate, known as shot noise [170]. This noise follows a Poisson distribution exhibiting a square root relationship between the signal and noise [169]. The relationship is given by  $\sigma_s^2 = \Phi_s t_{exp}$ , where  $\Phi_s$  is the flux in e/s of the measured signal and  $t_{exp}$  is the image exposure time in seconds. In essence, for a particular image, the shot noise in each pixel is given as the square root of the total number of photoelectrons.
3. Dark noise,  $\sigma_d$ : Due to thermal excitation, electrons are also generated within the camera sensor in the dark. The associated signal is independent of the light falling on the sensor and still contributing to the brightness of an image [170]. The temperature of the camera chip has a strong impact on the dark current. Cooling the chip reduces the dark current, thereby lowering the associated dark noise and total noise. In an ideal case, the dark signal can be sufficiently reduced, so that the light signal significantly exceeds it, reducing or eliminating its impact. The dark noise also follows Poisson distribution and therefore, its variance is given by  $\sigma_d^2 = \Phi_d t_{exp}$ , where  $\Phi_d$  is the flux in e/s of thermally generated electrons created in the sensor [169].

The total noise in a camera is given by [169]:

$$\sigma = \sqrt{\sigma_s^2 + \sigma_d^2 + \sigma_{ro}^2} = \sqrt{\Phi_s t_{exp} + \Phi_d t_{exp} + \sigma_{ro}^2} \quad (4.3)$$

The camera offset bias represents the non-zero value of every pixel, even in the absence of light or dark signal. The camera offset bias is subtracted from the measured signal as it is present in any electronic data acquisition system that involves ADC and does not contribute to the measured signal [169]. This offset is typically large for InGaAs cameras [171]. Substituting  $\Phi_s t_{exp} + \Phi_d t_{exp} = S_t$ , which is the total signal measured by the camera after subtracting the camera offset bias for a specific  $t_{exp}$ , the total noise is given by:

$$\sigma = \sqrt{S_t + \sigma_{ro}^2} \quad (4.4)$$

The variance of a difference image ( $\sigma_{\text{diff}}$  in e) is calculated from two images of the same sample under identical imaging conditions taken in short succession and is given as the sum of the variances in both images:

$$\sigma_{\text{diff}}^2 = 2S_t + 2\sigma_{\text{ro}}^2 \quad (4.5)$$

Photoelectrons are converted to digital counts that are typically recorded by the computer (represented by suffix  $c$  in each of the terms below) by multiplying them with the camera gain,  $g$  ( $S_t = gS_{t_c}$ ):

$$g^2\sigma_{\text{diff}_c}^2 = 2gS_{t_c} + 2g^2\sigma_{\text{ro}_c}^2 \quad (4.6)$$

Simplifying the above equation:

$$\frac{\sigma_{\text{diff}_c}^2}{2} = \frac{S_{t_c}}{g} + \sigma_{\text{ro}_c}^2 \quad (4.7)$$

Thus, the slope and intercept of the linear relationship between the variance of difference images and the signal (in counts) acquired with different  $t_{\text{exp}}$  allows determination of  $1/g$  and  $\sigma_{\text{ro}_c}^2$  via a least-squares linear fitting procedure.

To find the offset bias of the used InGaAs camera [158], the mean dark signal from the dark image (no light is entering the camera) is obtained for different  $t_{\text{exp}}$ . The resulting data are plotted in Figure 4.6. From the slope and intercept,  $d$  and offset are found to be 8,772 counts/s and 15,863 counts, respectively. Note that all the following measurements were performed with a frame grabber [160] connected to the camera and the camera gain and temperature were set to the highest gain mode and -65 °C, respectively.

#### 4 Batch measurement of outdoor photoluminescence imaging

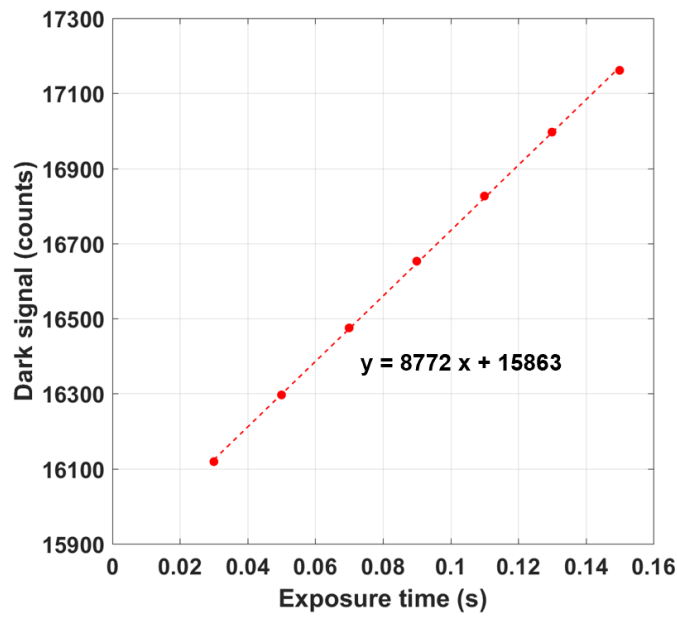


**Figure 4.6** Mean dark signal measured by InGaAs camera as a function of dark exposure time.

Subsequently,  $s_s$  can be determined in the same way, however, using EL emission from a relatively uniform solar cell without micro cracks and dislocations. The measurements are done with the camera without lens or filters by mounting the camera sensor right on top of the solar cell. This ensures that the solar cell is completely out of focus for the camera and illuminates the sensor homogeneously.

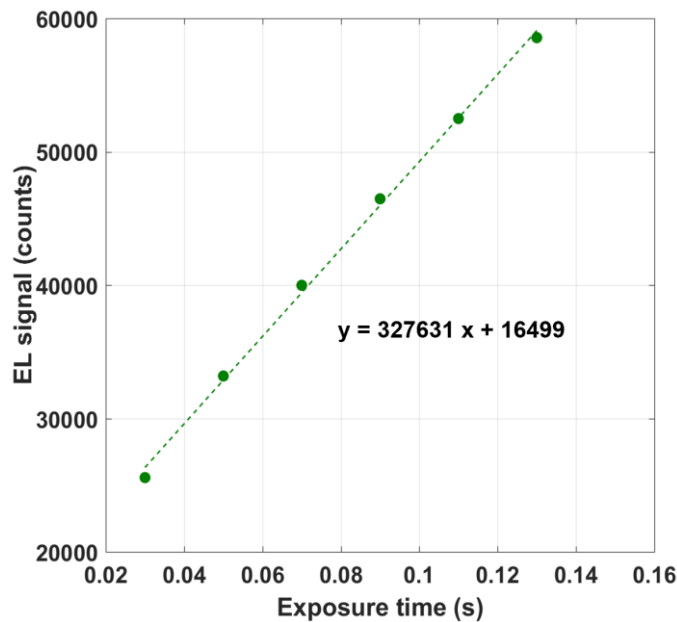


**Figure 4.7** Mean EL signal measured by InGaAs camera as a function of exposure time.

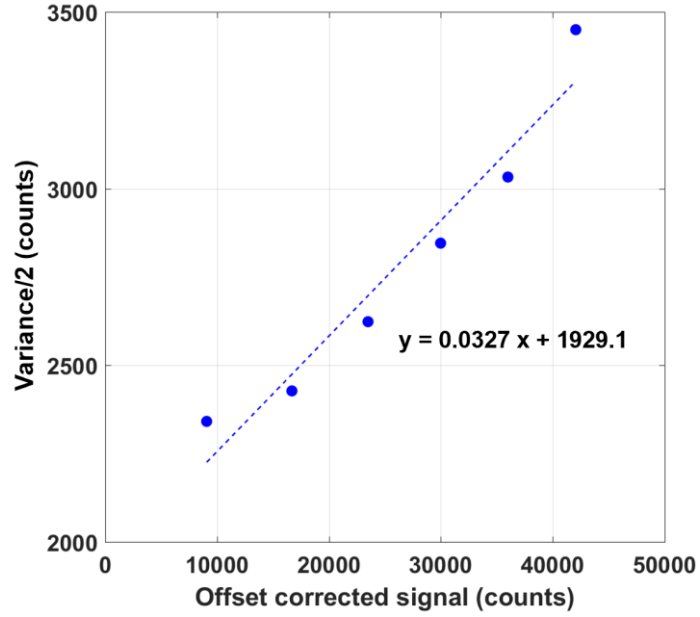


**Figure 4.8** Offset corrected mean signal as a function of the variance of the difference image measured from two EL images.

From the slope of the plot presented in Figure 4.7,  $s$  is found to be 327,631 counts/s. Note that the offset obtained from this plot (16,499 counts) is ~4% higher compared to that obtained from in Figure 4.6 which is attributed to a repeatability error as similar offsets are expected from both measurements. As the EL signal is stronger compared to the dark signal (in Figure 4.6), the linear fitting is more accurate and reliable and therefore the offset from the EL measurements is used for analysis.

The variance of a difference image is calculated using two images measured with identical exposure time divided by two as a function of the bias offset corrected signal in counts of the individual image  $S_{t_c}$  (EL signal – offset) is obtained for different  $t_{exp}$  and presented in Figure 4.8. From the slope and intercept, the  $g$  of the camera and  $\sigma_{ro}$  are found to be 30.58 e/counts and 43.92 counts, respectively (Equation 4.6). The determined readout noise is quite high, probably due to the high dynamic range of the sensor used in this camera [158]. This is posing a limitation in using this camera for outdoor PL imaging.

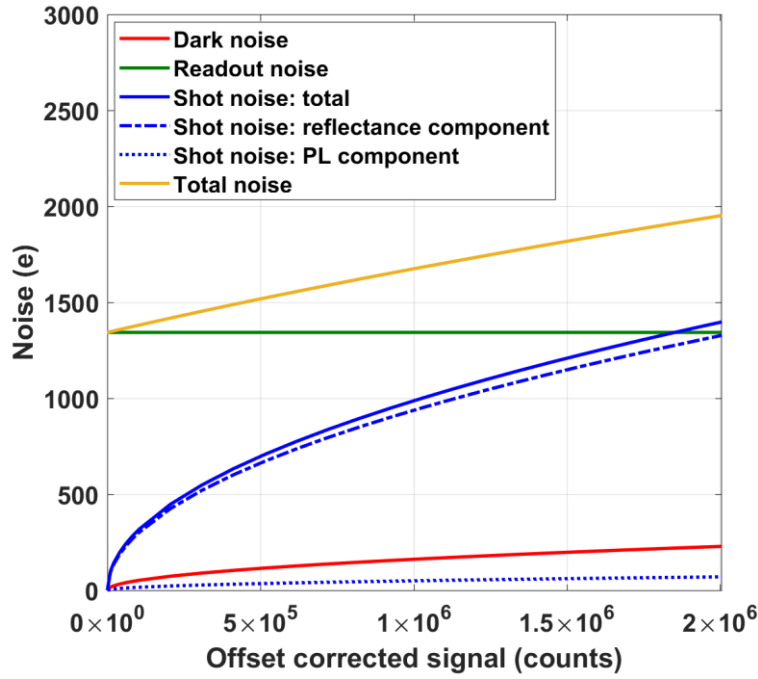


Figure 4.9 Different components of camera noise.

The measured camera parameters are summarized in Table 4.1. The different components of the total camera noise as a function of exposure time calculated from the summarized parameters are illustrated in Figure 4.9.

It is observed that the total noise is influenced mostly by the readout noise. Although the shot noise constitutes of emitted PL signal (PL component) and the diffuse ambient sunlight reflected from the module (reflectance component), it is mainly influenced by the reflectance component.

Table 4.1: Measured camera parameters

| Parameter     | Symbol        | Measured value                       |
|---------------|---------------|--------------------------------------|
| Gain          | $g$           | 31 e/counts                          |
| Offset        | $S_o$         | 504,539 e<br>(16,499 counts)         |
| Readout noise | $\sigma_{ro}$ | 1,343 e<br>(43.92 counts)            |
| Dark current  | $d$           | 268,248 e/s<br>(8,772 counts/s)      |
| Photocurrent  | $s$           | 10,018,956 e/s<br>(327,631 counts/s) |

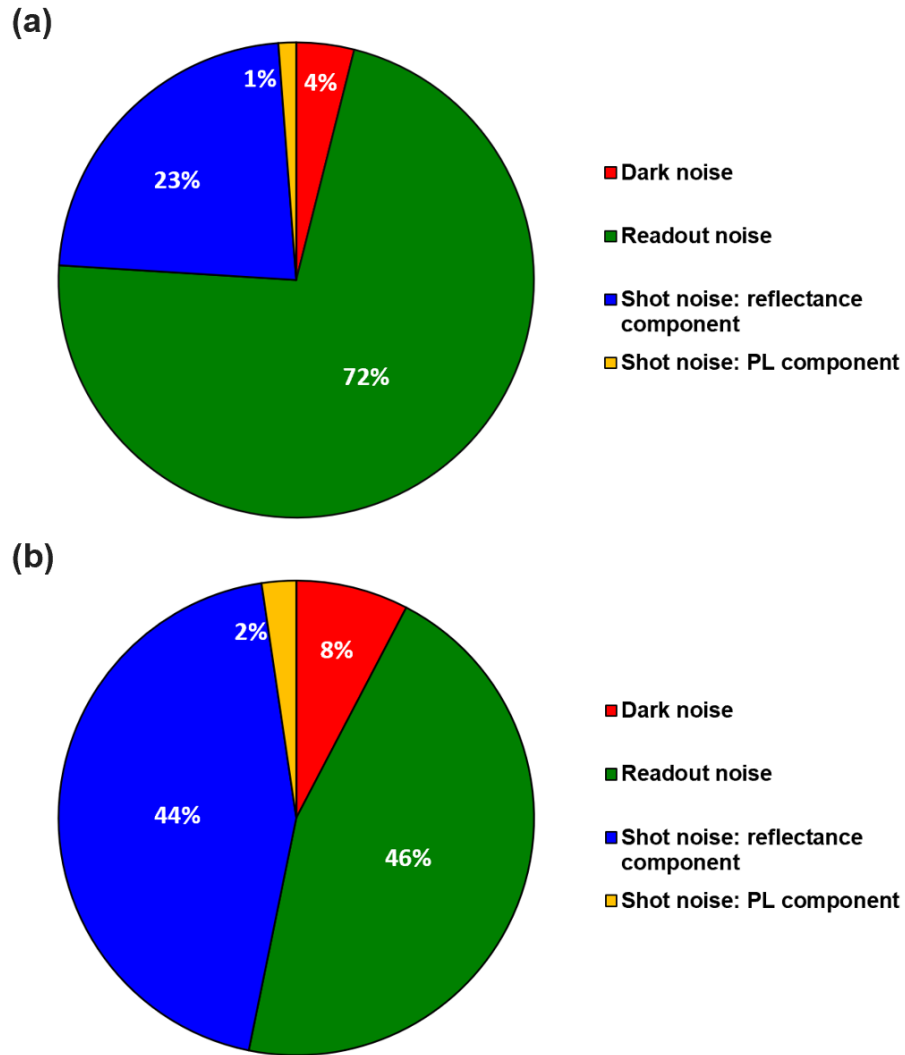


**Figure 4.10** Different components of noise in the image captured (a) in Figure 4.2 and (b) with a maximum count rate of 65,536 counts.

Figure 4.10 compares the contribution of each noise component to the total noise of the image captured when PL is present (LED OFF) for the maximum possible count rate. As can be seen, in this case, about two-thirds of the noise is due to the readout noise, followed by shot noise of the reflectance signal captured by the camera. Figure 4.2 also presents a case when the camera's maximum possible count rate of 65,536 counts is used for which both readout and shot noises contribute almost equally.

In summary, for this camera, the total noise is strongly dominated by the readout noise for images in which the signal is significantly below the maximum count rate of 65,536 counts (2,004,090 e, Figure 4.9). For the maximum count rate, the read noise and shot noise contribute about equally. To minimize the relative impact of the readout noise, it is recommended to use the maximum possible range without saturating the sensor, minimizing the number of image-pairs captured.

#### 4.4 Determination of SNR for outdoor PL images

The signal in the outdoor PL images is given by the difference in  $S_t$  between images corresponding to LED OFF ( $S_{t\_OFF}$ ) and LED ON ( $S_{t\_ON}$ ) conditions, as this represents the PL signal. Therefore, the SNR for single and  $n$  image-pairs considering a pixel in outdoor PL images is given as [169]:

$$SNR_1 = \frac{S_{t\_OFF} - S_{t\_ON}}{\sqrt{S_{t\_OFF} + S_{t\_ON} + 2\sigma_{ro}^2}} \quad (4.8)$$

$$SNR_n = \frac{\sum_{i=1}^n (S_{t\_OFF,i} - S_{t\_ON,i})}{\sqrt{\sum_{i=1}^n (S_{t\_OFF,i} + S_{t\_ON,i}) + 2n\sigma_{ro}^2}} \quad (4.9)$$

where the numerator and denominator represent the signal and noise (from Equation 4.4), respectively. Note that in the above equations,  $S_{t\_OFF}$  and  $S_{t\_ON}$  represent the signal in photoelectrons after offset correction as discussed before.

In the case of outdoor PL images, the signal is influenced by the PL emission from the module that changes linearly with changes in the incident light intensity (as will be investigated in Section 4.5.1) and is exponentially related to the cell  $V_{oc}$  (Section 4.5.2).

The signal, noise and hence, SNR estimated for the *sequential*, *batch* and *offset corrected batch* approaches (corresponding to the data set of Figure 4.2) are shown as a function of the number of image-pairs in Figure 4.11. Note that increasing image-pairs is considered from the switching point outwards for all three approaches: for  $n$  image-pairs,  $n/2$  images from the left and right of the switching point are considered.

The noise from all three methods is the same since they all have the same measurement conditions, thus, having the same dark, shot and readout noises. The dashed black line indicates the minimum acceptable SNR for industrial and process control outdoor imaging as suggested by the IEC standard [79]. It seems that only 7, 9 and 15 image-pairs are required to achieve this IEC's requirement for *sequential*, *batch* and *offset corrected batch* measurements, respectively. This just takes 560, 720 and 1,200 ms of acquisition time.



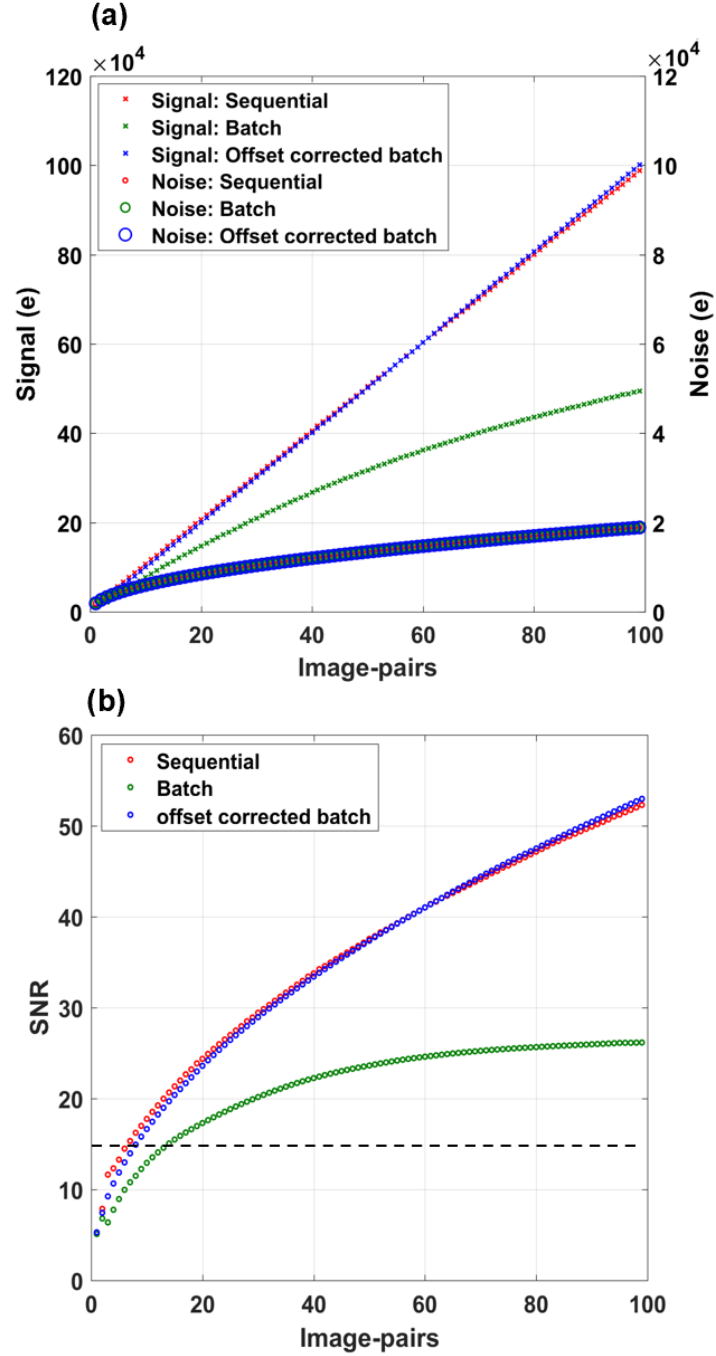


**Figure 4.11** (a) Signal and noise, and (b) SNR as a function of the number of evaluated image-pairs. The dashed line in (b) represents the minimum acceptable SNR for outdoor imaging as suggested by the IEC standard [79].

Although the image quality seems similar (Figure 4.3), the SNR of the *batch* measurements is lower than that of the corresponding *sequential* measurements. This is because of the lower PL signal in the *batch* measurements, as the sunlight intensity was reduced during this specific measurement. Note that if the sunlight had increased, the opposite would be observed, i.e. a higher SNR for the *batch* measurements. This impact

on SNR is a pure artefact as the actual noise in all three approaches is similar and SNR reflects the offset due to sunlight intensity that can be corrected.

As discussed above the *sequential* measurement has the advantage of being more robust to sunlight intensity changes, however, it has a severe limitation of not being applicable to systems with module-level MPP tracking. It seems that the *offset corrected batch* measurement overcomes this limitation and has the added advantage of being relatively simple and convenient compared with the sequential approach, as it removes the complexity of synchronizing the camera image acquisition with the irradiance switching on the control cell. Therefore, for the rest of the thesis, all the outdoor PL imaging measurements are performed using the *offset corrected batch* measurement approach, unless specified.

### 4.5 Impact of different factors on outdoor PL image quality

In this section, the impact of different factors, such as incident light intensity, cell  $V_{oc}$  and control cell shunting, on the obtained SNR of outdoor PL images is investigated. During these measurements, the test cells are modulated between OC and SC conditions. Note that as the image-pairs are obtained in close intervals, the subtracted PL image is insensitive to temperature.

#### 4.5.1 Impact of incident sunlight intensity

In order to investigate the impact of the sunlight intensity on the SNR, an encapsulated multi-Si PERC solar cell with a cell  $V_{oc}$  of 655 mV is used (Figure 4.12). The measurements were performed throughout a sunny day (25<sup>th</sup> of March in Sydney), while the cell is mounted at a fixed tilt angle of approximately 34° facing north. The measurements were performed from 11:52 A.M. (solar noon) until the late afternoon (4:02 P.M.). During the measurement, the  $I_{sc}$  of the cell was measured from which the irradiance was estimated.

The signal, noise and the corresponding SNRs obtained from 100 image-pairs for different incident light intensity are shown in Figure 4.13(a) and (b). The SNR as a function of numbers of image-pairs for different incident light intensity is presented in Figure 4.13(c). The signal and noise increase for increasing light intensity. Overall the noise has a linear relationship with the increasing light intensity, as this camera is dominated by both the readout noise and the shot noise.

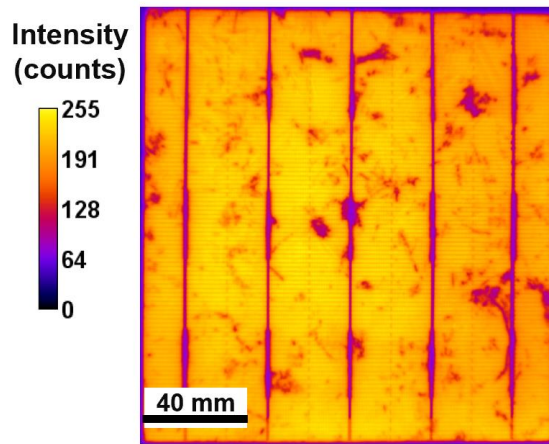


**Figure 4.12** PL image of the multi-Si PERC solar cell.

The corresponding SNR, thus, changes linearly with the incident light intensity. From Figure 4.13(c), it is observed that at noon, four image-pairs (320 ms measurement time) are needed for IEC's minimum SNR requirement of 15, whereas at 4 P.M., 15 image-pairs (1200 ms measurement time) are required if the same exposure time is used. In the experimental data shown in Figure 4.13, the exposure time is fixed, and therefore multiple image-pairs are needed to achieve a similar SNR. However, since the used camera is dominated by the readout noise, it will be beneficial to minimize the number of image-pairs and increase the exposure time such that the maximum sensor capacity is used without saturating the sensor, as discussed in Section 4.2. Moreover, since the dark noise of the used camera is low (Section 4.2), the total noise will remain unaffected by dark noise, irrespective of changes in the exposure time. The same SNR can be achieved at 4 P.M. by increasing the exposure time to reach the same PL signal that was captured at noon. Because the measurement time is far less than 1 sec overall, changing the exposure time is not a limitation for outdoor PL imaging.

Therefore, reaching a specific SNR is associated with reaching a minimum PL signal with the minimum number of image-pairs as possible (to minimize readout noise), which takes longer when the sun is less intense. For an ideal cell, the PL signal scales linearly with illumination intensity, unlike a shunted cell or cell with an ideality factor greater than one.

#### 4 Batch measurement of outdoor photoluminescence imaging

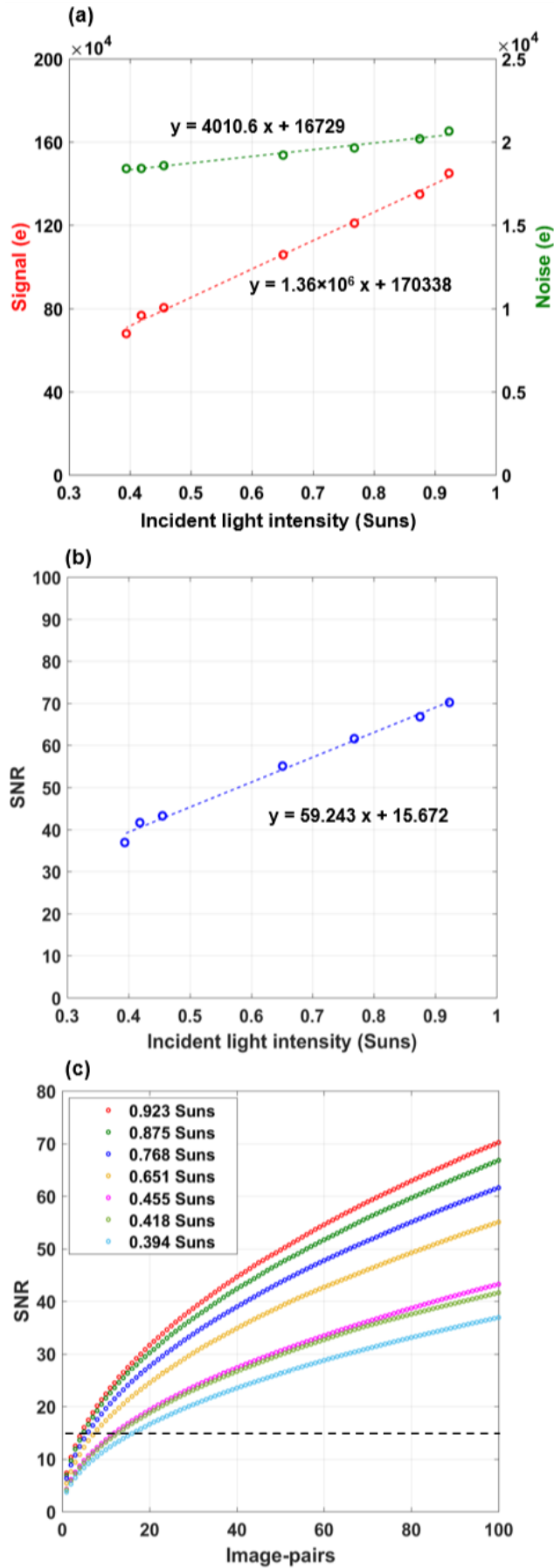


**Figure 4.13** (a) Signal and noise, and (b) SNR for 100 image-pairs and (c) the SNR computed for different incident light intensities across one day (March 25<sup>th</sup>, Sydney).

#### 4.5.2 Impact of cell open-circuit voltage

To quantitatively investigate the impact of cell  $V_{oc}$  on the image quality, mini module consisting of nine cast-mono silicon solar cells, connected in series is used.

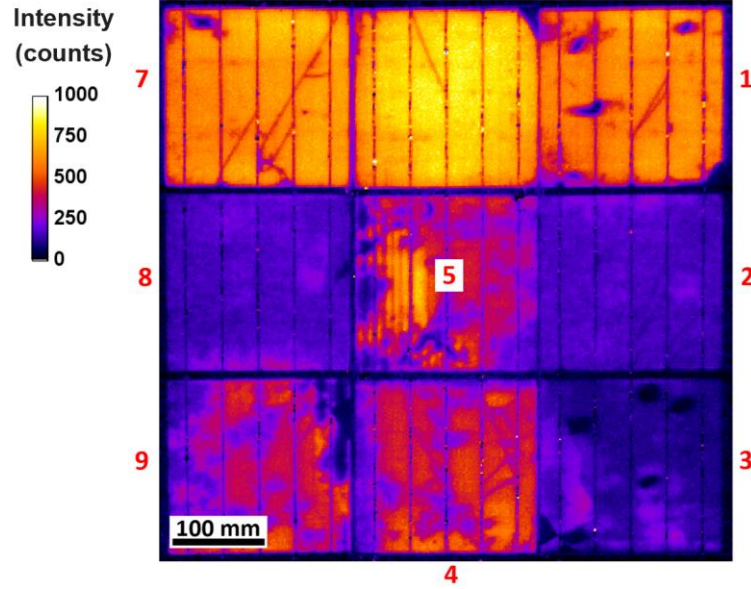


**Figure 4.14** Outdoor PL image of a cast-mono nine-cell mini module for 100 image-pairs (cell IDs are provided in red).

Table 4.2: Cell and module parameters

| Cell ID       | $V_{oc}$     | $I_{sc}$    | $R_{sh}$           | FF           |              |
|---------------|--------------|-------------|--------------------|--------------|--------------|
|               | [mV]         | [A]         | [k $\text{cm}^2$ ] | [%]          | [%]          |
| 1             | 666          | 9.05        | 0.33               | 65.51        | 16.41        |
| 2             | 633          | 8.94        | 1.11               | 70.96        | 15.94        |
| 3             | 624          | 8.75        | 0.21               | 63.63        | 13.54        |
| 4             | 651          | 9.04        | 1.61               | 69.97        | 16.46        |
| 5             | 648          | 8.83        | 4.24               | 57.58        | 13.11        |
| 6             | 673          | 9.16        | 4.48               | 72.60        | 17.76        |
| 7             | 667          | 9.31        | 0.96               | 71.44        | 17.82        |
| 8             | 633          | 8.92        | 3.62               | 70.87        | 15.97        |
| 9             | 646          | 8.98        | 1.89               | 67.28        | 15.55        |
| <b>Module</b> | <b>5,810</b> | <b>8.73</b> | <b>4.71</b>        | <b>68.69</b> | <b>15.99</b> |

The module was purposely fabricated with cells having significantly different  $I$ - $V$  characteristics ( $V_{oc}$  in the range 624 mV to 673 mV) to have a high module non-uniformity. Furthermore, shunts with different levels of severity were induced in

Cells 1, 3 and 7 by scratching the rear of the cells with a diamond pen. The module was built to enable access to the terminals of each individual cell. This allows light  $I$ - $V$  measurements of individual cells. These light  $I$ - $V$  measurements (of each cell) were performed after encapsulation using a SPIRE module flash tester [172]. The electrical parameters of the individual cells are summarised in Table 4.2. Note that some of the cells' parameters  $V_{oc}$ ,  $I_{sc}$  and FF does not result in the listed efficiency. This could be because of the impact of  $R_s$  in the cells. An outdoor PL image of the module obtained at approximately one Sun illumination, obtained from 100 image-pairs is shown in Figure 4.14.

The variation of signal, noise and SNR for 100 image-pairs and SNRs for increasing image-pairs between different cells is presented in Figure 4.15. As the cell  $V_{oc}$  increases, the PL signal is increased as a result of the exponential relationship between the PL signal and the cell's voltage (Equation 2.1). However, the noise is observed to be constant for different cells. This is because the measurement conditions including the camera, location and time are the same for different cells, therefore, contributing to the same read and shot noises. Although the PL signal contributes to the shot noise and is significantly changing for different cells, the total noise is not impacted by the PL signal as it only contributes 1.7-7% of the overall signal for this module as shown in Figure 4.16. Hence, the SNR is simply given by  $\frac{PL\ signal}{constant}$ . It linearly scales with the PL signal, the higher the PL signal, the higher is the SNR. The PL component  $\left(\frac{S_{t\_OFF}-S_{t\_ON}}{S_{t\_ON}} \times 100\right)$  at mid-day is plotted in Figure 4.16 as a function of the cell  $V_{oc}$  using a semi-log plot, confirming the exponential relationship between PL and  $V_{oc}$  and between PL and the SNR in the investigated case. Note that the deviation in the data from the linear fit in Figure 4.16 is expected to be because of the difference in ideality factors across the different cells.

Any increase in cell  $V_{oc}$  by  $kT$  causes the SNR to increase by a factor 2.71 (Equation 2.1). From the experimental value of  $kT = 30.67$  mV, the cell temperature during the experiment can be estimated to be 78.2 °C. This value is slightly higher than the expected temperature (~50 °C) for a solar module exposed to sunlight. This difference may be attributed to the deviation of the diode from a unity ideality factor.

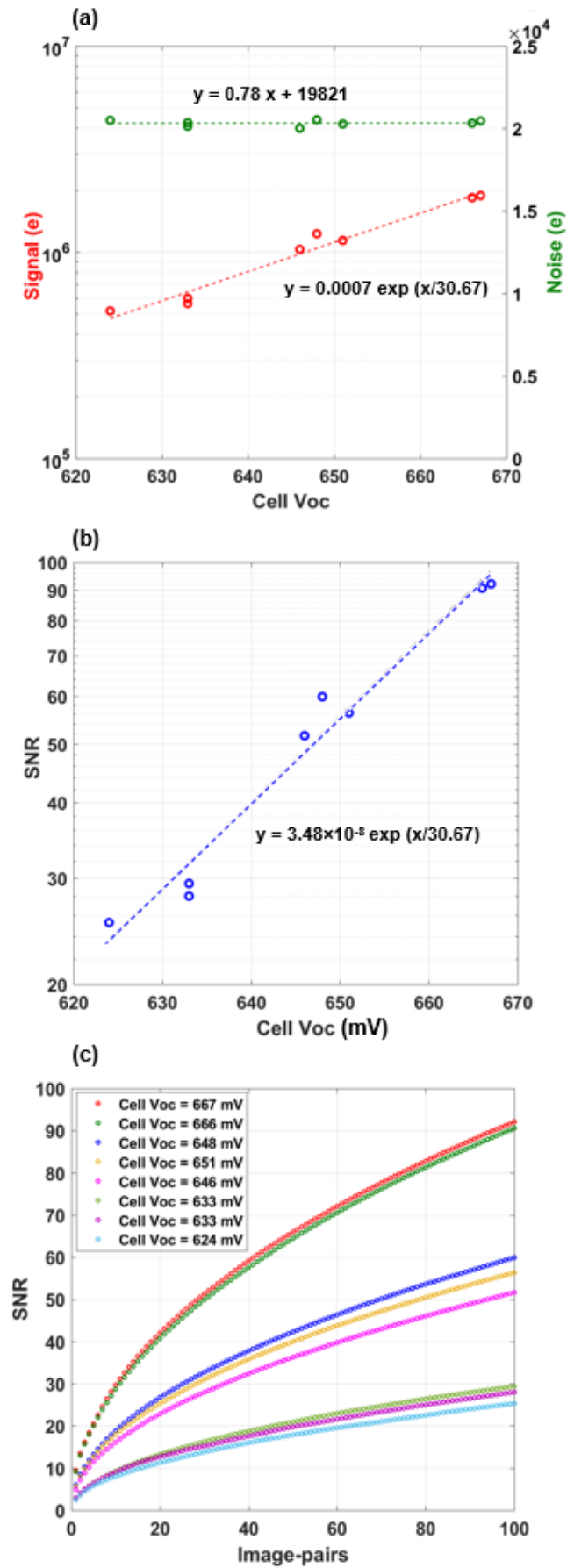


**Figure 4.15** (a) Signal and noise, and (b) SNR for 100 image-pairs and (c) the corresponding SNR computed for different cell's  $V_{oc}$  (February, Sydney).

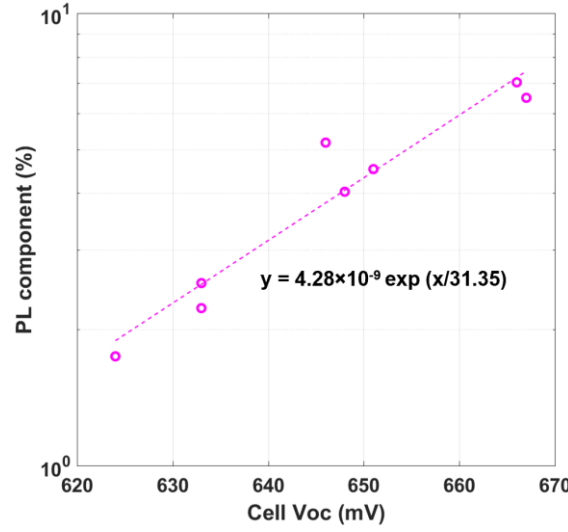


**Figure 4.16** PL component of signal as a function of cell  $V_{oc}$ .

In essence, the SNR varies exponentially with cell  $V_{oc}$  as it is dominated by the signal, while the noise remains almost constant. As mentioned in Chapter 3, future cell technologies will have significantly higher  $V_{oc}$  and therefore will achieve higher SNR for a lower number of image-pairs. For example, from Figure 4.15, the SNR obtained for a cell with  $V_{oc} = 667$  mV using one image pair (80 ms acquisition time) is 9.45 which is below the acceptable minimum SNR for outdoor luminescence imaging. However, if the cell  $V_{oc}$  increases to 688 mV (21 mV increase), just one image pair will be sufficient to achieve an SNR greater than the minimum acceptable of 15, as the resultant SNR would then already have doubled to 18.9. For achieving the minimum SNR of 15 suggested by the IEC standard [79], the minimum cell  $V_{oc}$  required for the technique to be successful is found to be 610 mV using the relationship between cell  $V_{oc}$  and SNR given in from Figure 4.15(b). Note that in practice imaging modules with different cell technologies might be influenced by the optical effects (such as a difference in cell texturing, anti-reflection coating and glass).

### 4.5.3 Control cell shunt resistance

The proposed outdoor PL imaging method relies on the test cells forced into OC condition when the control cell is shaded, as the shaded cells, in an ideal case, cannot carry any current. The non-shaded cells connected in series to the shaded cells build up a reverse voltage bias across the shaded cell that is equivalent to the sum of the  $V_{oc}$  of these cells (in practice up to  $\sim 15$  V). The current through the sub-string is limited by the reverse current of the shaded cell since industrial solar cells that are incorporated into modules are screened, generally during the final testing, to not exceed certain current limits.



The reverse current of the control cell at the reverse voltage that is built up by the series connected non-shaded cells flows through all test cells. As a result, the other cells will not go into OC condition, but to some intermediate operating point near  $V_{oc}$  (quasi OC condition), thereby reducing the PL signal. With a decrease in  $R_{sh}$  (increase in shunt conductance), we expect an increase in the reverse current through the shaded cell. Hence, a linear reduction in the PL signal and the SNR is expected. This section discusses the impact of  $R_{sh}$  of the control cell on SNR using the same nine-cell mini module from above section.

The current measured from the string terminals is presented in Figure 4.17. As expected, it shows a linear relationship between module current and shunt conductance.

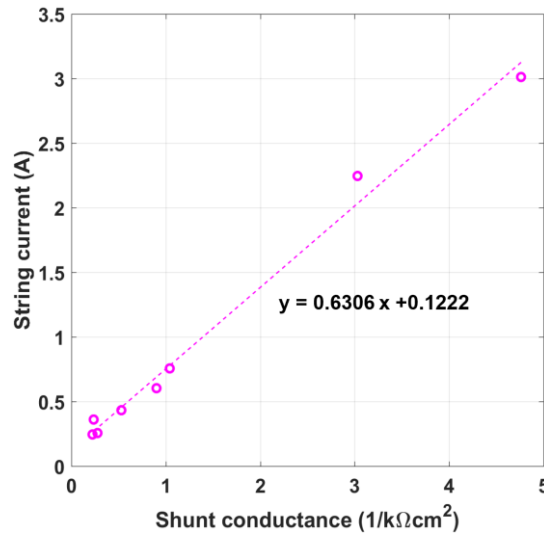


**Figure 4.17** Module current when the control cell is fully shaded as a function of the shunt conductance of the control cell.

The variation of signal, noise and SNRs of Cell 5 by controlling cells with different shunt conductance [determined from light I-V measurements (Table 4.2)] is presented in Figure 4.18. Similar to Figure 4.15, the noise is constant, while the signal and SNR are lower for control cells with low  $R_{sh}$  (high conductance value). Increased reverse current, that associated with lower  $R_{sh}$ , prevents the test cells to reach OC condition.

The module PL images obtained from five image-pairs by modulating the shading on four different control cells with different  $R_{sh}$  are presented in Figure 4.19 with the associated SNR of Cell 5 displayed above each image. Note the decreased PL intensity

#### 4 Batch measurement of outdoor photoluminescence imaging

from the whole module while modulating heavily shunted cells [Figure 4.19 (c) and (d)]. It is observed that the minimum acceptable SNR of 15 [79] is already achieved for five image-pairs when Cell 6 (high  $R_{sh}$ ) is modulated.

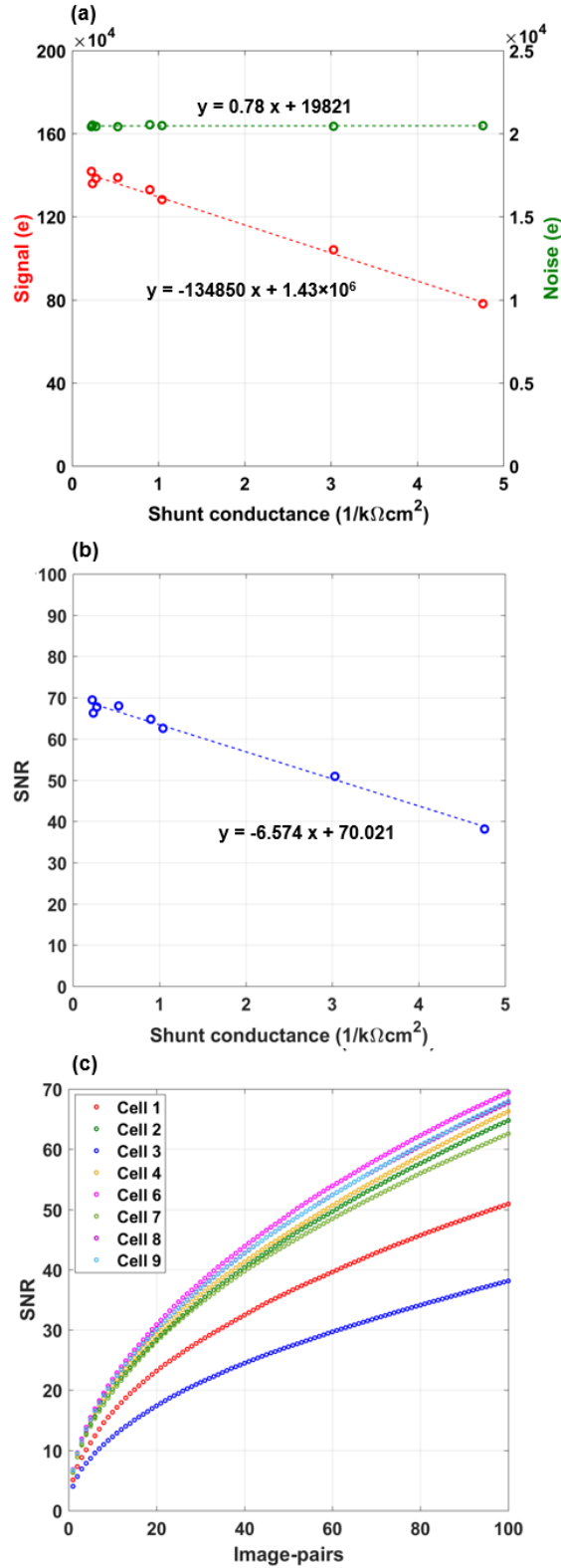


**Figure 4.18** (a) Signal, noise and (b) SNR for 100 outdoor PL image-pairs and the (c) SNR computed as a function of different image-pairs of different shunt conductance of the control cell (February, Sydney).

To minimize the possibility of measuring a reduced PL signal and the risk of hotspot (if the breakdown voltage of that cell is low) caused by selecting a shunted control cell for modulation, it is advisable to select more than one control cell in the sub-string. This divides the voltage of the illuminated cells between all shaded cells, i.e. by half if two cells are shaded, which reduces the current in proportion to the number of shaded cells for a linear shunt, but can have a much more dramatic effect (10× or 100× reduction in reverse current) for non-linear shunts and reverse breakdown (i.e. current can be large at -15V, but close to zero for -7.5V). These issues will be discussed further in Chapter 5 Section 5.5.3.

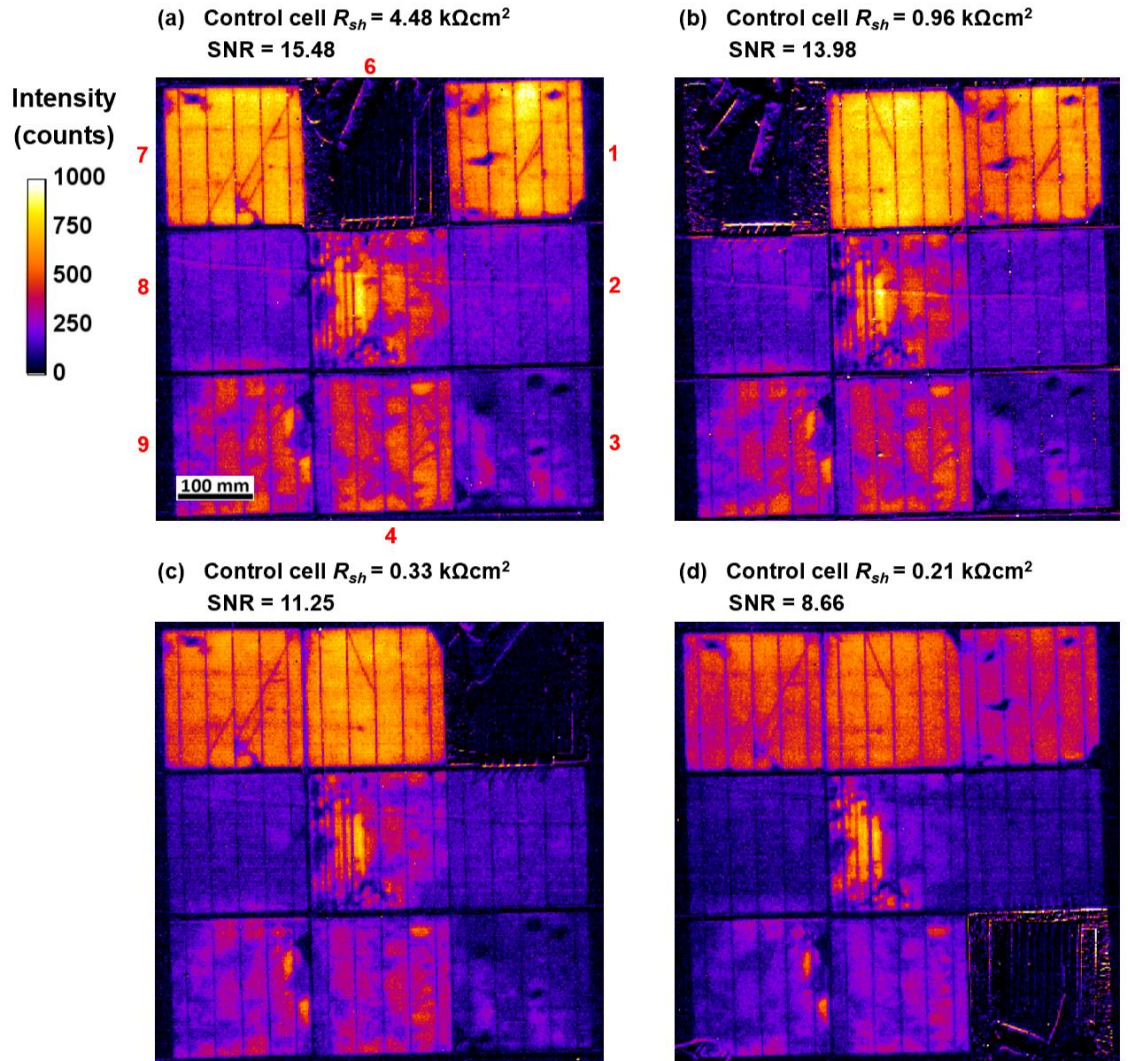


**Figure 4.19** Outdoor PL image for five image-pairs while selecting different control cells namely (a) Cell 6, (b) Cell 7, (c) Cell 1 and (d) Cell 3. The SNR of Cell 5 and the control cell  $R_{sh}$  are included at the top of the image while the cell IDs are provided in red in (a). Note that the control cell in the images appear dark as they were shaded.

## 4.6 Comparison between outdoor PL and conventional EL imaging

In this section, the outdoor PL imaging method developed in this thesis is compared with the more conventional outdoor EL imaging method.

Outdoor PL imaging is performed under one Sun illumination using the system described in Section 3.3, whereby the test cells are switched between MPP (approx.  $0.95 \times I_{sc}$ ) and OC during the measurements.

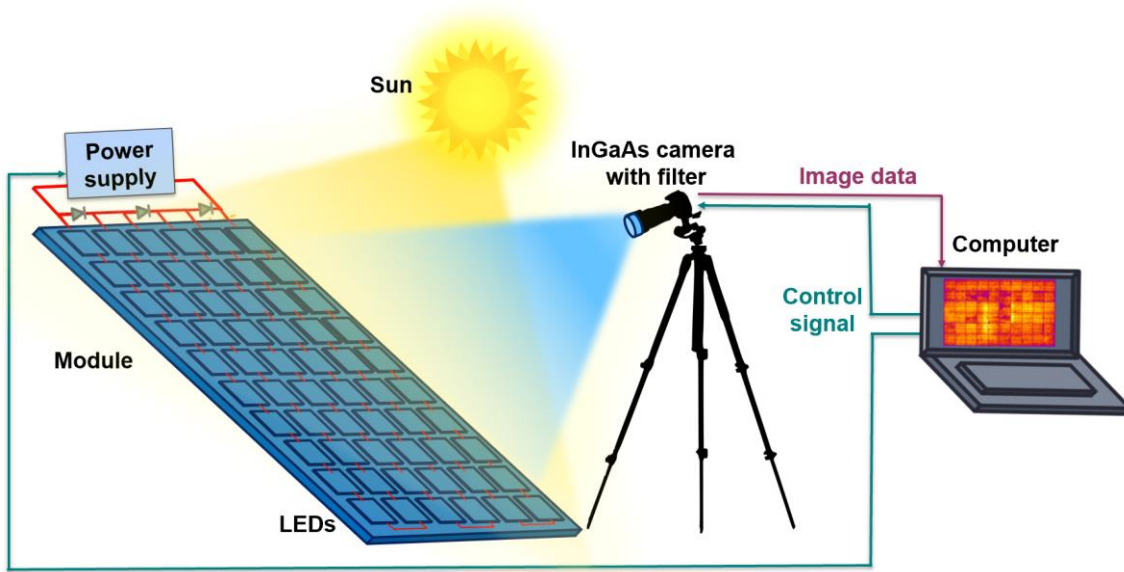


**Figure 4.20** Schematic diagram of the experimental outdoor EL setup.

Outdoor EL images are obtained under approximate one Sun illumination by connecting a power supply [173] across the module terminals as shown in Figure 4.20.

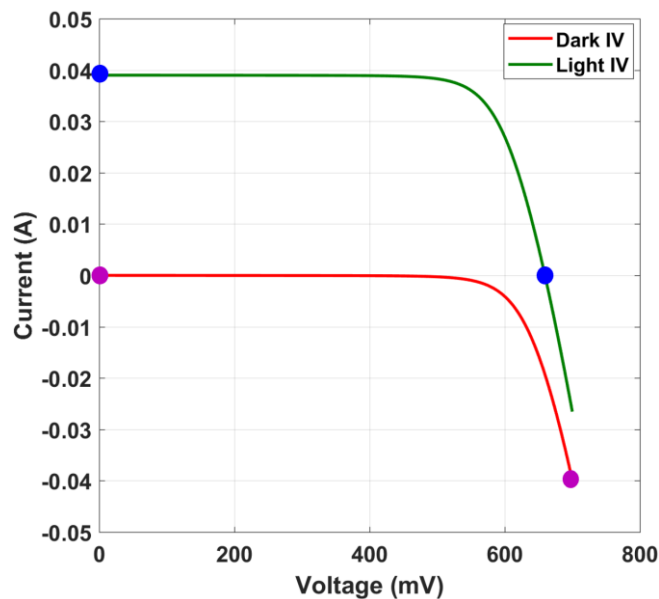


**Figure 4.21** Operating points of the image-pair for EL (purple dots) and outdoor PL (blue dots) imaging.

Table 4.3: Modelled solar cell parameters

| Cell parameter | Value                          |
|----------------|--------------------------------|
| $J_L$          | 39 mA/cm <sup>2</sup>          |
| $J_{0,1}$      | 300 fA/cm <sup>2</sup>         |
| $J_{0,2}$      | 10 nA/cm <sup>2</sup>          |
| $R_{sh}$       | 10 k $\Omega$ ·cm <sup>2</sup> |
| $R_{s,cell}$   | 1 $\Omega$ ·cm <sup>2</sup>    |

During the measurement, the injected current is switched between 0 and  $I_{sc}$ , modulating the overall module operating conditions between OC and  $I_{sc}$ . Note that in outdoor EL the current is injected instead of extraction as in outdoor PL, although the carriers contributing to the luminescence are the same. The two operating points used for both EL and outdoor PL are presented in Figure 4.21 using simulated dark and light  $IV$  curves of a solar cell. The simulated solar cell parameters are summarised in Table 4.3.

Indoor EL measurements are performed in the dark using the setup shown in Figure 4.20, without the bandpass filter (1125-1150 nm) since the ambient room light (LED light) is very low in the spectral sensitivity range of the InGaAs camera. During this measurement, the power supply is switched between 0 A and  $I_{sc}$ , similar to the outdoor EL measurements.

The three different measurements are compared capturing 1 to 100 image-pairs. The signal, noise and SNR analysis performed as a function of the number of image-pairs is shown in Figure 4.22. Note that all the measurements are performed using the same image acquisition parameters (exposure time, gain, aperture and camera temperature). It is observed that the signal and noise computed for indoor EL measurement is  $\sim 9$  times higher and 10% lower than the signal and noise of the outdoor measurements, respectively. This is mainly because, in outdoor measurements the bandpass filter restricts the PL detection to a narrow wavelength range, hence, only a small portion of the emitted PL signal is captured leading to an increased SNR. The  $\sim 5\%$  signal difference between the outdoor measurements (EL and PL) can be explained by the small difference between the current injected during outdoor EL ( $I_{sc}$ ) and the current extracted during outdoor PL ( $I_{MPP}$ ) contributing to a  $0.953 \times I_{sc}$  for this module. This difference in carriers contributing to luminescence emission affects the SNR.

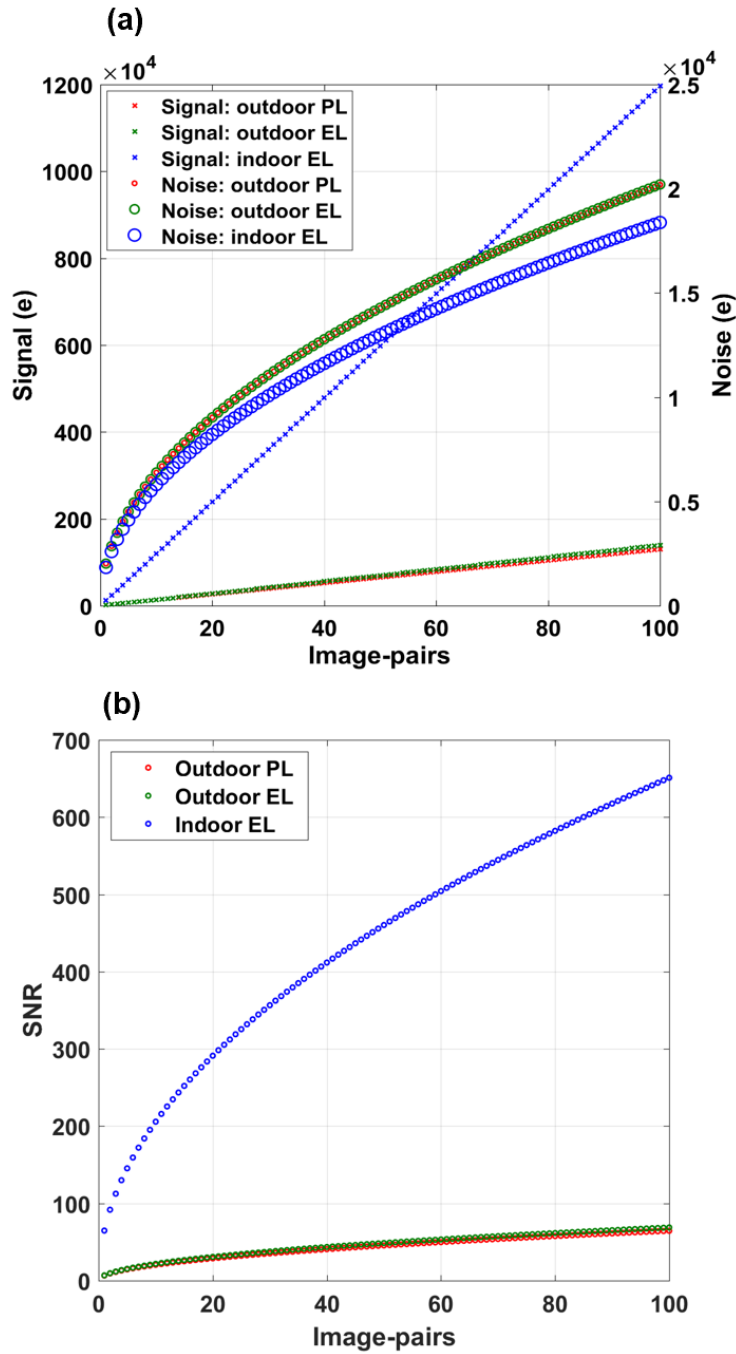


**Figure 4.22** (a) Signal and noise, and (b) SNR of indoor EL, outdoor EL and outdoor PL images.

Luminescence images obtained using one and 25 image-pairs, respectively, with their corresponding SNRs are presented in Figure 4.23. Although the SNR largely improves between one and 25 image-pairs for the indoor EL measurement, no significant difference in terms of image quality can be observed in the corresponding images. This is attributed to the high signal and very low noise present, even for a low number of image-pairs. For the outdoor EL and PL images, a reduction in the noise for 25 image-pairs is noticeable. Note that the outdoor PL and EL are not identical even though the SNR is almost identical.



This is because in the case of outdoor EL as the carriers are generated by injecting a constant forward current through the terminals, the current flows from the busbars, through the fingers, and into the semiconductor and isolated areas. However, in the case of outdoor PL, it is a difference between two images where one image is measured with a minimal current flow (OC image) and the other image with current extraction, i.e. with current flow in the opposite direction of that of EL. These effects will be discussed in more detail in the following section.

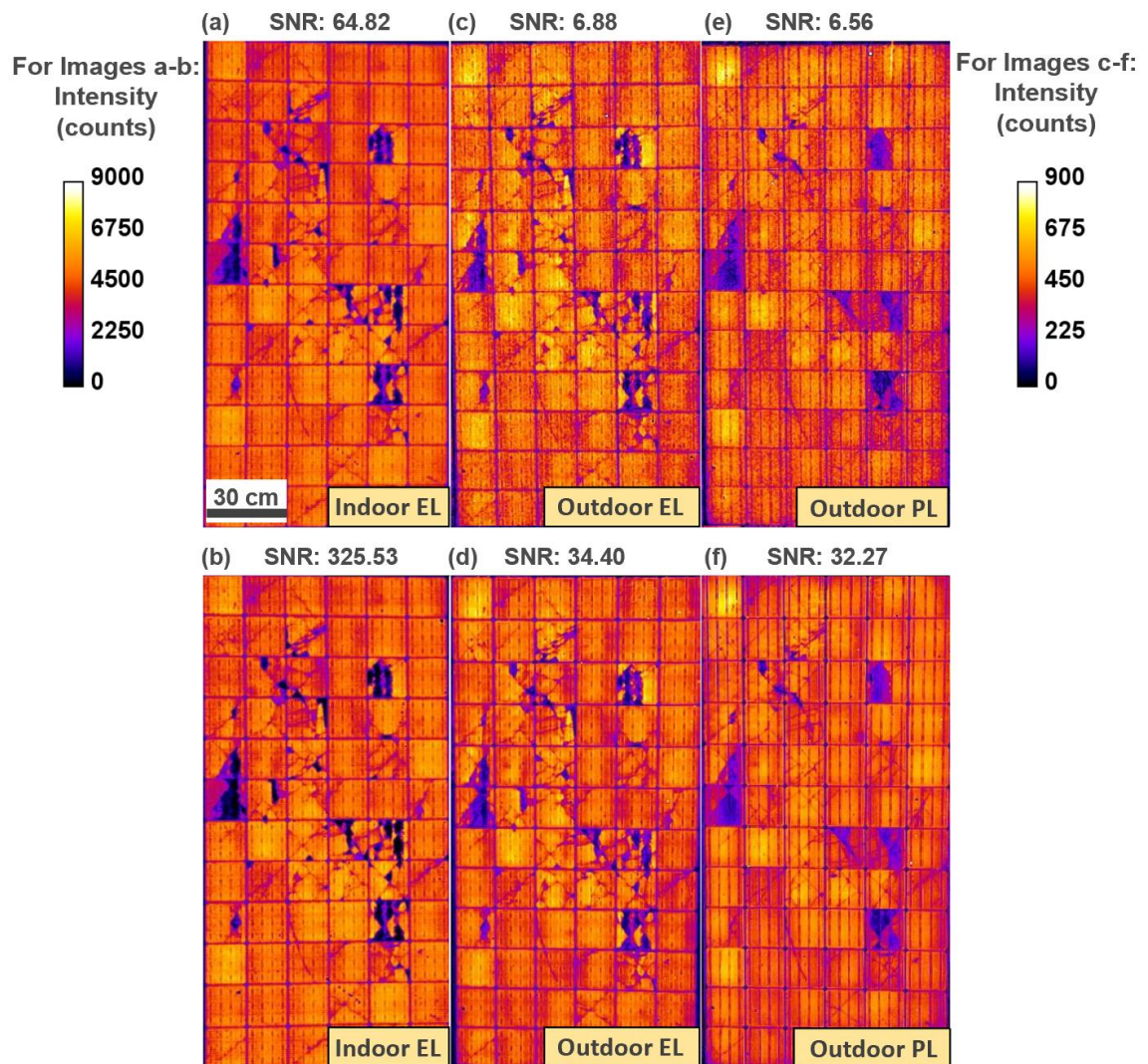


**Figure 4.23** Luminescence images: (a-b) indoor EL, (c-d) outdoor EL and (e-f) outdoor PL. The images on the top and bottom rows are obtained from one and 25 image-pairs, respectively.

## 4.7 Local series resistance quantification

Cracks that resistively isolate a segment of a cell, partially (Mode B [80]) or completely (Mode C [80]), contribute to the power loss of a PV system and can potentially lead to damaging hot-spot effects [174], as discussed in Chapter 2. Even comparatively

small fully isolated regions, of the total cell area, can have an impact on the module power output, as the sub-string current is limited by the damaged cell [67] and the bypass diode turns on. In this section, a method to quantify the extent of isolation, based on outdoor PL images taken at different operating points, is presented.

The method is first demonstrated using Griddler [175], a finite-element software that uses a network of electrical components to model a Si solar cell. Two isolated regions (Regions 1 and 2) are modelled in an otherwise uniform Al-BSF solar cell, as shown in Figure 4.25. The same cell parameters of Table 4.3 are used in this simulation. To achieve different degrees of resistive isolation, finger breaks of different lengths are inserted where the Regions 1 and 2 are simulated with  $2 \Omega\text{cm}^2$  and  $4.8 \Omega\text{cm}^2$ , respectively. The spatial distribution of  $R_s$  as simulated with this solar cell model is shown in Figure 4.24.

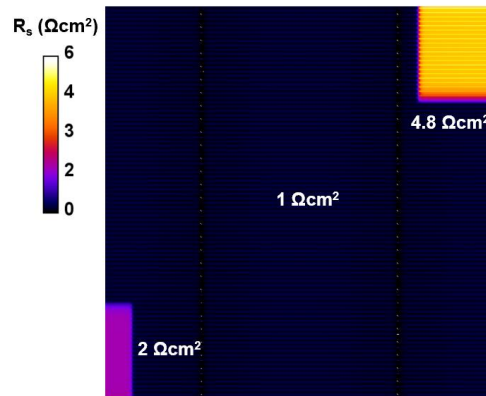


**Figure 4.24**  $R_s$  map of a solar cell with local variations in series resistance that was simulated in Griddler.

The simulated OC PL image with AM 1.5 spectrum and  $1000 \text{ W/m}^2$  of irradiance is shown in Figure 4.25(a). Note that all images in Figure 4.25 are displayed using the same PL intensity colour scale. The local voltage (and thus, the PL signal) in both isolated regions is slightly higher compared to the rest of the solar cell. One may expect that series resistance variations within a solar cell should not impact the PL image under uniform illumination and in OC condition. However, this is not the case when the resistively isolated regions feature less overall recombination. In the presented example, both Regions 1 and 2 are resistively separated from the recombination under the busbars, resulting in a slightly higher voltage and PL signal at  $V_{oc}$  [176].



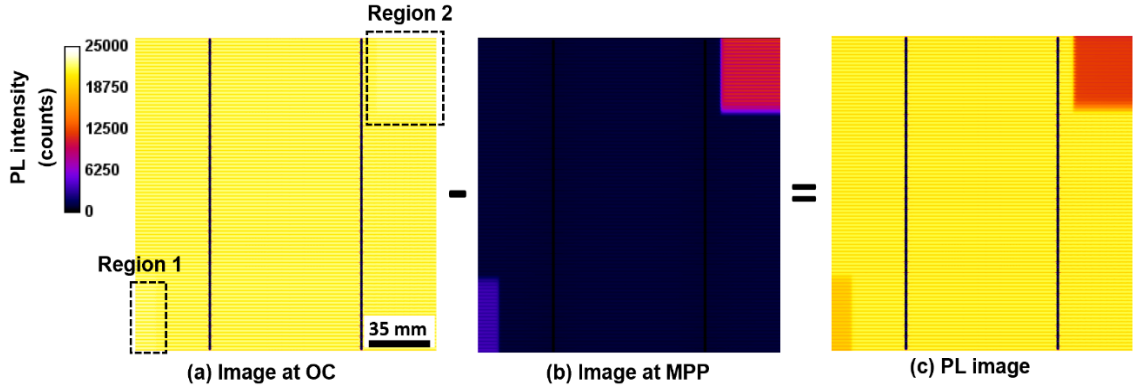


**Figure 4.25** Simulated luminescence images of a test cell containing two isolated regions under one-Sun illumination in (a) OC condition and (b) MPP condition and the corresponding (c) outdoor PL image obtained by subtracting (b) from (a). Note: The scale bar on the left applies to all images.

The simulated image for the cell operating at MPP condition is shown in Figure 4.25(b). The intensity in the isolated regions remains much higher compared to the remainder of the cell, while the intensity across the other regions of the cell decreased strongly, due to the extraction of approximately 95% of the photocurrent [112]. It is also noted that the intensity in Region 1 is lower than the intensity in Region 2, a result of higher current extraction from Region 1 and an indication that this region features lower series resistance.

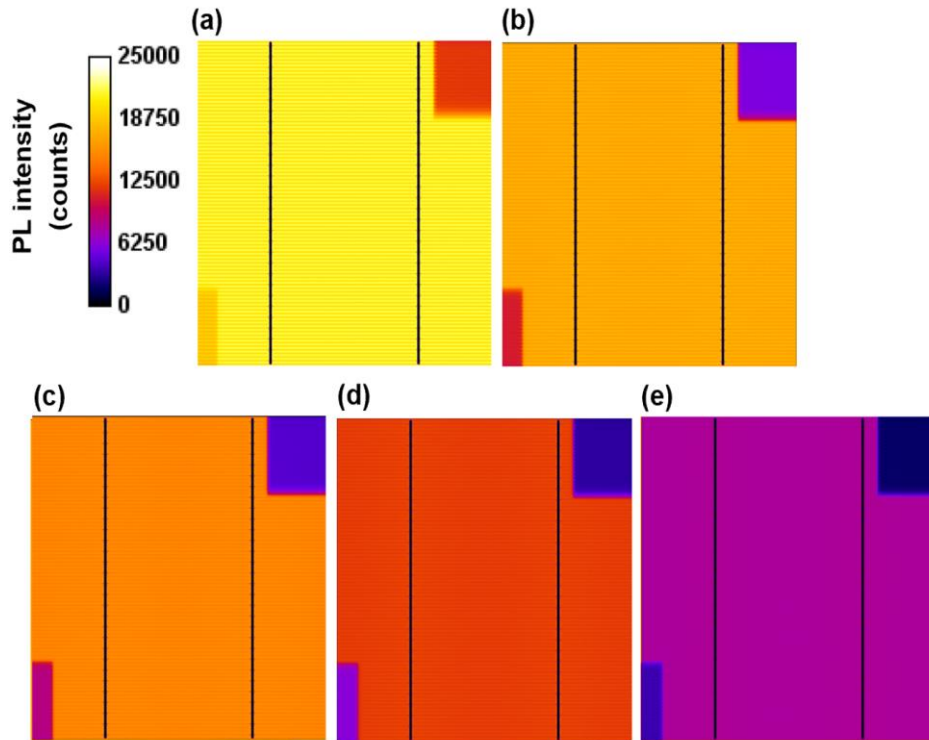


**Figure 4.26** Simulated outdoor PL images obtained between OC condition and a second operating point at a different current extraction condition of: (a) 0.93 Suns (b) 0.73 Suns (c) 0.64 Suns (d) 0.50 Suns and (e) 0.33 Suns.

The outdoor PL image, as it would be generated using a fully shaded *control cell*, is shown in Figure 4.25(c). Region 2 appears darker than Region 1 since it produces a higher PL signal due to lower current extraction in the MPP condition. This simulation demonstrates that  $R_s$  variations in the cell have a significant impact on the outdoor PL image. The same effect on image-pairs taken at different OPs will be further investigated below. Simulated outdoor PL images obtained using different cell OPs are presented in Figure 4.26(a-e). Note that all images are displayed using the same colour scale. In all cases, the first image is simulated under OC condition i.e. with zero current extraction (full shading of the *control cell* in practice). The operating point of the second image is varied by controlling the current extraction conditions. Note that Figure 4.26(a), in which variation between MPP and OC is simulated, is identical to Figure 4.25(c). As the second operating point shifts towards OC (reducing the illumination on the *control cell* in practice), the overall difference in PL intensity and thus, the resulting measured PL signal, reduces.

To illustrate the PL intensity change over a large change in extracted current density, in Figure 4.28 the PL intensity of the normal cell area, as well as that of Regions 1 and 2, as a function of the current extraction level is presented. Notably, for different current extraction conditions, the PL intensity of Region 1 changes faster compared to that of Region 2. This indicates that Region 2 is more resistively isolated than Region 1. This feature will be exploited below to quantify the degree of isolation [129].

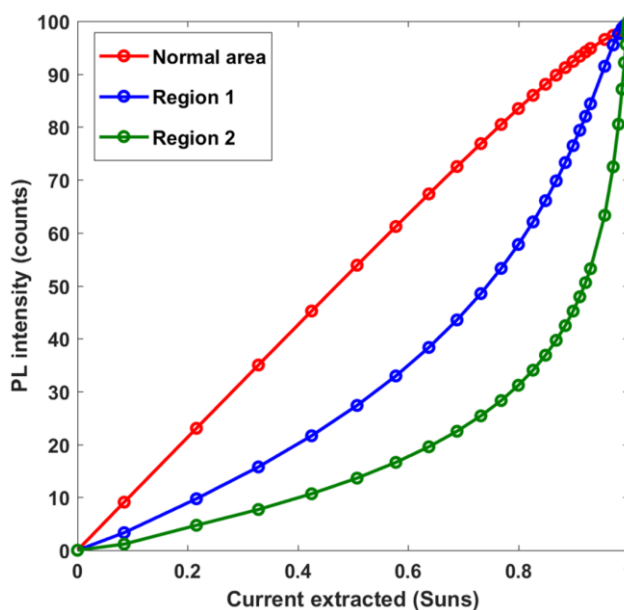


**Figure 4.27** Change in the PL intensity as a function of different current extraction conditions (a) in Region 1 and Region 2 corresponding to the Griddler simulations shown in Figure 4.26.

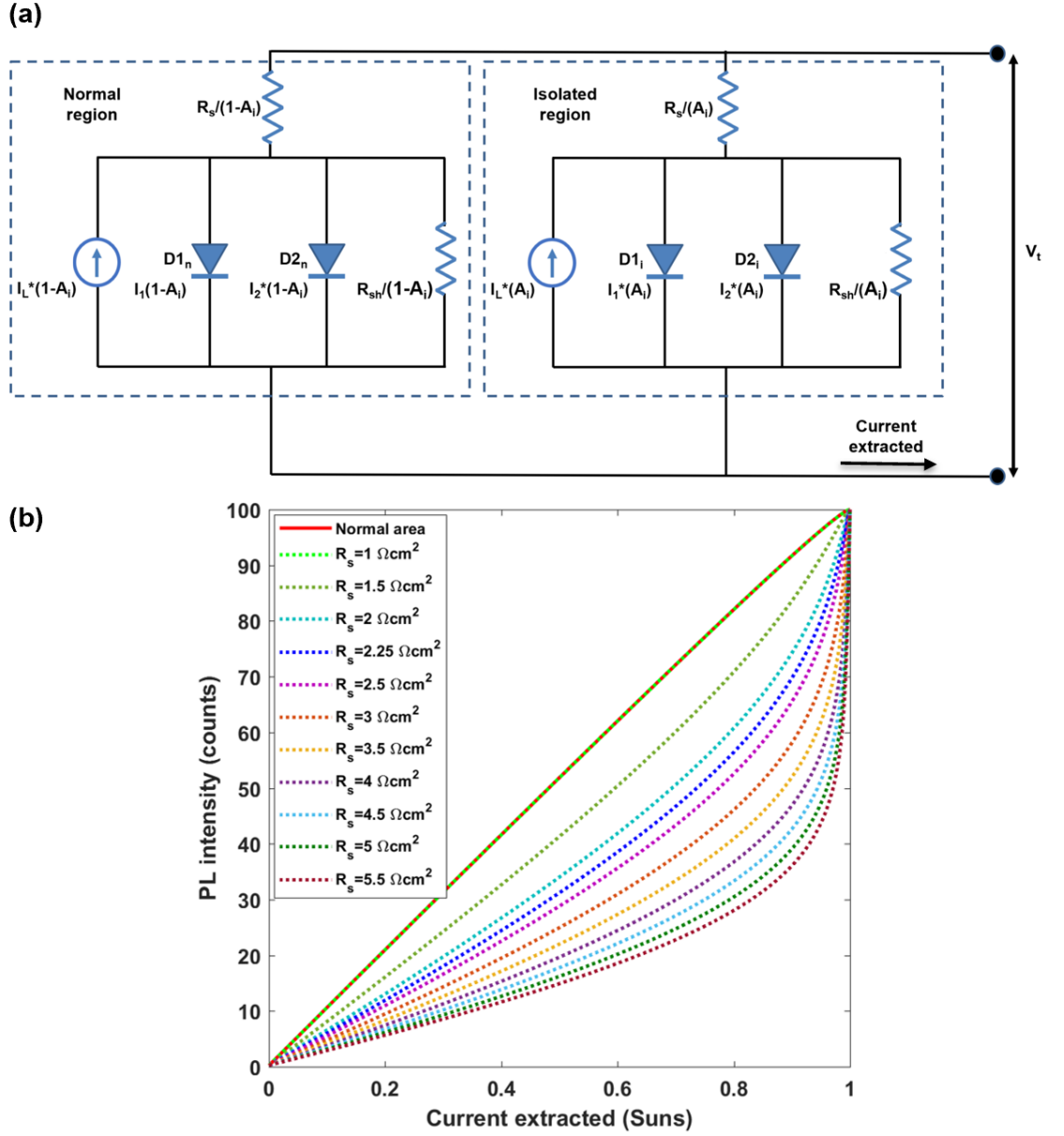


**Figure 4.28** (a) LTspice equivalent circuit model of a solar cell with a single isolated region and (b) Change in the PL intensity as a function of different current extraction conditions for a solar cell with one resistively isolated region as a function of  $R_s$  of the isolated region modelled with LT-Spice.

In order to quantify this effect, the cell is modelled using LT-Spice [162]. The standard two-diode model is used to represent the main body of the solar cell ( $R_s$  unaffected, normal region) connected in parallel with another two-diode model representing a resistively isolated area. The equivalent circuit diagram of this model is shown in Figure 4.28(a). The same cell parameters of Table 4.3 are used in this simulation as well. In the model, the factor  $A_i$  represents the fraction of the area of the isolated region relative to the overall cell area. Using this model, considering  $A_i = 0.045$  (area of Region 2 with respect to rest of the cell), the change in the PL intensity of the normal and enhanced  $R_s$  region is

simulated for various current extraction conditions and different  $R_s$  values of the isolated region as shown in Figure 4.28(b). From a comparison between the change in the PL intensity obtained from the Griddler simulation [Figure 4.28] and the LT-Spice simulation [Figure 4.28(b)],  $R_s$  of the isolated areas is determined to be  $2.25 \Omega\text{cm}^2$  (Region 1) and  $5 \Omega\text{cm}^2$  (Region 2), both agreeing very well (in the range 12%) with the value simulated in Griddler (Figure 4.24). Typically since the isolated areas are sufficiently small with respect to the total cell area, a model with a single isolated region (Figure 4.27) can be applied to each of the regions separately without making a notable error.

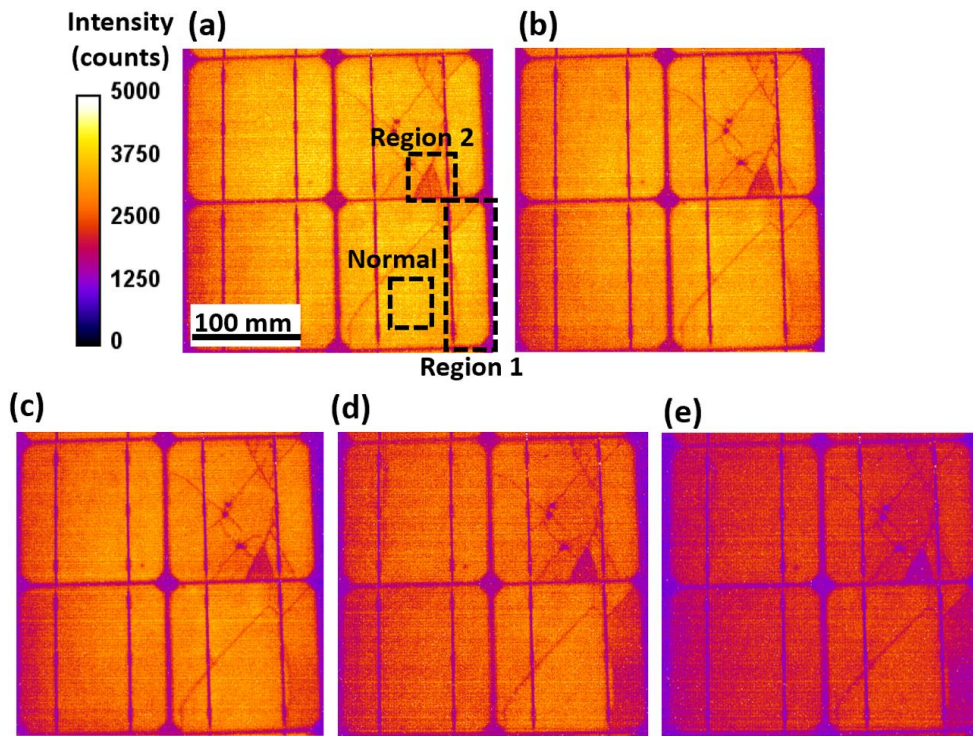


**Figure 4.29** Outdoor PL images obtained between OC condition and a second OP at a different current extraction condition: (a) 0.93 Suns (b) 0.73 Suns (c) 0.64 Suns (d) 0.50 Suns and (e) 0.33 Suns.

In order to demonstrate this application, a PV module (72 cells, mono-Si, Al-BSF) with different types of isolated areas (marked as Region 1 and Region 2) was measured outdoors. Luminescence images of a 2x2 cell section of that module are shown in Figure 4.29. In order to determine the light generated current that is equivalent to  $I_{MPP,system}$ , the LED intensity needs to be increased until there is no notable change in the outdoor PL image. Using this value, all other current values can be determined through the linear relationship between the LED light intensity and light-induced current density. The PL intensity change as a function of the extracted current is plotted in Figure 4.30. It shows that as the second bias point is shifted towards  $V_{oc}$  (*control cell* illumination towards zero),

that Region 1 shows a stronger PL intensity change than Region 2. Based on the previous discussion, it can be concluded that Region 1 exhibits lower resistive isolation. Note that as the average  $R_s$  of the remainder of the cell ( $R_{s,cell}$ ) is unknown, only the relative change of  $R_s$  can be determined. Using the LT-Spice model from above, the change in the PL intensity of the two isolated areas is found to be 1.5 (Region 1) and two times (Region 2) of  $R_{s,cell}$ , thus demonstrating the capability of the presented approach to estimate the degree of isolation.

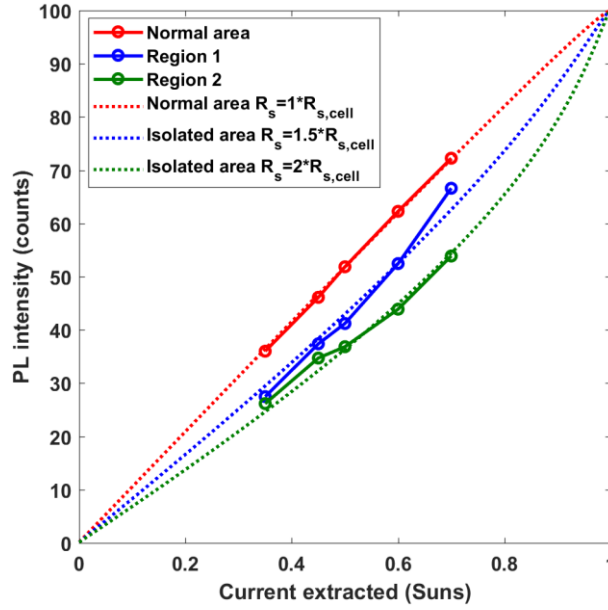


**Figure 4.30** PL intensity as a function of extracted current in the normal area and Regions 1 and 2 for the module shown in Figure 4.29 (circles and solid line). Also displayed are the corresponding LTSpice model results using  $R_s$  values that result in an optimal fit to the measured PL intensity curves (dotted lines).

## 4.8 Solar car imaging

This section presents an application of the developed method to characterize the UNSW solar race car, named *Violet* [177]. The solar array of this car is based on high efficiency Maxeon Gen III solar cells [178] without reflectors or concentrators. The cell's  $V_{oc}$  is about 720 mV. The maximum allowable collector area for this car as per design constraints is 5 m<sup>2</sup>.

For obtaining outdoor PL images of *Violet*, an image-pair is obtained by modulating the cells between OC and SC using the outdoor PL setup described in Section 3.3. For simplicity, instead of using the shading approach, the array terminals (after disconnecting from the battery) are directly switched between OC and SC.



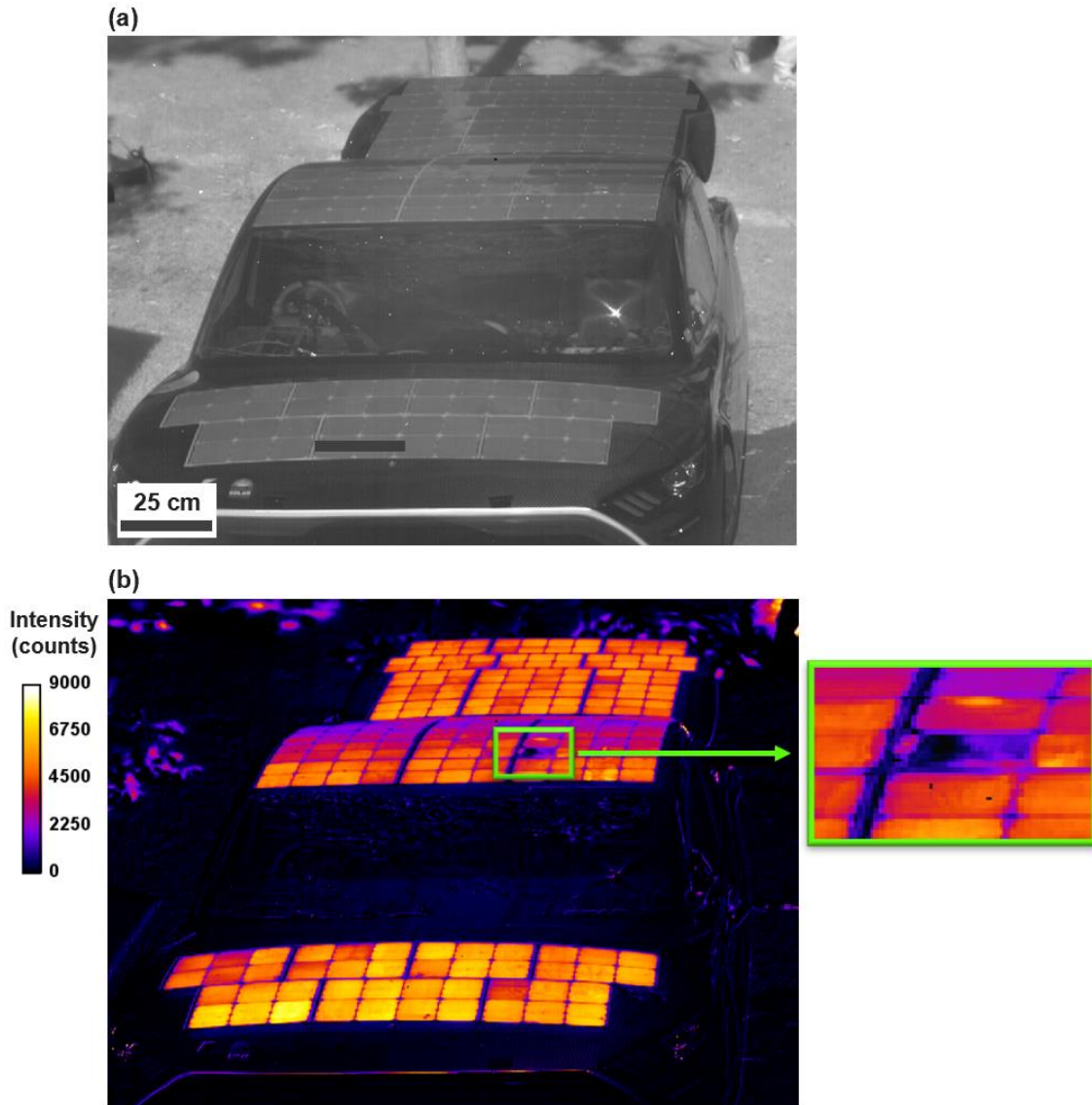


**Figure 4.31** (a) Image captured by the outdoor PL system in OC condition and (b) the outdoor PL image obtained from a single image-pair.

The image captured by the system in OC condition is shown in Figure 4.31(a) and the obtained outdoor PL image is shown in Figure 4.31(b), using only **one image-pair**. The high-quality of the PL image is quite impressive, especially considering the minimal measurement time (80 ms) and the non-ideal angle at which the image was taken. This is a clear demonstration of the ease of using the method to image future solar modules which will feature solar cells with much higher cell  $V_{oc}$  than are common today. One of the solar cells is observed to be degraded with lower PL emission as highlighted by the close-up inset. Note that the non-uniformity in the PL intensity across the image between the hood, roof and the boot of the car is due to optical effects and not because of the difference in PL emission (the camera was mounted in a shallow angle due to the limitation of the maximum height of the tripod). The PL image of the roof was collected at the shallowest

angle and looks darker because of the Lambertian emission of the PL [33]. Hence, ideally, a system for imaging vehicle integrated PV should be mounted directly above the vehicle that is investigated.

## 4.9 Application in Solar farms

The *sequential* measurement using a prototype system was applied to a 5 MW fixed-tilt solar farm (Summerhill solar farm, Australia) consisting of 345 W mono-Si PERC modules with cell  $V_{oc}$  of 656 mV. A row of six LED's (optical modulator) shading two cells in each sub-string (6 cells in total) is used to modulate the operating conditions of the module between MPP and OC. The shading of two control cells in each sub-string of the module has the previously mentioned advantage of enabling measurements with lower current flow through the test cells and less sensitivity of the images on the reverse characteristics of the control cell. Measurements were performed using an industrial prototype measurement system, which was developed at UNSW and which incorporates the measurement approach developed and first demonstrated as part of this thesis.

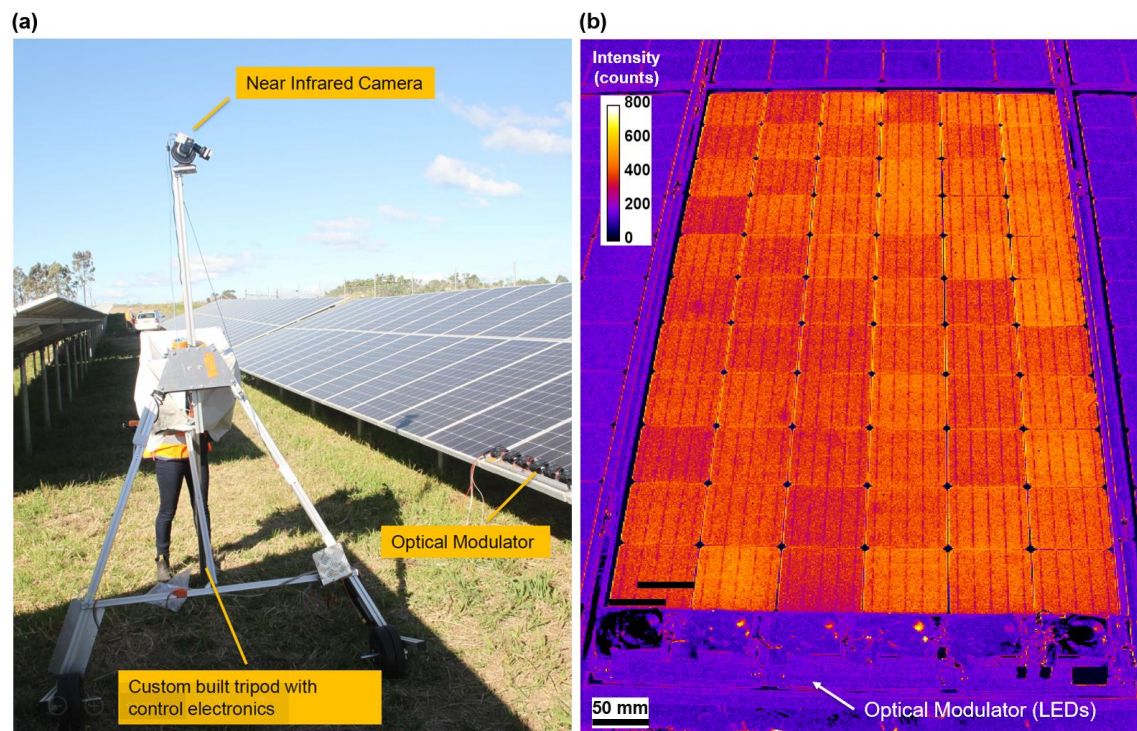


**Figure 4.32** (a) The first prototype of the outdoor PL imaging system and (b) the resultant outdoor PL image obtained from 100 image-pairs.

A PL image obtained from 100 image-pairs of one of the modules is shown in Figure 4.32. Note that the neighboring modules appear dark in the image as they are not modulated and still operating at MPP condition. The optical modulator is covering the

bottom row of cells, as discussed above, and thus, in order to get a PL image of the full module, a second image would need to be measured, with another row of cells acting as control cells. No performance limiting defects can be observed in this particular image, however, the image exhibits substantial intensity variations between cells. PL images obtained from other random modules installed in this solar farm confirmed the high quality of the modules. Using the prototype an average throughout of one module per minute was achieved, a demonstration of the capability of the outdoor PL imaging system to inspect large solar farms.

### 4.10 Chapter summary

This Chapter proposed a simplified *offset corrected batch* measurement that is simple and robust to sunlight changes and overcomes the PL modulation problem of the *sequential* method presented in Chapter 3.

Detailed noise analysis was performed for the existing camera [158] which was used for all measurements presented in this thesis. The technique is currently limited by the excessive readout noise of this camera which is dominant for signal strength of  $\sim 300,000$  e and the source of 50% of the noise when the full 16-bit of the camera is used (i.e. 2,004,090 e). Using a camera with similar sensitivity but say 10 times lower readout noise is therefore the key to improve the technique and to allow better SNR with a lower number of image-pairs. Since the readout noise dominates, the total number of reads (image-pairs) must be minimised and therefore it is beneficial to maximise the signal in each image by increasing the exposure time without saturating the sensor. Modern cameras have substantially better noise performance especially in terms of readout noise [159] and therefore some of the conclusions from this chapter would be significantly different for those. In this sense the calculation presented in this thesis are worst-case scenario and the ability to reach the desired SNR will be better for modern cameras. The application will be further facilitated by cell voltages of modern industrial PERC solar cells exceeding 680mV.

This chapter also demonstrated that the same SNR can be achieved by adapting the exposure time at any time of the day as dark noise is insignificant. The SNR was observed to be higher for the outdoor PL images for higher cell  $V_{oc}$  modules (since PL has an exponential relationship with voltage as shown in Equation 2.1) and control cells having higher  $R_{sh}$  (due to low reverse current in the sub-string). The relationship between each



of these parameters and SNR was established enabling the prediction of SNR for a specific module, location and time of measurement. The image quality of outdoor PL images was compared to outdoor and indoor EL images. This chapter also demonstrated a method to extract spatial series resistance information in a module that can be used to differentiate and quantify resistance-related degradation in fielded modules.

The outdoor system was used to investigate the state and quality of solar arrays of a solar race car. Finally, a commercial prototype for an outdoor PL imaging system, based on the methodology first demonstrated within this thesis, was available at the end of this thesis to investigate field-deployed solar modules in an operating large scale solar farm.



## Chapter 5

# Implied current-voltage measurements of individual cells in a module<sup>3</sup>

The performance of individual solar cells in solar modules influences the reliability, lifetime, cost, and safety of photovoltaic power plants. The electrical performance of these cells, as well as their degradation rates over time, can vary significantly between individual cells within the same photovoltaic module. Current-voltage measurements can provide detailed data on cell performance. However, as discussed in Chapter 2, they cannot be performed on individual cells in encapsulated modules.

In this chapter, a contactless and non-destructive method that is based on Suns-photoluminescence measurements to extract the current-voltage characteristics of individual solar cells under operating conditions in the field is presented. Applications of the method to identify the extent of various degradation mechanisms, such as light-induced and potential-induced degradation, are demonstrated and discussed. The main advantages of the proposed method include its low cost, and its fast and easy applicability.

---

<sup>3</sup> This Chapter is partially based on:

**Bhoopathy, R.,** Kunz, O., Dumbrell, R., Trupke, T. and Hameiri, Z., 2018. Contactless extraction of implied I-V curves of individual solar cells in fully assembled modules using photoluminescence. In *7th World Conference on Photovoltaic Energy Conversion* (pp. 3578-3602).

**Bhoopathy, R.,** Kunz, O., Dumbrell, R., Trupke, T. and Hameiri, Z., 2019. Application of suns-photoluminescence to extract implied I-V curves of individual cells in modules installed in the field. In *36th European Photovoltaic Solar Energy Conference and Exhibition*.

**Bhoopathy, R.,** Kunz, O., Dumbrell, R., Trupke, T. and Hameiri, Z., 2019. Outdoor non-contact measurement of pseudo I-V curves of solar cells in a module. In *Asia Pacific Solar Research Conference*.

**Bhoopathy, R.,** Kunz, O., Dumbrell, R., Trupke, T. and Hameiri, Z., 2020. Outdoor implied current-voltage measurements of an individual encapsulated cell in a module. *IEEE Journal of Photovoltaics*. (Accepted for publication in the next issue)

### 5.1 Introduction

As discussed in Chapter 2, identifying the cause for the underperformance of individual cells can be critical for detecting the dominating source for power plant degradation. In many cases, early recognition of these fault mechanisms even allows recovery measures to be quickly implemented [54]. In other cases, the results of such studies can inform the solar industry and provide important guidance for future cell and module designs.

Removing solar modules from existing solar power plants for thorough characterization is impractical and cost prohibitive if a significant number of modules are to be tested. Additionally, it is challenging to extract the *individual* cell  $I$ - $V$  information when cells are embedded in finished solar modules using currently utilised characterization techniques. Trained experts, as well as sophisticated equipment and methods are often required, which limits or even prevents their use for routine inspection of fielded modules.

In this chapter, a highly sensitive, fast, simple, and cost-effective method to obtain implied  $I$ - $V$  curves from encapsulated cells in a module, without the requirement to access the module terminals is presented. The method presents a substantial improvement over other methods discussed in Chapter 2 and therefore has the potential to become a routine inspection method for researchers and solar plant operators.

### 5.2 Methodology

The Suns-PL method [35]–[37] is used in this Chapter to obtain implied  $I$ - $V$  characteristics of solar cells that are free of series resistance effects. During Suns-PL measurements, the tested solar cell is illuminated with light of varying intensity and the corresponding PL signal is measured simultaneously. Usually, the solar cell under test operates at OC conditions. Trupke *et al.* [24] demonstrated for the first time the excellent agreement between Suns-PL and Suns- $V_{oc}$  measurements.

The fundamental principle of Suns-PL is that the light-generated current in the cell is linearly dependent on the illumination intensity, while the cell's implied open-circuit voltage ( $iV_{oc}$ ) is logarithmically related to the measured PL signal ( $P_L$ ) as shown in Equation 2.1.

The key benefits of this method include:

- (1) The method is *contactless*, hence, avoiding the requirement to access individual cell or module terminals.
- (2) Highly sensitive implied voltage measurements in the operational voltage range (between maximum power point, MPP and OC) are achieved through PL, as the measured signal is exponentially related to  $iV_{oc}$ .
- (3) The measurement is *less sensitive* to temperature changes, which is beneficial for outdoor measurements [179].

### 5.3 Calibration procedure

Although Suns-PL measurements can be used without calibration to identify different loss and cell failure mechanisms, a few applications might be required to obtain calibrated absolute implied  $I$ - $V$  curves. The illumination intensity of the light source is calibrated to respective Suns by measuring the  $I_{sc}$  of a reference cell having a similar quantum efficiency to the cell being measured. The calibration of the implied voltage is achieved by determining the factor  $C$  (of Equation 2.1) which can be obtained using two different approaches.

#### 5.3.1 Suns-PL curves

The first approach is based on Suns-PL measurements of a statistically significant sample set in a string. In this method, the PL response of some of the cells in a string is measured (measured cells) using the setup described later in Section 5.4. The sample set is selected such that it is large enough to represent most of the cells in the string. The temperature corrected string OC voltage is given by:

$$V_{oc,string} = \left[ \sum_{i=1}^M V_T \ln \left( \frac{\phi_i}{C} \right) \right] + \left[ (N - M) V_T \ln \left( \frac{\bar{\phi}_{1-M}}{C} \right) \right] \quad (5.1)$$

where  $M$  is the number of measured cells in the string,  $N$  is the total number of cells in the string,  $\phi_i$  is the integrated PL intensity of the  $i^{th}$  cell measured at one Sun illumination and  $\bar{\phi}_{1-M}$  is the average PL intensity of all the measured cells (from 1 to  $M$ ) at the same illumination (one-Sun). In this equation, the first and second terms represent the sum of  $V_{oc}$  of measured and rest of the cells, respectively, from Equation 2.1.

Using Equation 5.2,  $C$  is calculated as [117], [118], [151]:

$$C = \sqrt[N]{\frac{(\bar{\phi}_{1-M})^{N-M}}{\exp(V_{oc,string}/V_T)}} \prod_{i=1}^M \phi_i \quad (5.2)$$

### 5.3.2 Luminescence imaging

Luminescence images, such as EL [117], [118], [151] or PL [22], [129] can also be used to determine  $C$  using Equation 5.2, where  $\phi_i$  is a pixel value representing the luminescence intensity of the  $i^{th}$  cell after flat-field correction. In this study,  $\phi_i$  is selected as the maximum pixel value of the  $i^{th}$  cell (after eliminating the top 0.1% intensity pixels, that could be measurement artefacts due to “hot pixels”, saturated pixels or faulty pixels [119]). To allow comparison between the two methods, one of the measured  $\phi_i$  is normalized using the one-Sun PL intensity from the Suns-PL measurement of the same cell. This is done to minimise the impacts the optical parameters have on the two methods (luminescence imaging and Suns-PL; each is impacted differently by these parameters). Note that any cell can be selected for this calibration procedure. Although using luminescence images is quicker compared to Suns-PL for calibrating Suns-PL curves, it is comparatively complicated and requires more sophisticated equipment. However, if the plant was already inspected with luminescence imaging, the images can then also be used for calibration. If EL images are used, the image should be obtained with a minimum influence of  $R_s$ , i.e. typically at low current injection ( $< 0.1 I_{sc}$ ) [117], [118], [151]. Note that EL, in contrast to PL, requires contacting the string or module terminals to inject current.

Using the temperature corrected module  $V_{oc}$  ( $V_{oc,mod}$ ) instead of  $V_{oc,string}$  (as presented in [117], [118], [151]) in the above two approaches might lead to a smaller number of cells needing to be measured, thus, making it less time consuming. However, measuring  $V_{oc,mod}$  is, in general, not practical for fielded modules as it requires disconnecting the modules from the string, a procedure which requires a qualified (and expensive) electrician. It is possible to estimate  $V_{oc,mod}$  by using the information provided in the data-sheet of the investigated module or by measuring  $V_{oc,mod}$  of an equivalent non-degraded module of the same type.

On the other hand,  $V_{oc,string}$  can be measured by the string inverter as many of them have the capability to measure at least a part of the  $I$ - $V$  curve of the string [180]. The additional advantage of this instead of  $V_{oc,mod}$  is that the  $C$  estimated for one of the strings



## 5 Implied current-voltage measurements of individual cells in a module

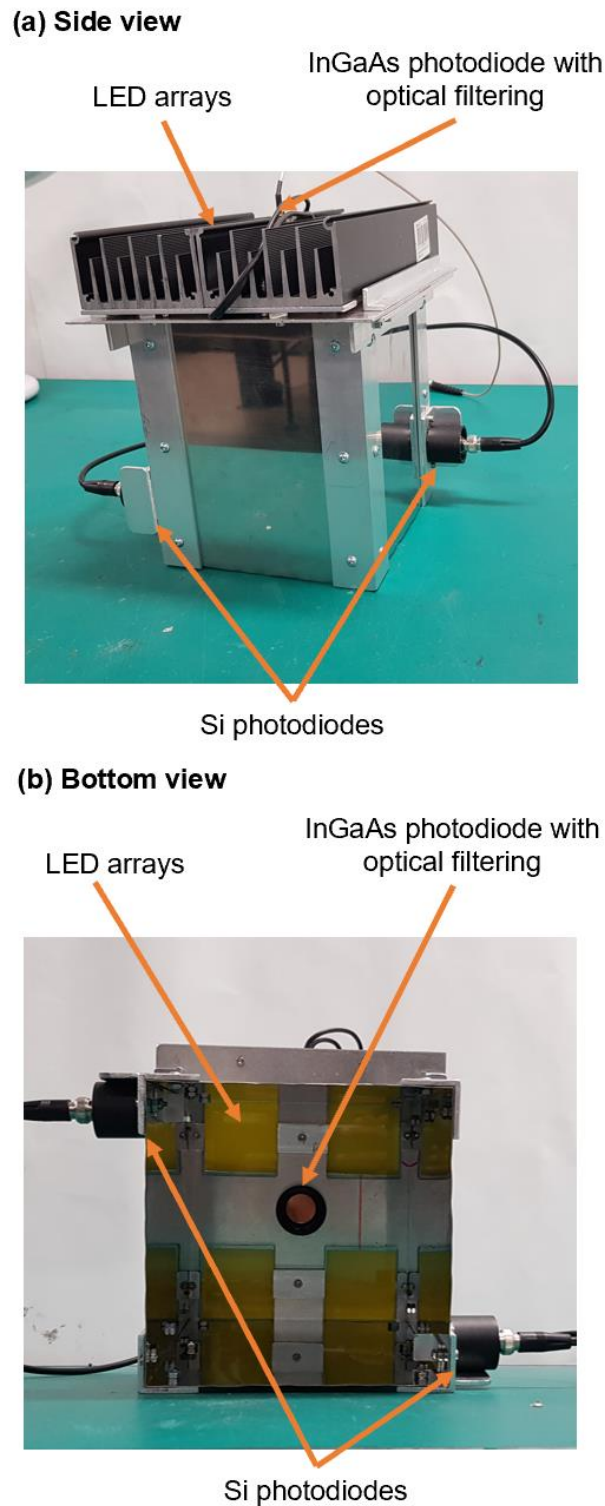


**Figure 5.2** Experimental setup of the Suns-PL tool.

In between the LED arrays, an InGaAs photodiode (5) is mounted, along with a suitable optical filter set (cut-on and cut-off wavelengths of 1100 nm and 1150 nm, respectively [21]) to measure the PL intensity with minimal impact of stray light in outdoor conditions. Note that the height of the Suns-PL tool (25 cm) is designed as a trade-off between the InGaAs photodiode capturing the PL signal from the entire tested



cell and receiving a sufficient amount of PL signal (that drops off proportional to the square of the distance). In this tool, the collection efficiency of the PL signal between the centre and edge of the cells differs by ~16% according to the cosine-fourth-power law that applies in such circumstances. The tool contains two Si photodiodes (6) that are mounted on its inner walls pointing upwards to ensure that they only measure the illuminating light and not the light reflected from the measured sample (Figure 5.1 indicates only the output connections of these photodiodes, not their actual locations, situated inside the tool). The measured photocurrents from the InGaAs and Si photodiodes are amplified using SR570 low noise transimpedance preamplifiers (7) [182]. The preamplifier signals are then captured by the data acquisition card (8); USB-1808 from Measurement Computing [183]) and transferred to the computer (9) for further processing (see Figure 5.1). A picture of the experimental setup of the Suns-PL tool (3) is shown in Figure 5.2.

## 5.5 Results and Discussion

This section presents the application of the Suns-PL method both indoors and outdoors to extract implied  $I$ - $V$  curves of individual cells in a module. It demonstrates the ability of the method to investigate some of the common degradation mechanisms in the field and discusses the challenges associated with the outdoor measurements.

The mini-module described in Sections 4.5.2 is used in this section. To validate the Suns-PL method the module was built to enable access to the terminals of each individual cell, which allows performing:

- Suns-PL measurements
- Suns- $V_{oc}$  measurements, and
- light  $I$ - $V$  measurements

of all individual cells within the mini-module. The electrical parameters of the individual cells performed using light  $I$ - $V$  measurements can be found in Table 4.2.

### 5.5.1 Comparison between calibration methods

Figure 5.3 presents the implied voltage calculated from different methods as detailed in Section 5.3 using Equation 5.2 while all cells in the mini-module ( $T=M=9$ ) were measured. Note that in the presented case,  $V_{mod}$  is identical to  $V_{string}$  as this module is not

## 5 Implied current-voltage measurements of individual cells in a module

connected to other modules. The voltages are measured using a SPIRE module flash tester [172] and are corrected to 26.85 °C. The inserted table presents the RMS standard deviation ( $\sigma$ ) of the difference of implied and terminal voltages, for all the cells for each method.

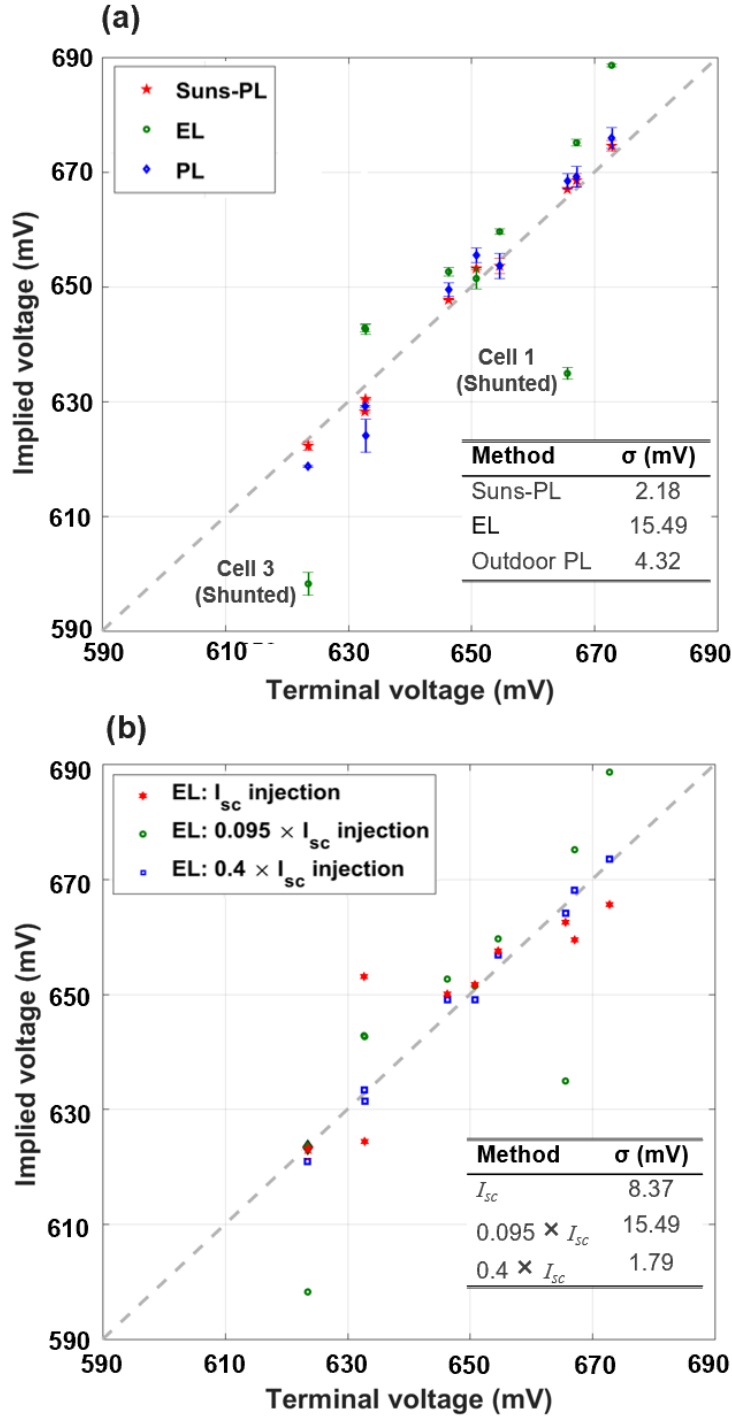


**Figure 5.3** Implied voltage as a function of terminal voltage using (a) different calibration methods discussed in Section 5.3, and (b) calibration based on EL images taken at different current injection levels. The dotted line represents  $y = x$ , while the standard deviation ( $\sigma$ ) between  $V_{ter}$ - $V_{imp}$  for each method is displayed in the inserted tables. Error bars in (a) are obtained from five repeat measurements.

The Suns-PL measurements are performed using the setup described in Section 5.4, while the EL and PL measurements are performed using the setups described Sections 4.5 and 3.3 respectively. The PL imaging is performed by modulating the module operating conditions between MPP and OC, while EL presented in Figure 5.3(a) is performed at a low injection of  $0.095 \times I_{sc}$ . The results indicate that a calibration based on Suns-PL data for all cells against  $V_{mod}$  provides the most accurate results when following the method based on outdoor PL. The slightly larger  $\sigma$  of the outdoor PL method is attributed to the small impact of  $R_s$  at MPP. The calculated voltage using EL images under low current injection of less than 10% of  $I_{sc}$  ( $0.095 I_{sc}$ ) as proposed in [117], [118], [151] is erroneous, especially in the case of heavily shunted cells (see Cells 1 and 3). This is because the low-injection measurements are subject to significant shunting and high ideality factor recombination. Hence, a tradeoff needs to be found between the benefits of low injection measurements to reduce the impact of  $R_s$  and the impact of shunt and non-ideal recombination at this injection range. Figure 5.3(b) presents a comparison between implied voltages calculated from EL images measured with forward current equivalent to  $I_{sc}$ ,  $0.4 \times I_{sc}$ , and  $0.095 \times I_{sc}$ . In this case, even the measurement with the highest current, with a significant impact of  $R_s$ , performs better than the low injection measurement. The mid-range current injection of  $0.4 \times I_{sc}$  provides the best results for this particular module with a very low  $\sigma$  of 1.62 mV from the terminal voltage.

Note that in the field, the accuracy of the methods will depend on the sample set measured for the estimation of  $C$ . The main advantage of Suns-PL based calibration is its simplicity, as it avoids the need for additional equipment. Therefore, in this chapter, Suns-PL measurements are used for calibration purposes whenever absolute implied voltages are calculated from luminescence measurements.

### 5.5.2 Indoor measurements

The proposed method is first demonstrated in the laboratory, as indoor measurements can be performed with a well-controlled low-level surrounding illumination. These measurements are used for comparison with outdoor measurements (Section 5.5.3). During the measurement, the illumination intensity incident on the measured cell is varied approximately sinusoidally with a frequency of 0.45 Hz, as shown in the inset in Figure 5.4. Such a slow frequency allows for low-noise quasi-steady-state measurements that minimise measurement artefacts that could be present, in particular when measuring high efficiency solar cells with long carrier lifetimes [184]–[186].

Figure 5.4 displays the PL signals of three cells with significantly different  $I$ - $V$  characteristics (Cells 1, 3 and 6 from the mini-module shown in Figure 4.14). Note that any fault affecting the implied  $I$ - $V$  curve, such as cell degradation, is reflected in the luminescence signal [115]. For an ideal cell, a linear relationship between illumination intensity (hence, the current) and emitted PL intensity (hence, the exponential of voltage) is expected. As these curves are fitted for high illumination intensities, it is expected they are mostly impacted by the diode with a unity ideality factor (in the absence of  $R_s$ ). Therefore, for this ideal case, the fit intercept is expected to be at the origin. For the non-ideal case, where the curve cannot be described by only one diode, the intercept is expected to shift from the origin. For instance, in the case of the best cell (Cell 6), the relationship between the emitted PL intensity and illumination intensity is linear throughout most of the measurement and thus, the distance of the intercept from the origin is small.

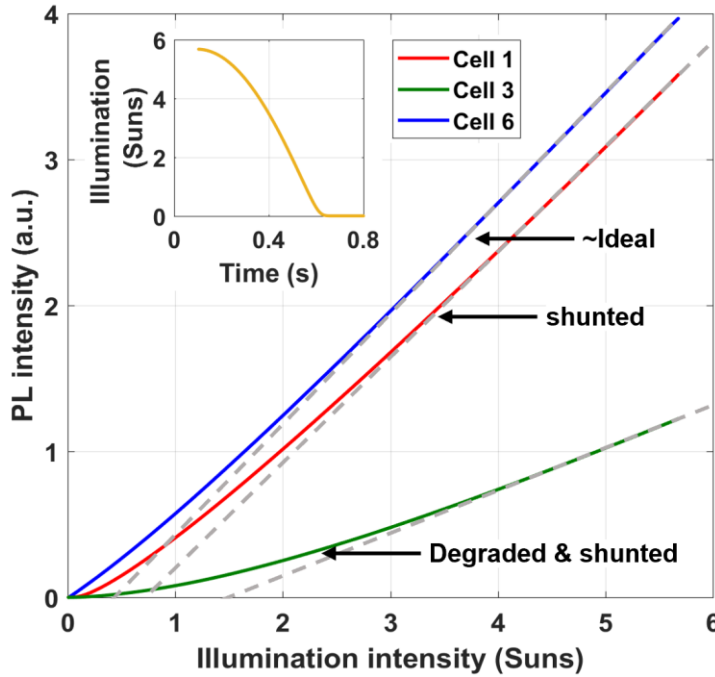


**Figure 5.4** Measured PL intensity of three selected cells from the mini-module as a function of illumination intensity. The inset shows the illumination intensity as a function of time. The dashed line represents the linear relationship that is observed at high illumination intensities.

For shunted cells, the linear relationship fails at illumination intensities  $< 0.5$  Suns with reduced PL signal throughout the measurement, although the slope remains similar (Cell 1 in comparison with Cell 6). This is a clear demonstration for the ability of the proposed method to detect shunts, such as those produced by PID [83]. Early detection of these shunts can be useful in order to recover the affected modules in the field [82], [83], [187].

Although Cell 1 and Cell 3 have similar  $R_{sh}$ , the slope of the PL intensity reduces significantly for Cell 3 as it is highly degraded. This highlights the ability of the proposed method to detect increased saturation currents in solar cells, for example cells that are affected by CID [188].

Figure 5.4, thus, highlights the ability of the Suns-PL method to detect different loss mechanisms and to distinguish between them, even *before* calibrating the measured PL intensity to an absolute implied voltage. It should be noted that in many cases it is not necessary to calibrate the Suns-PL measurements to absolute  $I$ - $V$  curves (via the determination of  $C$ ). For instance, if the purpose of the measurement is a *relative* comparison between cells or identification of fault mechanisms, then the uncalibrated Suns-PL data already provides sufficient information.

Using  $C$  values determined from Suns-PL measurements of all nine cells of the mini-module (as presented in Section 5.5.1), the Suns-PL measurements of the three cells are converted into implied  $I$ - $V$  curves and presented in Figure 5.5. As expected from the PL image (Figure 4.11) and the measured PL signal (Figure 5.4), the difference between the  $I$ - $V$  curves of the three cells is significant. To validate the method, Figure 5.5 also includes the measured Suns- $V_{oc}$  [189] curves of the same cells. Note that the Suns-PL data is denser at illumination intensity less than 1.5 Suns since each cell's Suns-PL curve is taken using two separate sweeps to increase the measurement range. The measured terminal voltages,  $V_{oc}$ , agree very well with the  $iV_{oc}$  determined by the Suns-PL method. The deviation between the corresponding curves observed above one-Sun intensity stems most likely from shading and contact recombination induced by the front metal grid, in combination with the lateral  $R_s$  of the cell, as previously reported [176]. This deviation is found to be 4.5-5 mV at one Sun for the cells tested here. A similar value was previously reported in [54]. Note that due to the rapid decrease of the PL signal with voltage, the Suns- $V_{oc}$  measurements extend into a lower voltage regime. However, the range covered using Suns-PL is fully adequate to obtain all the relevant solar cell parameters, as will be shown below. It is possible to translate the light intensity to current, if  $I_{sc}$  is known. However, it is challenging to measure  $I_{sc}$  of encapsulated cells. To minimize the associated uncertainty, in this study, we use the light intensity and not  $I_{sc}$ .

## 5 Implied current-voltage measurements of individual cells in a module

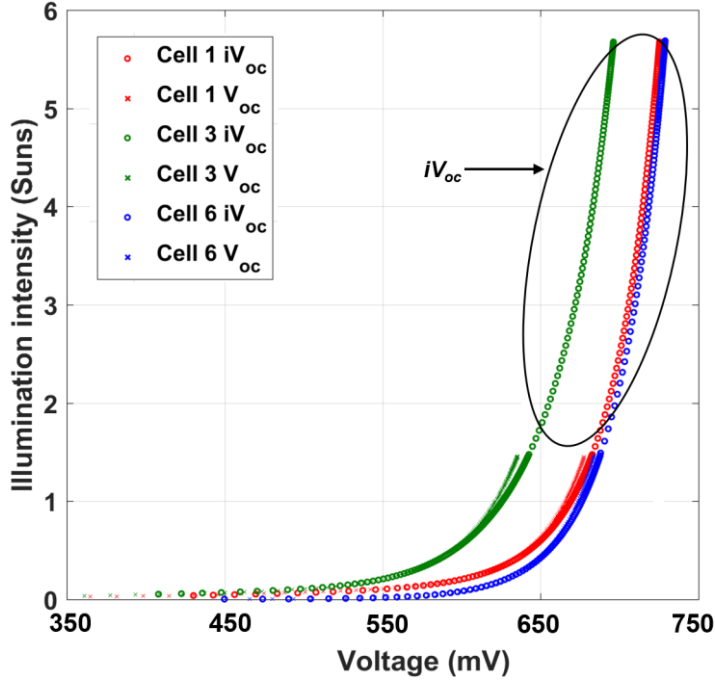


**Figure 5.5**  $I$ - $V$  curves obtained from Suns-PL ( $iV_{oc}$ ; open circles) and Suns- $V_{oc}$  ( $V_{oc}$ ; crosses) measurements.

The  $J$ - $V$  characteristics of a solar cell without the influence of  $R_s$  can be described by the two-diode model [33], [190]:

$$J = J_L - J_{01} \left( \exp \left( \frac{V}{m_1 V_T} \right) - 1 \right) - J_{02} \left( \exp \left( \frac{V}{m_2 V_T} \right) - 1 \right) - \frac{V}{R_s} \quad (5.3)$$

where  $J_L$  is the light generated current density,  $J_{01}$  ( $J_{02}$ ) are the saturation current densities of the diode with ideality factors  $m = 1$  ( $m = 2$ ), and  $V$  is the implied or terminal voltage. In many cases, extracting the two-diode model parameters allows identification of the dominant recombination mechanisms [33].

Table 5.1: Two diode model fit parameters (first four columns) and measured  $R_{sh}$  (last column)

| Cell ID | $J_{01}$<br>[pA/cm <sup>2</sup> ] | $J_{02}$<br>[nA/cm <sup>2</sup> ] | $pFF$<br>[%] | $R_{sh}$<br>[k cm <sup>2</sup> ] | Measured $R_{sh}$<br>[k cm <sup>2</sup> ] |
|---------|-----------------------------------|-----------------------------------|--------------|----------------------------------|---|
| 1       | 0.08                              | 36.22                             | 74.86        | 0.29                             | 0.33                                      |
| 3       | 0.19                              | 133.10                            | 72.89        | 0.46                             | 0.21                                      |
| 6       | 0.11                              | 16.12                             | 81.21        | infinity                         | 4.48                                      |

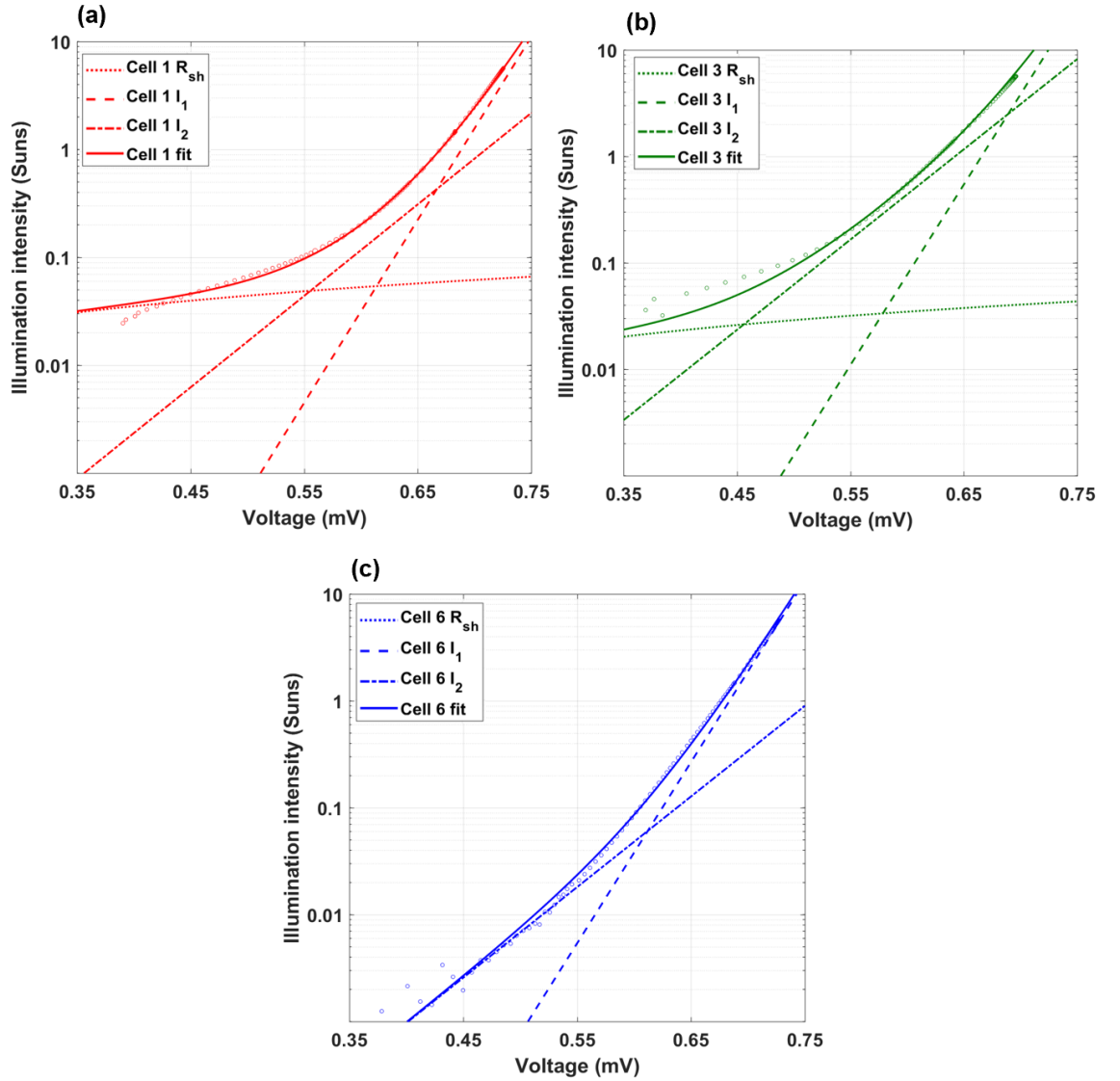


**Figure 5.6** Semi-log plot of the data in Figure 5.5 with a two-diode model fit for (a) Cell 1, (b) Cell 3 and Cell 6.

The two-diode model fits to the  $iV_{oc}$  data (using weighted least squares [191]) for selected cells are shown in Figure 5.6. The figure also presents the obtained currents flowing through the different components (two diodes and shunts) of each cell. Obtaining these parameters can be useful when investigating fundamental recombination processes within a solar cell [191]. Reasonable fits are obtained for Cells 1 and 6 compared to Cell 3 that could not be fitted well at low voltages. The fit parameters are summarized in Table 5. along with  $R_{sh}$  measured from the light  $I$ - $V$  measurement (also presented in Table 4.2). It is noticeable that the extracted  $J_{02}$  of Cell 3 is larger compared to the other cells. Hence, the influence of the depletion region or edge recombination extends to a larger voltage range. As this extends beyond MPP, there is a subsequent reduction in the cell efficiency.

Furthermore, the larger total recombination current of Cell 3 leads to a strongly reduced  $V_{oc}$ . The extracted  $R_{sh}$  of Cells 1 and 3 is significantly low, similar to the findings from the  $I$ - $V$  measurement (Table 4.2). However, there is a significant difference between the  $R_{sh}$  of Cell 3 obtained by the two methods. This discrepancy is probably due to the unreliable fit for this cell at low illumination intensities.

In order to gain additional information, the local ideality factor as a function of voltage (the  $m$ - $V$  curve) is calculated using:

$$m = \frac{dV}{d \ln(J_L) \times V_T} \quad (5.4)$$

Such  $m$ - $V$  curves can be very useful, since the efficiency limiting degradation mechanisms in a solar cell are not always obvious from standard  $I$ - $V$  curves [141], [191]–[193]. The  $m$ - $V$  curve reveals more information by highlighting the shape of the  $I$ - $V$  curve that might otherwise go unnoticed [141].

Figure 5.7 presents the  $m$ - $V$  curves obtained by Suns-PL ( $m$ - $iV_{oc}$ ) and Suns- $V_{oc}$  ( $m$ - $V_{oc}$ ) measurements for the three cells together with their corresponding two-diode model fits ( $m$ -2Dfit). The good agreement between the  $m$ - $iV_{oc}$  and  $m$ - $V_{oc}$ , even for such a sensitive parameter (as  $m$  is calculated from the derivative of the measured data), strongly validates the proposed method. However, the measurements cannot be fitted by the two-diode model, revealing the limitation of this model. This is because the simplified standard two diode model fit does not capture other recombination processes, such as the resistance-limited enhanced recombination [194]. Figure 5.7, therefore, also includes the fits obtained by a three-diode model ( $m$ -3Dfit) without the influence of  $R_s$  whose equivalent circuit is given in Figure 5.8 and  $J$ - $V$  characteristics is given by:

$$J = J_L - J_{01} \left( \exp \left( \frac{V}{m_1 V_T} \right) - 1 \right) - J_{02} \left( \exp \left( \frac{V}{m_2 V_T} \right) - 1 \right) - J_H - \frac{V}{R_s} \quad (5.5)$$

where  $J_H = J_{0H} \left( \exp \left( \frac{V_H}{m_H V_T} \right) - 1 \right)$ ,  $V_H = V - R_H J_H$  and  $J_{0H}$  is the saturation current density of the diode with ideality factors  $m = H$ . These fits match the measured data significantly better. The extracted three-diode model fit parameters are summarised in



Table 5.2.

The height and extension of the hump in the  $m$ - $V$  data is related to the recombination current ( $J_{0H}$ ), whereas the hump position is correlated with the resistance ( $R_H$ ) that separates the localized recombination regions from the remaining regions of the solar cell [141]. The humps of Cell 1 and 3 are higher and extend over a larger voltage range, indicating higher  $J_{0H}$ . For Cell 3, even at very high voltages (690 mV),  $m$  is greater than one, implying that even in this voltage range the recombination is not solely dominated by  $J_{0I}$ . We assume the localized dark spots in the PL image of this cell (as presented in Figure 4.11) leads to localized recombination regions.

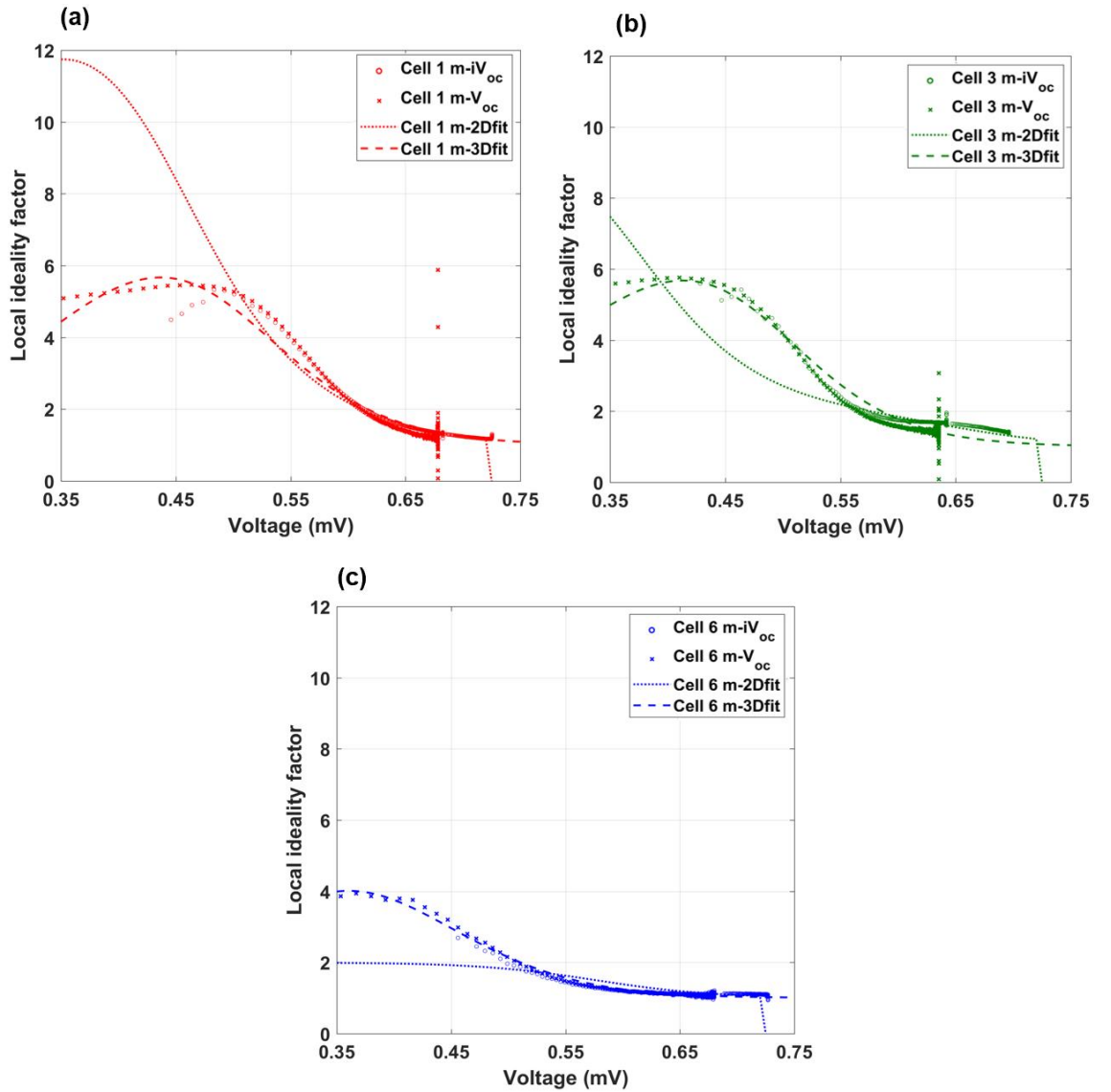


**Figure 5.7** Local ideality factor of  $iV_{oc}$  and  $V_{oc}$ , together with their two-diode and three-diode model fits.

Table 5.2: Three diode model fit parameters

| Cell ID | $J_{01}$<br>[pA/cm <sup>2</sup> ] | $J_{02}$<br>[nA/cm <sup>2</sup> ] | $R_{sh}$<br>[k cm <sup>2</sup> ] | $J_{0H}$<br>[nA/cm <sup>2</sup> ] | $R_H$<br>[k cm <sup>2</sup> ] | $pFF$<br>[%] |
|---------|-----------------------------------|-----------------------------------|----------------------------------|-----------------------------------|-------------------------------|--------------|
| 1       | 0.11                              | 36.10                             | 2.6                              | 18.92                             | 0.10                          | 72.87        |
| 3       | 0.42                              | 75.72                             | 0.8                              | 26.50                             | 0.12                          | 71.57        |
| 6       | 0.13                              | 7.60                              | infinity                         | 2.71                              | 4.01                          | 82.59        |

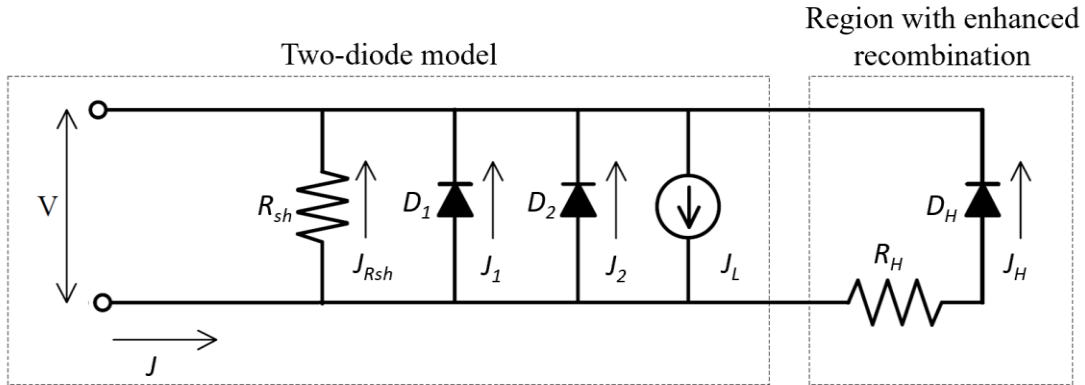


**Figure 5.8** Equivalent circuit model of the three-diode model comprising of the standard two-diode model representing the main body of the cell and a third diode series connected via a resistor representing a region of enhanced recombination [141].

### 5.5.3 Outdoor measurements

In this section, the application of the proposed Suns-PL method for outdoor measurements is discussed. Here the fact that modules are operated at MPP causes extra complications. As Suns-PL measurements require OC conditions [24], [176], they can easily be performed on solar systems at night time, when no power is produced, and hence no current is flowing.

However, night measurements are usually undesirable due to safety and practical considerations. For day measurements under sunlight irradiation, while the module is biased by the MPP tracker, power is extracted from the module. For this reason, the

investigated cells need to be forced into OC condition by shading a cell in a series connected sub-string, reducing the current through the corresponding sub-string to approximately zero and thus engaging the corresponding by-pass diode as proposed in Section 3.1. Using the fabricated mini-module, the proposed Suns-PL method is tested (using the setup described in Section 5.4) under approximately one-Sun daylight illumination, while the module is biased with an electronic load such that the MPP power is extracted.

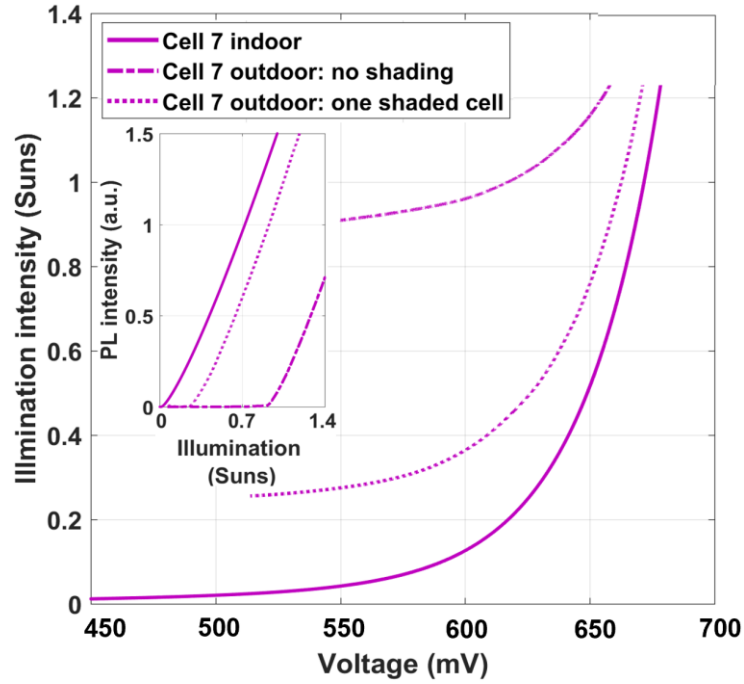


**Figure 5.9** Implied  $I$ - $V$  curves of Cell 7 measured indoor (without shading) and outdoor under different shading conditions; PL intensity as a function of illumination intensity is shown as an inset.

Figure 5.9 displays indoor and outdoor Suns-PL measurements of Cell 7 (a weakly shunted non-degraded cell). As can be seen, there is a large discrepancy between the measurements, causing an offset in the implied  $I$ - $V$  curves. This significant difference arises due to the investigated cell (test cell) not being under OC conditions during the measurement since some current still flows through all the cells. This current will be highly variable and change with the illumination intensity on the test cell as it receives the minimum illumination in the sub-string until it reaches  $I_{MPP}$ . In the measured case the sunlight was almost perpendicular to the module surface and hence all cells except Cell 7 received full illumination. Therefore, the test cell, that is shaded by the measurement system ('Cell 7 outdoor: no shading'), is reverse biased until the light induced current  $I_L$  exceeds the  $I_{MPP}$  (when test cell illumination is greater than other series connected cells),

as can be seen with the inset of Figure 5.9. As a result, there is no PL signal for illumination intensities  $I_L \leq I_{MPP}$ .

The situation is expected to be improved by shading additional cells in the same string. When one additional series connected cell is shaded (Cell 1 was used in here as an example), we expect the investigated cell (Cell 7) is expected to be forced to the OC condition in an ideal case. In this case, the obtained implied  $I$ - $V$  curve should be similar to that obtained indoors. However, as can be seen in Figure 5.9 ('Cell 7 outdoor: one shaded cell'), there is still a significant difference compared to the indoor measurements. This can be explained by either one or a combination of the following reasons:

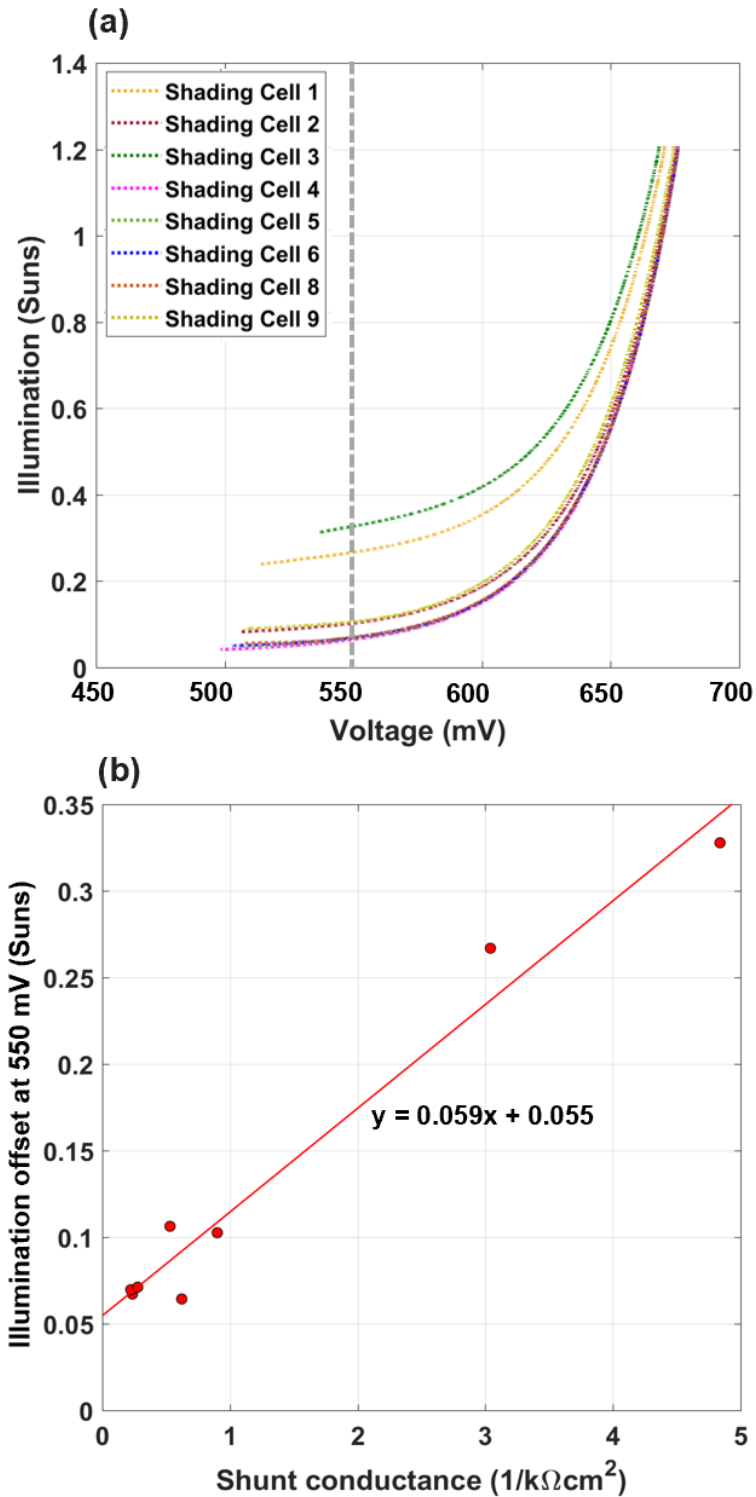
- (1) Significant shunt conductance in the shaded cell.
- (2) Light leakage into the shaded cell from the unshaded module areas.
- (3) Light leakage into the cell under test from unshaded module areas.

In order to investigate the impact of the shunt conductance on the  $I$ - $V$  curve offset, different cells in the mini-module are shaded, while the actual Suns-PL measurement is performed on Cell 7. The results of this measurement are presented in Figure 5.10(a).

A shaded cell is reverse biased by the non-shaded cells, and therefore if shunted, allows a current to flow through the series-connected non-shaded cells (including the test cell). Thus, a shunted shaded cell prevents the test cell from reaching the OC condition, causing an offset in the measured  $I$ - $V$  curves that depends on the level of shunting present in the shaded cell. In Figure 5.10(b) the relationship between shunt conductance (based on the measured  $R_{sh}$  of Table 5.) and the offset in the  $I$ - $V$  curves [measured at 550 mV, see dashed vertical line in Figure 5.10(a)] are presented. As expected, roughly a linear relationship between illumination offset and shunt conductance is observed. However, even when a non-shunted and non-degraded cell (Cell 6) is chosen as the shaded cell [blue curve in Figure 5.10(a)], the implied  $I$ - $V$  curve still has a significant offset which is caused by light leakage into the shaded cell from the surrounding areas.

A small amount of light is assumed to penetrate into the shaded cell via internal reflection of sunlight through the module glass [139]. In these measurements, the offset is found to be approximately 0.055 Suns [0.49 A, see Figure 5.10(b)]. The value observed is not always the same and is influenced by the shading technique used. Another source of error in this measurement is light leaking into the test cell. As a result, the penetrating

light reaches the PL detector and causes a small constant offset in  $P_L$ . This has very little impact on the voltages measured at higher illumination intensity but could dramatically alter the lower voltage region of the curve (at lower light intensities). Therefore,  $P_L$  is corrected for all the measurements presented here by shifting the measured PL signal by the offset in measured PL intensity when the LEDs are OFF.



## 5 Implied current-voltage measurements of individual cells in a module

**Figure 5.10** (a) Measured implied  $I$ - $V$  curves of Cell 7 while other cells are individually shaded; (b) illumination offset at 550 mV [represented by the vertical dashed line in (a)] as a function of the shunt conductance of the shaded cell. The red line represents the least squares fit of the data (equation inserted).

To address these challenges, the shading is extended to cover an area slightly larger than the eight neighbouring cells around the test cell (around 20 cm from the edge of the test cell) as shown in Figure 5.11. This has three effects:

- (1) it eliminates the PL offset mentioned above due to the light leaking into the test cell;
- (2) it effectively reduces light leakage into the shaded cells; and
- (3) it dramatically reduces the leakage current via shunt conductance since more cells are shaded and the reverse voltage caused by the shading is distributed amongst all of them.



**Figure 5.11** Modified experimental setup of Suns-PL tool.

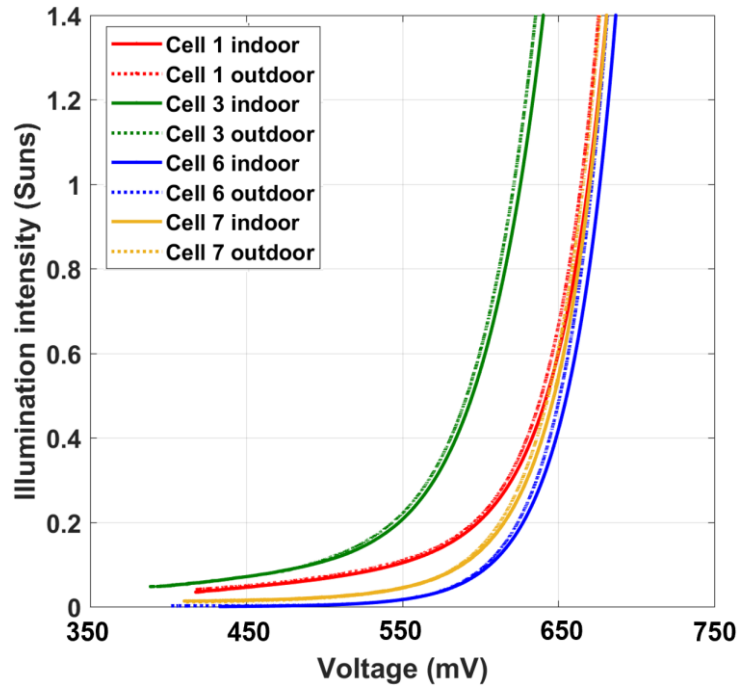


**Figure 5.12** Comparison of indoor measurements (solid lines) and outdoor implied I-V measurements (dotted lines) obtained with the extended shading approach for selected cells of the mini-module.

The results obtained using this extended shading method are shown in Figure 5.12. The obtained outdoor *I-V* measurements now very closely match those obtained indoors. The slight deviations that still exist (in the range of 4-5 mV at one Sun) are assumed to be due to temperature differences, as indoor measurements were performed at 25 °C, whereas the outdoor measurements were taken at around 50 °C. This difference can be corrected for taking into account the temperature coefficient for Suns-PL measurements, as will be discussed in the next section.

#### 5.5.4 Impact of temperature

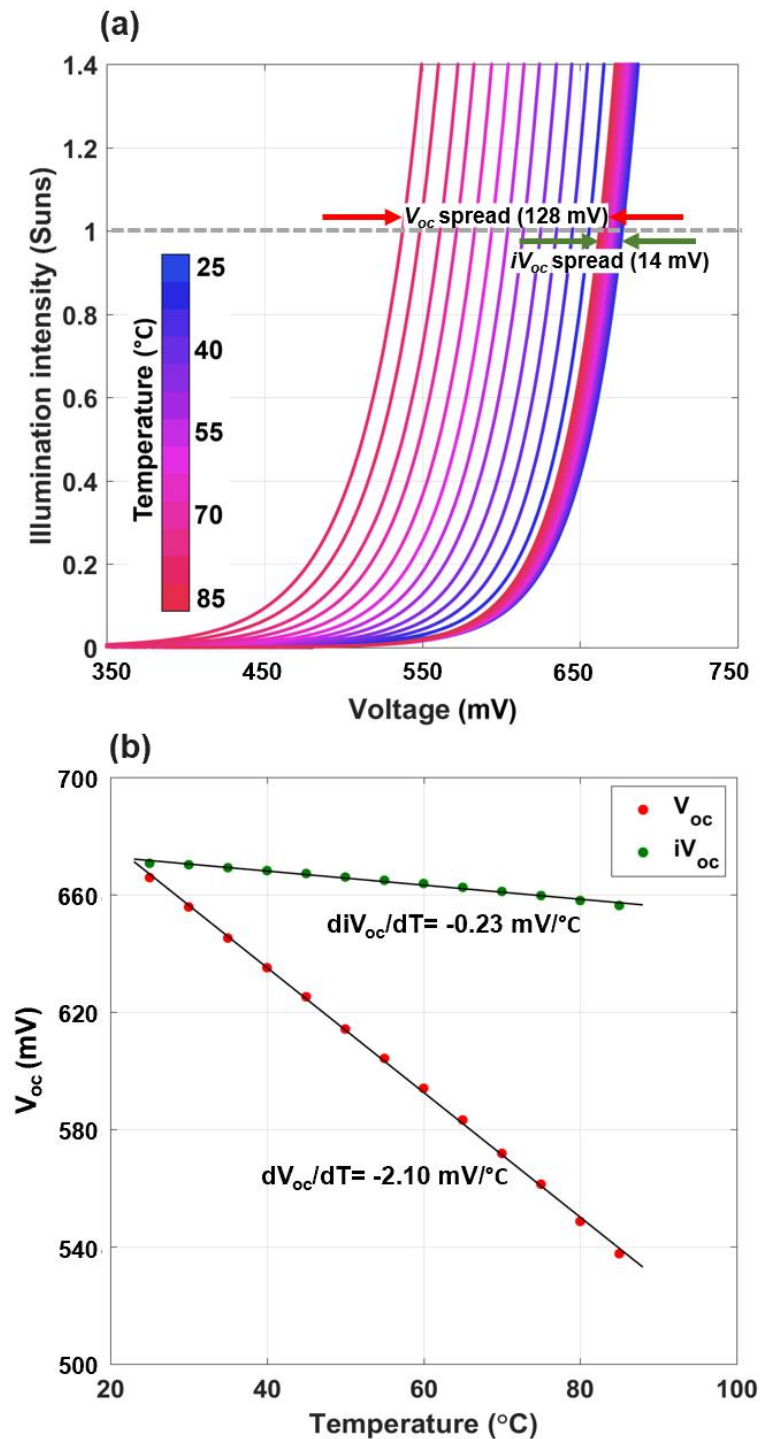
Outdoor measurements are naturally taken at a large range of module temperatures. When considering this it is essential that the analysis is only minimally affected by the different outdoor conditions. In this section the effect of temperature on Suns-PL measurements is investigated.

Figure 5.13(a) presents indoor Suns- $V_{oc}$  and Suns-PL measurements of Cell 6 over the temperature range from 25 °C to 85 °C. At each temperature, the two measurements are performed simultaneously using uniform heating from a large area halogen lamp. The temperature was measured using a LM35 sensor [195] attached firmly to the back of the tested solar cell.

## 5 Implied current-voltage measurements of individual cells in a module

Over the entire temperature range, the spread of  $V_{oc}$  is 128 mV, consistent with a temperature coefficient of  $\sim -2.13$  mV/K. In contrast, the equivalent voltage spread from Suns-PL measurements ( $iV_{oc}$ ) is only 14 mV, almost one order of magnitude smaller. The evolution of  $V_{oc}$  and  $iV_{oc}$  as a function of temperature is shown in Figure 5.13(b). The difference between  $V_{oc}$  and  $iV_{oc}$  at 25 °C is observed to be 5 mV, similar to the value reported in [176]. The  $iV_{oc}$  temperature coefficient is much smaller than the temperature coefficient of  $V_{oc}$  ( $-0.23$  mV/°C), indicating that Suns-PL measurements are resistant to changes in temperature that are expected during solar power plant operation. The lower  $iV_{oc}$  temperature coefficient derives from the luminescence intensity having only a weak temperature dependency in the range around room temperature. As  $iV_{oc} \propto \ln(I_{PL})$ , this dependency is even weaker for  $iV_{oc}$  as discussed by Zafirovska *et al.* [179]. Implied  $I$ - $V$  data from Suns-PL are thus found to be extremely robust to temperature variations, which means that only an approximate cell temperature is required to effectively correct for the temperature differences. Such a temperature estimate can, for instance, be conveniently obtained by using a remote infrared thermometer.





**Figure 5.13** (a) Measured implied  $I$ - $V$  curves obtained by Suns- $V_{oc}$  and Suns-PL measurements at varying module temperatures ranging from 25 °C to 85 °C in steps of 5 °C, (b)  $V_{oc}$  and  $iV_{oc}$  at one Sun [see grey dashed line in (a)] measured as a function of temperature (Cell 6).

## 5.6 Conclusions

The Suns-PL measurement technique was successfully applied to investigate solar cells embedded in a fully assembled modules operating in indoor and outdoor conditions. The method allows contactless extraction of implied  $I$ - $V$  curves of individual cells in full

## 5 Implied current-voltage measurements of individual cells in a module

daylight. The measurement system is highly sensitive, simple, cost effective and fast. Information regarding fundamental loss mechanisms, such as recombination current or shunt resistance can be easily obtained. Furthermore, the quality of the measurement is sufficient to extract the local ideality factor, a sensitive tool to investigate recombination mechanisms present in solar cells. An easy way to calibrate implied  $I$ - $V$  curves was discussed. The effect of measurement artefacts from insufficient shading was investigated and quantified. Measurements confirmed that the technique is almost unaffected by temperature variations as is expected during outdoor field measurements.

The proposed method can be a very useful and versatile tool for research, as well as for routine testing during operation and maintenance of solar modules in the field.



## Chapter 6

### Summary and future works

#### 6.1 Summary

The major aim of this thesis is to develop new characterization methods to improve field inspection of Si PV modules.

Chapter 2 reviewed the important components of the PV system, different degradation modes found in fielded modules and several cell and module inspection techniques currently used to identify them. From the review, the basic module inspection techniques involving visual inspections and module  $I$ - $V$  measurements were noted to be limited to identifying only the faults that produce visually noticeable consequences and information regarding the specific performance limiting region within the module respectively. It was understood that UV fluorescence is applicable only with modules with a specific time regime of field exposure, whereas IR thermography is a cost-effective, fast and contactless imaging-based technique but limited to identifying only the defects that cause temperature changes. On the other hand, although luminescence-based imaging techniques provide detailed spatial information, the existing techniques in the literature were found to be limited in terms of low light operation, need for special hardware, time consuming cell by cell imaging or the need for contacting the module terminals. It was observed that, to extract the  $I$ - $V$  information of individual solar cells in a module, the existing methods demanded a qualified electrician and sometimes sophisticated equipment limiting or even preventing their use for routine inspection in the field.

Chapter 3 presents a novel PL imaging technique for fielded modules that address the gaps identified in Chapter 2. The methodology to contactlessly modulate the PL emission from solar cells in field-deployed modules by changing the optical generation rate of one or more solar cells in the module is presented. Initially, the proof of concept was demonstrated using spectral measurement in outdoor conditions followed by designing and building of outdoor PL imaging system based on the developed contactless modulation approach. The camera and filter for the system were carefully chosen based

on the ratio of the PL signal to the total measured signal (PL and diffused sunlight). The theory behind the *sequential* switching approach and the process of acquiring the final outdoor PL image from multiple image-pairs were explained. The application of the proposed method to detect OC BPD failure was presented. Finally, the inability of the *sequential* method with systems that feature MLPE was discussed.

To overcome the problem of measuring modules with MLPE, Chapter 4 proposes a new contactless method, the *batch* method, which is simpler than the *sequential* method. As the *batch* method requires the change in LED status from ON to OFF only once, it is expected to work with all types of installations, even those that use module-level MPPT. The *batch* method is further improved to include correction for sunlight changes. The so-called *offset corrected batch* measurement increases the robustness to sunlight changes during the measurements. A detailed noise analysis procedure along with the noise analysis results of the existing camera was presented. The image quality was analyzed using a suitable approach to determine image SNR. It was found that the outdoor PL image quality is higher for measurements performed around solar noon, for modules with higher cell  $V_{oc}$  and higher control cell  $R_{sh}$ . The developed method was demonstrated to investigate the quality of solar arrays used on a solar race car and field-deployed solar modules in a large scale solar farm. As part of this chapter, a method to extract spatial  $R_s$  information in solar modules was developed.

Chapter 5 proposed a complementary characterization approach that makes use of the Suns-PL method to extract  $I$ - $V$  measurements of individual solar cells that are field-deployed and producing power. The chapter discussed simple methods to calibrate Suns-PL curves to convert them into implied  $I$ - $V$  curves and provided a comparison between existing and the proposed methods. The application of the tool to identify fundamental loss mechanisms, such as recombination current or  $R_{sh}$  was presented. The measured  $I$ - $V$  curves were validated using Suns- $V_{oc}$  measurements and it was observed that both were in close agreement. The effect of measurement artefacts from insufficient shading was investigated and quantified for application in outdoor conditions. The proposed method was demonstrated to be highly sensitive yet unaffected by temperature changes as they are expected during outdoor field measurements.

### 6.2 Contributions

This thesis makes the following contributions to the existing literature. Two novel contactless, versatile and easily applicable field inspection techniques are developed: (1) outdoor PL imaging system and (2) Suns-PL system. With an extensive review of existing literature, it is observed that an inspection technique of this kind has not been explored before.

The beauty of the outdoor PL imaging technique developed in this thesis lies in the fact that it uses a simple shading approach that relies on the functionality of bypass diodes and the sun as the sole source of excitation. Further, the developed outdoor PL imaging system is capable to detect OC BPD failure leading to reduced hot spot risk in PV systems. Interestingly, this failure reveals itself during the outdoor PL imaging through the inability to modulate the PL emission while the shading is changed.

The step-by-step procedure to perform camera noise analysis presented in this thesis enables the user to choose the InGaAs camera with the right specifications for outdoor PL imaging along with noise estimation for SNR analysis. Furthermore, this thesis extensively analyses the parameters with maximum impact on the SNR which would help in the understanding of expected SNR for a specific module depending on the location, date and time of measurement.

For the first time, a method was proposed in this thesis to quantify the  $R_s$  of isolated areas in fielded PV module contactlessly. This method uses the outdoor PL images obtained at different current extraction conditions by changing the LED illumination intensity on the control cell. With this set of images and the average  $R_s$  of the cell, the  $R_s$  of the isolated area can be quantified using a simple two diode equivalent circuit model of a solar cell. This method would be immensely beneficial in distinguishing the  $R_s$  degradation from lifetime degradation in fielded modules.

A complimentary cost-effective Suns-PL system developed in this thesis provides a deeper insight into the fundamental degradation mechanisms compared to the outdoor PL imaging system. This system is capable of identifying the typical failure modes in fielded PV systems such as LID and PID degradation modes.

The two novel methods proposed in this thesis can be very useful in failure detection in the state of art modules in PV power plants and be used at the commissioning stage to

detect potential failures caused during transportation and installation or for routine inspection during operation and maintenance of solar power plants.

### **6.3 Future works**

There are several opportunities to advance the work done in this thesis:

From a hardware point-of-view, to avoid the image registration issues between image-pairs due to the movement of the camera caused by wind during the measurement, a high frame rate camera can be used and gimbal mounting can be included with the camera in the outdoor PL imaging system.

From a software point-of-view, the outdoor PL imaging system proposed in this thesis obtains the final PL image of PV modules using multiple image-pairs with post-processing algorithms. There is a scope of automating this process for real-time application with advanced live-streaming software which will significantly reduce the overall inspection time, leading to large scale field implementation of the proposed method. Further, artificial intelligence can be used for automatically identifying the different fault mechanisms in the degraded modules along with their severity levels.

The proposed techniques can be used for quantitative analysis of module degradation. The effect of module temperature on the SNR of PL images can be investigated. Alternative shading options such as percentage mesh-based shading can be used instead of LEDs to achieve different irradiation. Using the developed method to create a database of faults in fielded modules is highly valuable. Using statistical tools, the data can then be analyzed to provide reliable information to PV developers, investors, and manufacturers. To obtain millions of images, the proposed outdoor imaging measurement approach can be implemented with unmanned aerial vehicles (UAVs) or drones with modifications such as the use of a lightweight and battery-operated camera, installing onboard processor to control the camera trigger signal, synchronize the LED, and to temporarily store captured images etc. However, in this case, the LEDs will be used to switch the complete string, not only an individual sub-string. This drone integration will enable the inspection of large PV farms in a short span of time.

The capabilities of the proposed method can also be extended to inspect other silicon module technologies (like shingled and half-cut), non-Si modules [such as cadmium

telluride (CdTe) and copper indium gallium selenide (CIGS)], building integrated PV and solar space vehicles.

### **6.4 Final remarks**

As solar energy has become the cheapest form of electricity, more solar power farms are being built while the existing coal-fired power plants are retiring. One of the most effective ways solar can continue being the cheapest form of electricity is by having longer durability achieving a high return on investment. Solar modules degrade in many ways during transportation, installation and operation. Early detection of these degradation modes will be immensely beneficial in mitigating or even preventing power loss in PV systems. The techniques available currently for field inspection are less attractive in terms of complexity and applicability to large solar farms. Hence, it has never been timely enough to develop new cost-effective, fast and easily applicable inspection techniques to prepare the ground for the solar industry to reap maximum benefit from such novel inspection techniques. The main purpose of this thesis has been to contribute to this expedition letting the solar industry continue to thrive towards a 100% renewable-powered future.





## References

- [1] “List of Worldwide Scientific Organizations - Office of Planning and Research.” <https://www.opr.ca.gov/facts/list-of-scientific-organizations.html> (accessed Jul. 22, 2020).
- [2] “World Scientists’ Warning of a Climate Emergency | BioScience | Oxford Academic.” <https://academic.oup.com/bioscience/article/70/1/8/5610806> (accessed Jul. 22, 2020).
- [3] “The Energy Innovators: A solar boost to the mining industry - Australian Renewable Energy Agency.” <https://arena.gov.au/blog/the-energy-innovators-martin-green/> (accessed Jul. 22, 2020).
- [4] R. Perez and M. J. R. Perez, “A fundamental look at energy reserves for the planet,” *Int. Energy Agency SHC Program. Sol. Updat.*, vol. 50, pp. 2–3, 2009, Accessed: Jul. 22, 2020. [Online]. Available: [https://www.researchgate.net/publication/237440187\\_A\\_fundamental\\_look\\_at\\_energy\\_reserves\\_for\\_the\\_planet](https://www.researchgate.net/publication/237440187_A_fundamental_look_at_energy_reserves_for_the_planet).
- [5] “International Technology Roadmap for Photovoltaic (ITRPV) Eleventh Edition (2020).” <http://itrpv.vdma.org/download> (accessed Jul. 12, 2020).
- [6] “Quarterly prices of photovoltaic modules United States 2020 | Statista.” <https://www.statista.com/statistics/216791/price-for-photovoltaic-cells-and-modules/> (accessed Aug. 04, 2020).
- [7] M. A. Green, “Photovoltaic technology and visions for the future,” *Prog. Energy*, vol. 1, no. 1, p. 013001, 2019, doi: 10.1088/2516-1083/ab0fa8.
- [8] “World now has 583.5 GW of operational PV – pv magazine International.” <https://www.pv-magazine.com/2020/04/06/world-now-has-583-5-gw-of-operational-pv/> (accessed Aug. 04, 2020).
- [9] “Global solar capacity grew faster than fossil fuels in 2017, says report | Carbon Brief.” <https://www.carbonbrief.org/global-solar-capacity-grew-faster-than-fossil-fuels-2017-report> (accessed Jul. 25, 2020).
- [10] J. Jean, M. Woodhouse, and V. Bulović, “Accelerating photovoltaic market entry with module replacement,” *Joule*, vol. 3, no. 11, pp. 2824–2841, 2019, doi: 10.1016/j.joule.2019.08.012.
- [11] K. Branker, M. J. M. Pathak, and J. M. Pearce, “A review of solar photovoltaic levelized cost of electricity,” *Renew. Sustain. Energy Rev.*, vol. 15, no. 9, pp. 4470–4482, 2011, doi: 10.1016/j.rser.2011.07.104.

- [12] A. Limmanee *et al.*, “Degradation analysis of photovoltaic modules under tropical climatic conditions and its impacts on LCOE,” *Renew. Energy*, vol. 102, pp. 199–204, 2017, doi: 10.1016/j.renene.2016.10.052.
- [13] T. Trupke and R. A. Bardos, “Photoluminescence: a surprisingly sensitive lifetime technique,” *Conf. Rec. Thirty-first IEEE Photovolt. Spec. Conf. 2005.*, pp. 903–906, 2005, doi: 10.1109/PVSC.2005.1488277.
- [14] T. Trupke *et al.*, “Progress with luminescence imaging for the characterisation of silicon wafers and solar cells,” 2007.
- [15] L. Stoicescu, M. Reuter, and J. Werner, “Daysy: luminescence imaging of PV modules in daylight,” in *29th European Photovoltaics Solar Energy Conference and Exhibition*, 2014, pp. 2553–2554.
- [16] T. Uberg Naerland, H. Angelskär, and E. Stensrud Marstein, “Direct monitoring of minority carrier density during light induced degradation in Czochralski silicon by photoluminescence imaging,” *J. Appl. Phys.*, vol. 113, p. 193707, 2013, doi: 10.1063/1.4806999.
- [17] A. Mansouri, M. Zettl, O. Mayer, M. Lynass, M. Bucher, and O. Stern, “Defect detection in photovoltaic modules using electroluminescence imaging,” in *27th European Photovoltaic Solar Energy Conference and Exhibition*, 2012, pp. 3374–3378.
- [18] R. Ebner, B. Kubicek, G. Újvári, S. Novalin, M. Rennhofer, and M. Halwachs, “Optical characterization of different thin film module technologies,” *Int. J. Photoenergy*, vol. 2015, no. June, pp. 1–12, 2015, doi: 10.1155/2015/159458.
- [19] T. Trupke, R. A. Bardos, and M. D. Abbott, “Self-consistent calibration of photoluminescence and photoconductance lifetime measurements,” *Appl. Phys. Lett.*, vol. 87, no. 18, pp. 1–3, Oct. 2005, doi: 10.1063/1.2119411.
- [20] M. D. Abbott, R. A. Bardos, T. Trupke, K. C. Fisher, and E. Pink, “The effect of diffusion-limited lifetime on implied current voltage curves based on photoluminescence data,” *J. Appl. Phys.*, vol. 102, no. 4, 2007, doi: 10.1063/1.2756529.
- [21] B. Mitchell, J. W. Weber, M. Juhl, D. Macdonald, and T. Trupke, “Photoluminescence imaging of silicon bricks,” *Solid State Phenom.*, vol. 205–206, pp. 118–127, 2013, doi: 10.4028/www.scientific.net/SSP.205-206.118.
- [22] I. Zafirovska, M. Juhl, J. Weber, O. Kunz, and T. Trupke, “Module inspection using line scanning photoluminescence imaging,” *32nd Eur. Photovolt. Sol. Energy Conf. Exhib.*, 2016, Accessed: Feb. 13, 2017. [Online]. Available: [https://www.researchgate.net/profile/Iskra\\_Zafirovska/publication/305654143\\_Module\\_Inspection\\_Using\\_Line\\_Scanning\\_Photoluminescence\\_Imaging/links/5797f65808ae33e89faedd9a.pdf](https://www.researchgate.net/profile/Iskra_Zafirovska/publication/305654143_Module_Inspection_Using_Line_Scanning_Photoluminescence_Imaging/links/5797f65808ae33e89faedd9a.pdf).
- [23] Z. Hameiri, T. Trupke, N. Gao, R. A. Sinton, and J. W. Weber, “Effective bulk doping concentration of diffused and undiffused silicon wafers obtained from combined photoconductance and photoluminescence measurements,” *Prog.*

## References

- Photovoltaics Res. Appl.*, vol. 21, pp. 942–949, 2013, doi: 10.1002/pip.
- [24] T. Trupke, R. A. Bardos, M. D. Abbott, and J. E. Cotter, “Suns-photoluminescence: Contactless determination of current-voltage characteristics of silicon wafers,” *Appl. Phys. Lett.*, vol. 87, pp. 2005–2007, 2005, doi: 10.1063/1.2034109.
- [25] L. El Chaar, L. A. Lamont, and N. El Zein, “Review of photovoltaic technologies,” *Renew. Sustain. Energy Rev.*, vol. 15, no. 5, pp. 2165–2175, 2011, doi: 10.1016/j.rser.2011.01.004.
- [26] “Mini series: On prices, technology and 2019 trends.” <https://www.pv-magazine.com/2019/08/23/mini-series-on-prices-technology-and-2019-trends/> (accessed May 13, 2020).
- [27] O. S. Sastry *et al.*, “Performance analysis of field exposed single crystalline silicon modules,” *Sol. Energy Mater. Sol. Cells*, vol. 94, no. 9, pp. 1463–1468, 2010, doi: 10.1016/j.solmat.2010.03.035.
- [28] “Solar panel construction.” <https://www.cleanenergyreviews.info/blog/solar-panel-components-construction> (accessed May 13, 2020).
- [29] M. Kempe, “Encapsulant Materials for PV Modules,” in *Photovoltaic Solar Energy*, Chichester, UK: John Wiley & Sons, Ltd, 2017, pp. 478–490.
- [30] “Does the frame of solar panels really matter?” <https://www.aleo-solar.com/frame-solar-panels/> (accessed Jul. 12, 2020).
- [31] C. Peike, I. Hädrich, K. Weiß, I. Dürr, and F. Ise, “Overview of PV module encapsulation materials,” *Photovoltaics Int.*, vol. 19, pp. 85–92, 2013.
- [32] B. B. Pannebakker, A. C. de Waal, and W. G. J. H. M. van Sark, “Photovoltaics in the shade: one bypass diode per solar cell revisited,” *Prog. Photovoltaics Res. Appl.*, vol. 25, no. 10, pp. 836–849, Oct. 2017, doi: 10.1002/pip.2898.
- [33] A. Luque and S. Hegedus, *Handbook of photovoltaic science and engineering*. John Wiley & Sons Ltd, 2003.
- [34] S. B. Kjaer, J. K. Pedersen, and F. Blaabjerg, “Power inverter topologies for photovoltaic modules - A review,” in *37th IEEE Industry Applications Conference*, 2002, vol. 2, pp. 782–788, doi: 10.1109/ias.2002.1042648.
- [35] K. Sinapis, G. Litjens, M. van den Donker, W. Folkerts, and W. van Sark, “Outdoor characterization and comparison of string and MLPE under clear and partially shaded conditions,” *Energy Sci. Eng.*, vol. 3, pp. 510–519, 2015, doi: 10.1002/ese3.97.
- [36] R. Angele, Verlinden Pierre, S. van; Wilfried, and F. Alexandre, *Photovoltaic solar energy: from fundamentals to applications*. 2017.
- [37] “Koppen climate classification.” <https://www.britannica.com/science/Koppen-climate-classification> (accessed May 14, 2020).

- [38] K. Slamova, "Mapping atmospheric corrosion in coastal regions: methods and results," *J. Photonics Energy*, vol. 2, pp. 1–11, 2012, doi: 10.1117/1.jpe.2.022003.
- [39] M. Köntges *et al.*, "Review of failures of photovoltaic modules," *IEA-Photovoltaic Power Syst. Program.*, pp. 1–140, 2014.
- [40] M. Köntges *et al.*, "Assessment of photovoltaic module failures in the field," *IEA-Photovoltaic Power Syst. Program.*, pp. 1–119, 2017, [Online]. Available: [http://www.iea-pvps.org/index.php?id=92&eID=dam\\_frontend\\_push&docID=4059](http://www.iea-pvps.org/index.php?id=92&eID=dam_frontend_push&docID=4059).
- [41] D. C. Jordan, T. J. Silverman, J. H. Wohlgemuth, S. R. Kurtz, and K. T. Vansant, "Photovoltaic failure and degradation modes," *Prog. Photovolt Res. Appl.*, vol. 25, pp. 318–326, 2017, doi: 10.1002/pip.
- [42] N. C. Park, J. S. Jeong, B. J. Kang, and D. H. Kim, "The effect of encapsulant discoloration and delamination on the electrical characteristics of photovoltaic module," in *Microelectronics Reliability*, Sep. 2013, vol. 53, no. 9–11, pp. 1818–1822, doi: 10.1016/j.microrel.2013.07.062.
- [43] D. C. Jordan and S. R. Kurtz, "Photovoltaic degradation rates—an analytical review," *Prog. Photovoltaics Res. Appl.*, vol. 21, pp. 12–29, 2013, doi: 10.1002/pip.
- [44] M. A. Mikofski *et al.*, "a Dynamic Cell-By-Cell Pv System Model To Predict Lifetime Performance and Reliability," in *26th European Photovoltaic Solar Energy Conference and Exhibition*, 2011, pp. 105–112, doi: 10.4229/26thEUPVSEC2011-1BO.10.1.
- [45] M. A. Mikofski *et al.*, "PVLIFE: An integrated model for predicting PV performance degradation over 25+ years," in *38th IEEE Photovoltaic Specialists Conference*, 2012, pp. 1744–1749, doi: 10.1109/PVSC.2012.6317932.
- [46] J. H. Wohlgemuth, M. D. Kempe, and D. C. Miller, "Discoloration of PV encapsulants," in *39th IEEE Photovoltaic Specialists Conference*, 2013, pp. 3260–3265, doi: 10.1109/PVSC.2013.6745147.
- [47] E. E. Van Dyk, J. B. Chamel, and A. R. Gxasheka, "Investigation of delamination in an edge-defined film-fed growth photovoltaic module," *Sol. Energy Mater. Sol. Cells*, vol. 88, no. 4, pp. 403–411, Sep. 2005, doi: 10.1016/j.solmat.2004.12.004.
- [48] A. R. Gxasheka, E. E. Van Dyk, and E. L. Meyer, "Evaluation of performance parameters of PV modules deployed outdoors," *Renew. Energy*, vol. 30, no. 4, pp. 611–620, Apr. 2005, doi: 10.1016/j.renene.2004.06.005.
- [49] L.-E. Perret-Aebi *et al.*, "Insights on EVA lamination process: Where do the bubbles come from?," in *5th World Conference on Photovoltaic Energy Conversion*, 2010, pp. 4036–40038, Accessed: May 14, 2020. [Online]. Available: [https://www.researchgate.net/publication/47806645\\_Insights\\_on\\_EVA\\_lamination\\_process\\_Where\\_do\\_the\\_bubbles\\_come\\_from](https://www.researchgate.net/publication/47806645_Insights_on_EVA_lamination_process_Where_do_the_bubbles_come_from).
- [50] M. D. Kempe, "Modeling of rates of moisture ingress into photovoltaic modules,"

## References

- Sol. Energy Mater. Sol. Cells*, vol. 90, no. 16, pp. 2720–2738, Oct. 2006, doi: 10.1016/j.solmat.2006.04.002.
- [51] D. C. Jordan, J. H. Wohlgemuth, and S. R. Kurtz, “Technology and climate trends in PV module degradation,” in *27th European Photovoltaic Solar Energy Conference and Exhibition*, Oct. 2012, pp. 3118–3124, doi: 10.4229/27thEUPVSEC2012-4DO.5.1.
- [52] D. Berman, S. Biryukov, and D. Faïman, “EVA laminate browning after 5 years in a grid-connected, mirror-assisted, photovoltaic system in the Negev desert: effect on module efficiency,” *Sol. Energy Mater. Sol. Cells*, vol. 36, no. 4, pp. 421–432, Apr. 1995, doi: 10.1016/0927-0248(94)00198-7.
- [53] D. L. King, M. A. Quintana, J. A. Kratochvil, D. E. Ellibee, and B. R. Hansen, “Photovoltaic module performance and durability following long-term field exposure,” *Prog. Photovoltaics Res. Appl.*, vol. 8, no. 2, pp. 241–256, Mar. 2000, doi: 10.1002/(SICI)1099-159X(200003/04)8:2<241::AID-PIP290>3.0.CO;2-D.
- [54] M. A. Munoz, M. C. Alonso-García, N. Vela, and F. Chenlo, “Early degradation of silicon PV modules and guaranty conditions,” *Sol. Energy*, vol. 85, no. 9, pp. 2264–2274, 2011, doi: 10.1016/j.solener.2011.06.011.
- [55] M. A. Quintana, D. L. King, T. J. McMahon, and C. R. Osterwald, “Commonly observed degradation in field-aged photovoltaic modules,” in *Conference Record of the IEEE Photovoltaic Specialists Conference*, 2002, pp. 1436–1439, doi: 10.1109/pvsc.2002.1190879.
- [56] W. G. Shin, S. W. Ko, H. J. Song, Y. C. Ju, H. M. Hwang, and G. H. Kang, “Origin of bypass diode fault in c-Si photovoltaic modules: Leakage current under high surrounding temperature,” *Energies*, vol. 11, no. 9, pp. 2416 (1–11), 2018, doi: 10.3390/en11092416.
- [57] R. Andrews and K. Sinclair, “Issues with bypass diodes – pv magazine USA.” <https://pv-magazine-usa.com/2017/09/27/issues-with-bypass-diodes/> (accessed Nov. 30, 2018).
- [58] N. G. Dhere, N. Shiradkar, E. Schneller, and V. Gade, “The reliability of bypass diodes in PV modules,” in *SPIE 8825, Reliability of Photovoltaic Cells, Modules, Components, and Systems VI*, 2013, pp. 88250I (1–8), Accessed: Aug. 23, 2018. [Online]. Available: <http://proceedings.spiedigitallibrary.org/proceeding.aspx?doi=10.1117/12.2026782>.
- [59] K. Kato, “PVResQ!: a research activity on reliability of PV systems from an user’s viewpoint in Japan,” in *Reliability of Photovoltaic Cells, Modules, Components, and Systems IV*, Sep. 2011, vol. 8112, pp. 81120K (1–9), doi: 10.1117/12.896135.
- [60] N. A. Al-Rawi, M. M. Al-Kaisi, and D. J. Asfer, “Reliability of photovoltaic modules II. Interconnection and bypass diodes effects,” *Sol. Energy Mater. Sol. Cells*, vol. 31, no. 4, pp. 469–480, Jan. 1994, doi: 10.1016/0927-0248(94)90189-9.

- [61] K Kato, "A feasibility study on detecting fault and failure in crystalline-Si PV module with wired route tracing device," *J. Jpn Sol. Energy Soc*, vol. 35, no. 1, pp. 65–72, 2009.
- [62] A. Paduthol, O. Kunz, K. Kaufmann, M. Patzold, D. Lausch, and T. Trupke, "Magnetic Field Imaging: Strengths and limitations in characterising solar cells," in *Conference Record of the IEEE Photovoltaic Specialists Conference*, Jun. 2019, pp. 822–824, doi: 10.1109/PVSC40753.2019.8980950.
- [63] S. Vemuru, P. Singh, and M. Niamat, "Modeling impact of bypass diodes on photovoltaic cell performance under partial shading," in *IEEE International Conference on Electro/Information Technology*, 2012, pp. 1–5, doi: 10.1109/EIT.2012.6220747.
- [64] H. Yoshioka *et al.*, "Non hot-spot PV module using solar cells with bypass diode function," in *25th IEEE Photovoltaic Specialists Conference*, 1996, pp. 1271–1274, doi: 10.1109/pvsc.1996.564364.
- [65] M. Simon and E. L. Meyer, "Detection and analysis of hot-spot formation in solar cells," *Sol. Energy Mater. Sol. Cells*, vol. 99, pp. 362–364, Feb. 2010, doi: 10.1016/j.solmat.2009.09.016.
- [66] W. Herrmann, W. Wiesner, and W. Vaassen, "Hot spot investigations on PV modules - new concepts for a test standard and consequences for module design with respect to bypass diodes," in *26th IEEE Photovoltaic Specialists Conference*, 1997, pp. 1129–1132, doi: 10.1109/pvsc.1997.654287.
- [67] M. Köntges, I. Kunze, S. Kajari-Schröder, X. Breitenmoser, and B. Bjørneklett, "Quantifying the risk of power loss in PV modules due to micro cracks," in *25th European Photovoltaic Solar Energy Conference*, 2010, pp. 3745–3752.
- [68] M. Köntges, S. Kajari-Schröder, and I. Kunze, "Cell cracks measured by UV fluorescence in the field," in *27th European Photovoltaic Solar Energy Conference and Exhibition*, 2012, no. September, pp. 3033–3040, doi: 10.4229/27thEUPVSEC2012-4CO.11.4.
- [69] M. Köntges, S. Kajari-Schröder, I. Kunze, and U. Jahn, "Crack statistic of crystalline silicon photovoltaic modules," in *26th European Photovoltaic Solar Energy Conference and Exhibition*, 2011, vol. 26, pp. 3290–3294, doi: 10.4229/26thEUPVSEC2011-4EO.3.6.
- [70] "Standard IEC 61215:1987, Crystalline silicon terrestrial photovoltaic (PV) modules," *International Electrotechnical Commission*, 1987.
- [71] J. H. Wohlgemuth, D. W. Cunningham, N. V. Placer, G. J. Kelly, and A. M. Nguyen, "The effect of cell thickness on module reliability," in *33rd IEEE Photovoltaic Specialists Conference*, 2008, pp. 1–4, doi: 10.1109/PVSC.2008.4922770.
- [72] B. V. Dobaria, V. Sharma, and A. Adeshara, "Investigation of failure and degradation types of solar PV plants in a composite climate: Abstract after 4–6, years of field operation," in *Advances in Smart Grid and Renewable Energy*, 2018,

- vol. 435, pp. 227–235, doi: 10.1007/978-981-10-4286-7\_22.
- [73] F. Reil, J. Althaus, W. Vaaßen, W. Herrmann, and K. Strohkendl, “The effect of transportation impacts and dynamic load tests on the mechanical and electrical behaviour of crystalline PV modules,” in *25th European Photovoltaic Solar Energy Conference and Exhibition*, 2010, pp. 3989–3992.
  - [74] C. Ferrara and D. Philipp, “Why do PV modules fail?,” *Energy Procedia*, vol. 15, pp. 379–387, Jan. 2012, doi: 10.1016/j.egypro.2012.02.046.
  - [75] G. Mathiak, J. Sommer, W. Herrmann, N. Bogdanski, J. Althaus, and F. Reil, “PV module damages caused by hail impact and non-uniform snow load,” in *32nd European Photovoltaic Solar Energy Conference*, 2016, pp. 1692–1696, Accessed: May 19, 2020. [Online]. Available: <https://www.sunsniffer.de/knowledge/TUEV-Hail.pdf>.
  - [76] S. Pingel *et al.*, “Mechanical stability of solar cells within solar panels,” in *24th European Photovoltaic Solar Energy Conference*, 2009, pp. 3459–3463, doi: 10.4229/24thEUPVSEC2009-4AV.3.49.
  - [77] Kelly Pickerel, “Demystifying the formation of micro-cracks on solar panels.” <https://www.solarpowerworldonline.com/2015/05/demystifying-the-formation-of-micro-cracks-on-solar-panels/> (accessed May 19, 2020).
  - [78] M. Köntges, M. Siebert, A. Morlier, R. Illing, N. Bessing, and F. Wegert, “Impact of transportation on silicon wafer-based photovoltaic modules,” *Prog. Photovoltaics Res. Appl.*, vol. 24, no. 8, pp. 1085–1095, Aug. 2016, doi: 10.1002/pip.2768.
  - [79] “Standard IEC TS 60904-13:2018, Photovoltaic devices - Part 13: Electroluminescence of photovoltaic modules,” *International Electrotechnical Commission*, 2018.
  - [80] M. Kontges, I. Kunze, S. Kajari-Schroder, X. Breitenmoser, and B. Bjørneklett, “The risk of power loss in crystalline silicon based photovoltaic modules due to micro-cracks,” *Sol. Energy Mater. Sol. Cells*, vol. 95, no. 4, pp. 1131–1137, Apr. 2011, doi: 10.1016/j.solmat.2010.10.034.
  - [81] B. Abdellatif *et al.*, “Experimental evaluation of performance drop for crystalline photovoltaic modules affected by snail trails defect,” in *International Conference on Photovoltaic Science and Technologies*, Nov. 2018, pp. 1–5, doi: 10.1109/PVCon.2018.8523959.
  - [82] M. Schütze *et al.*, “Laboratory study of potential induced degradation of silicon photovoltaic modules,” in *37th IEEE Photovoltaic Specialists Conference*, 2011, pp. 821–826, doi: 10.1109/PVSC.2011.6186080.
  - [83] S. Pingel *et al.*, “Potential induced degradation of solar cells and panels,” in *35th IEEE Photovoltaic Specialists Conference*, 2010, pp. 2817–2822, doi: 10.1109/PVSC.2010.5616823.
  - [84] D. Lausch *et al.*, “Potential-induced degradation (PID): Introduction of a novel test



- approach and explanation of increased depletion region recombination,” *IEEE J. Photovoltaics*, vol. 4, no. 3, pp. 834–840, 2014, doi: 10.1109/JPHOTOV.2014.2300238.
- [85] J. Schmidt, A. G. Aberle, and R. Hezel, “Investigation of carrier lifetime instabilities in Cz-grown silicon,” in *Conference Record of the IEEE Photovoltaic Specialists Conference*, 1997, pp. 13–18, doi: 10.1109/pvsc.1997.653914.
  - [86] F. Kersten *et al.*, “Degradation of multicrystalline silicon solar cells and modules after illumination at elevated temperature,” *Sol. Energy Mater. Sol. Cells*, vol. 142, pp. 83–86, 2015, doi: 10.1016/j.solmat.2015.06.015.
  - [87] C. Vargas *et al.*, “Carrier-induced degradation in multicrystalline silicon: dependence on the silicon nitride passivation layer and hydrogen released during firing,” *IEEE J. Photovoltaics*, vol. 8, no. 2, pp. 413–420, Mar. 2018, doi: 10.1109/JPHOTOV.2017.2783851.
  - [88] D. Chen *et al.*, “Hydrogen induced degradation: A possible mechanism for light- and elevated temperature- induced degradation in n-type silicon,” *Sol. Energy Mater. Sol. Cells*, vol. 185, pp. 174–182, Oct. 2018, doi: 10.1016/j.solmat.2018.05.034.
  - [89] K. Ramspeck *et al.*, “Light induced degradation of rear passivated mc-Si solar cells,” in *27th European Photovoltaic Solar Energy Conference and Exhibition*, Oct. 2012, pp. 861–865, doi: 10.4229/27THEUPVSEC2012-2DO.3.4.
  - [90] T. Niewelt, J. Schon, W. Warta, S. W. Glunz, and M. C. Schubert, “Degradation of crystalline silicon due to boron-oxygen defects,” *IEEE J. Photovoltaics*, vol. 7, no. 1, pp. 383–398, Jan. 2017, doi: 10.1109/JPHOTOV.2016.2614119.
  - [91] J. Schmidt, A. G. Aberle, and R. Hezel, “Investigation of carrier lifetime instabilities in Cz-grown silicon,” 2002, doi: 10.1109/pvsc.1997.653914.
  - [92] F. Fertig, K. Krauß, and S. Rein, “Light-induced degradation of PECVD aluminium oxide passivated silicon solar cells,” *Phys. status solidi - Rapid Res. Lett.*, vol. 9, no. 1, pp. 41–46, Jan. 2015, doi: 10.1002/pssr.201409424.
  - [93] L. J. Geerligs and D. Macdonald, “Dynamics of light-induced FeB pair dissociation in crystalline silicon,” *Appl. Phys. Lett.*, vol. 85, no. 22, pp. 5227–5229, Nov. 2004, doi: 10.1063/1.1823587.
  - [94] J. Lindroos, A. Zuschlag, J. Carstensen, and G. Hahn, “Light-induced degradation variation in industrial multicrystalline PERC silicon solar cells,” *AIP Conf. Proc.*, vol. 1999, no. August, 2018, doi: 10.1063/1.5049332.
  - [95] E. S. Kopp, V. P. Lonij, A. E. Brooks, P. L. Hidalgo-Gonzalez, and A. D. Cronin, “I-V curves and visual inspection of 250 PV modules deployed over 2 years in tucson,” in *38th IEEE Photovoltaic Specialists Conference*, 2012, pp. 3166–3171.
  - [96] A. Morlier, M. Siebert, I. Kunze, G. Mathiak, and M. Kontges, “Detecting photovoltaic module failures in the field during daytime with ultraviolet fluorescence module inspection,” in *IEEE Journal of Photovoltaics*, 2017, vol. 7,

- pp. 1710–1716, doi: 10.1109/JPHOTOV.2017.2756452.
- [97] M. Kontges, A. Morlier, G. Eder, E. Fleis, B. Kubicek, and J. Lin, “Review: Ultraviolet fluorescence as assessment tool for photovoltaic modules,” *IEEE J. Photovoltaics*, vol. 10, no. 2, pp. 616–633, 2020, doi: 10.1109/JPHOTOV.2019.2961781.
  - [98] S. Koch, T. Weber, S. Christian, A. Fladung, P. Clemens, and J. Berghold, “Outdoor electroluminescence imaging of crystalline photovoltaic modules: Comparative study between manual ground - level inspections and drone - based aerial surveys,” in *32nd European Photovoltaic Solar Energy Conference and Exhibition*, 2016, pp. 1736–1740.
  - [99] M. Aghaei, P. B. Quater, F. Grimaccia, S. Leva, and M. Mussetta, “Unmanned aerial vehicles in photovoltaic systems monitoring applications,” in *29th European Photovoltaic Solar Energy Conference and Exhibition*, 2014, pp. 2734–2739, doi: 10.1017/CBO9781107415324.004.
  - [100] R. Ebner, B. Kubicek, and G. Ujvari, “Non-destructive techniques for quality control of PV modules: Infrared thermography, electro- and photoluminescence imaging,” in *39th Annual Conference of the IEEE Industrial Electronics Society*, 2013, pp. 8104–8109, doi: 10.1109/IECON.2013.6700488.
  - [101] R. Tscharnner, K. H. . . S. . . Rao, R. Schwarz, and A. V. Shah, “Evaluation of photovoltaic panels with IR thermography,” in *Thermosense VII: Thermal Infrared Sensing for Diagnostics and Control*, Mar. 1985, vol. 0520, p. 130, doi: 10.1117/12.946143.
  - [102] R. Weißmann, H. Scheuerpflug, and C. Buerhop-Lutz, “The role of infrared emissivity of glass on IR-imaging of PV-plants,” in *26th European Photovoltaic Solar Energy Conference and Exhibition*, Oct. 2011, pp. 3413–3416, doi: 10.4229/26THEUPVSEC2011-4AV.1.39.
  - [103] C. Buerhop, D. Schlegel, C. Vodermayr, and M. Nieß, “Quality control of PV-modules in the field using infrared-thermography,” in *26th European Photovoltaic Solar Energy Conference*, Oct. 2011, pp. 3894–3897, doi: 10.4229/26thEUPVSEC2011-5AO.5.2.
  - [104] C. Buerhop, D. Schlegel, M. Niess, C. Vodermayr, R. Weißmann, and C. J. Brabec, “Reliability of IR-imaging of PV-plants under operating conditions,” *Sol. Energy Mater. Sol. Cells*, vol. 107, pp. 154–164, Dec. 2012, doi: 10.1016/j.solmat.2012.07.011.
  - [105] T. Kaden, K. Lammers, and H. J. Möller, “Power loss prognosis from thermographic images of PID affected silicon solar modules,” *Sol. Energy Mater. Sol. Cells*, vol. 142, pp. 24–28, 2015, doi: 10.1016/j.solmat.2015.05.028.
  - [106] A. M. Salazar and E. Q. B. Macabebe, “Hotspots detection in photovoltaic modules using infrared thermography,” in *MATEC We3rd International Conference on Manufacturing and Industrial Technologiesb of Conferences*, 2016, vol. 70, p. 10015, doi: 10.1051/MATECCONF/20167010015.

- [107] O. Breitenstein and M. Langenkamp, *Lock-in thermography basics and use for functional diagnostics of electronic components*. 2003.
- [108] E. Kaplani, "Degradation in field-aged crystalline silicon photovoltaic modules and diagnosis using electroluminescence imaging," in *8th International Workshop on Teaching in Photovoltaics*, 2016, pp. 38–41, [Online]. Available: [https://ueaeprints.uea.ac.uk/58215/1/EKaplani\\_PV\\_degradation\\_Electroluminescence\\_IWTPV2016.pdf](https://ueaeprints.uea.ac.uk/58215/1/EKaplani_PV_degradation_Electroluminescence_IWTPV2016.pdf).
- [109] I. Zafirovska, M. K. Juhl, J. W. Weber, O. Kunz, and T. Trupke, "Module inspection using line scanning photoluminescence imaging," in *32nd European Photovoltaic Solar Energy Conference and Exhibition*, 2013, pp. 1826–1829.
- [110] S. Johnston, "Contactless electroluminescence imaging for cell and module characterization," in *42nd Photovoltaic Specialist Conference*, 2015, pp. 1–6.
- [111] M. Sander *et al.*, "Investigations on cracks in embedded solar cells after thermal and mechanical loading," in *27th European Photovoltaic Solar Energy Conference and Exhibition*, 2012, pp. 3188–3193.
- [112] T. Trupke, E. Pink, R. A. Bardos, and M. D. Abbott, "Spatially resolved series resistance of silicon solar cells obtained from luminescence imaging," *Appl. Phys. Lett.*, vol. 90, p. 093506, 2007, doi: 10.1063/1.2709630.
- [113] A. Mansouri, M. Zettl, O. Mayer, M. Lynass, M. Bucher, and O. Stern, "Defect detection in photovoltaic modules using electroluminescence imaging," *27th Eur. Photovolt. Sol. Energy Conf. Exhib.*, pp. 3374–3378, 2012.
- [114] T. Fuyuki, H. Kondo, T. Yamazaki, Y. Takahashi, and Y. Uraoka, "Photographic surveying of minority carrier diffusion length in polycrystalline silicon solar cells by electroluminescence," *Appl. Phys. Lett.*, vol. 86, no. 26, pp. 1–3, 2005, doi: 10.1063/1.1978979.
- [115] T. Trupke, R. A. Bardos, M. D. Abbott, F. W. Chen, J. E. Cotter, and A. Lorenz, "Fast photoluminescence imaging of silicon wafers," in *4th World Conference on Photovoltaic Energy Conversion*, 2006, vol. 1, pp. 928–931, doi: 10.1109/WCPEC.2006.279608.
- [116] T. Fuyuki, H. Kondo, Y. Kaji, A. Ogane, and Y. Takahashi, "Analytic findings in the electroluminescence characterization of crystalline silicon solar cells," *J. Appl. Phys.*, vol. 101, no. 2, pp. 023711-1-023711-5, Jan. 2007, doi: 10.1063/1.2431075.
- [117] T. Potthoff, K. Bothe, U. Eitner, D. Hinken, and M. Köntges, "Detection of the voltage distribution in photovoltaic modules by electroluminescence imaging," *Prog. Photovolt Res. Appl.*, vol. 18, pp. 100–106, 2010, doi: 10.1002/pip.941.
- [118] M. Köntges, M. Siebert, and D. Hinken, "Quantitative analysis of PV-modules by electroluminescence images for quality control," in *European Photovoltaic Solar Energy Conference*, 2009, pp. 3226–3231, [Online]. Available: [http://www.isfh.de/institut\\_solarforschung/files/24eupvsec\\_koentges\\_4co.2.3.pdf](http://www.isfh.de/institut_solarforschung/files/24eupvsec_koentges_4co.2.3.pdf).

## References

- [119] S. Guo, E. Schneller, K. O. Davis, and W. V. Schoenfeld, “Quantitative analysis of crystalline silicon wafer PV modules by electroluminescence imaging,” in *43rd IEEE Photovoltaic Specialists Conference*, 2016, pp. 3688–3692, doi: 10.1109/PVSC.2016.7750365.
- [120] K. Mertens, H. Kösters, and M. Diehl, “Low-cost-outdoor-EL: Cost-efficient extensive on-site quality analysis of solar modules,” in *31st European Photovoltaic Solar Energy Conference and Exhibition*, 2015, pp. 2300–2302.
- [121] “Fladung aerial PV inspection.” <http://www.solartechnik-fladung.de> (accessed Jun. 01, 2020).
- [122] K. Mertens, A. Arnds, G. Behrens, A. Domnik, and F. Bielefeld, “LowCost-outdoor-electroluminescence: Significant improvements of the method,” in *32nd European Photovoltaic Solar Energy Conference and Exhibition*, 2016, pp. 2081–2083.
- [123] A. Gisele *et al.*, “Development of outdoor luminescence imaging for drone-based PV array inspection,” in *44th IEEE Photovoltaic Specialists Conference*, 2017, pp. 2682–2687, doi: 10.1109/PVSC.2017.8366602.
- [124] G. Alves Dos Reis Benatto *et al.*, “Drone-Based Daylight Electroluminescence Imaging of PV Modules,” *IEEE J. Photovoltaics*, vol. 10, no. 3, pp. 872–877, May 2020, doi: 10.1109/JPHOTOV.2020.2978068.
- [125] T. Trupke, R. A. Bardos, M. C. Schubert, and W. Warta, “Photoluminescence imaging of silicon wafers,” *Appl. Phys. Lett.*, vol. 89, pp. 044107-1-044107-3, 2006, doi: 10.1109/WCPEC.2006.279608.
- [126] R. Ebner and B. Kubicek, “Photoluminescence measurement system for thin film modules,” in *31st European Photovoltaic Solar Energy Conference and Exhibition*, 2015, pp. 39–41.
- [127] T. Trupke, B. Mitchell, J. W. Weber, W. McMillan, R. A. Bardos, and R. Kroeze, “Photoluminescence imaging for photovoltaic applications,” *Energy Procedia*, vol. 15, pp. 135–146, 2012, doi: 10.1016/j.egypro.2012.02.016.
- [128] J. A. Tsanakas, L. Ha, and C. Buerhop, “Faults and infrared thermographic diagnosis in operating c-Si photovoltaic modules: A review of research and future challenges,” *Renew. Sustain. Energy Rev.*, vol. 62, pp. 695–709, 2016, doi: 10.1016/j.rser.2016.04.079.
- [129] T. J. Silverman, M. G. Deceglie, K. VanSant, S. Johnston, and I. Repins, “Illuminated outdoor luminescence imaging of photovoltaic modules,” in *44th IEEE Photovoltaic Specialists Conference*, 2017, pp. 3452–3455.
- [130] V. Parra *et al.*, “Implementation of a friendly daylight electroluminescence system for the inspection of solar PV panels,” in *33rd European Photovoltaic Solar Energy Conference and Exhibition*, Nov. 2017, pp. 2021–2025, doi: 10.4229/EUPVSEC20172017-6CO.15.4.
- [131] T. Kropp, M. Berner, L. Stoicescu, and J. H. Werner, “Self-sourced daylight

- electroluminescence from photovoltaic modules,” *IEEE J. Photovoltaics*, vol. 7, no. 5, pp. 1184–1189, Sep. 2017, doi: 10.1109/JPHOTOV.2017.2714188.
- [132] C. Y. Peng, S. Y. Wen, Z. J. Ji, and C. P. Huang, “Non-destructive displaying defects for luminescence image of photovoltaic panel arrays,” in *International Conference on Advanced Robotics and Intelligent Systems*, 2015, pp. 1–4.
- [133] “LumiSolar.” <https://www.environmental-expert.com/products/lumisolar-outdoor-electroluminescence-inspection-system-394889> (accessed Jul. 10, 2017).
- [134] “Sensors Unlimited.” <http://www.sensorsinc.com/applications/photovoltaics/electroluminescence-for-pv-cells> (accessed Jul. 13, 2017).
- [135] “MBJ.” <https://www.mbj-services.com> (accessed Jul. 10, 2017).
- [136] “MRP Energy.” <https://www.mrpenergy.it/en/products/check-up-kit/> (accessed Jul. 10, 2017).
- [137] M. GREEN *et al.*, “Solar cell efficiency tables (version 40),” *IEEE TRANS FUZZY SYST*, vol. 20, no. 6, pp. 1114–1129, 2012, doi: 10.1002/pip.
- [138] J. Schlothauer, S. Jungwirth, M. Kohl, and B. Roder, “Degradation of the encapsulant polymer in outdoor weathered photovoltaic modules: Spatially resolved inspection of EVA ageing by fluorescence and correlation to electroluminescence,” *Sol. Energy Mater. Sol. Cells*, vol. 102, pp. 75–85, 2012, doi: 10.1016/j.solmat.2012.03.022.
- [139] G. B. Alers, J. Zhou, C. Deline, P. Hacke, and S. R. Kurtz, “Degradation of individual cells in a module measured with differential IV analysis,” *Prog. Photovoltaics Res. Appl.*, vol. 19, pp. 977–982, 2011, doi: 10.1002/pip.
- [140] R. A. Sinton and A. Cuevas, “Contactless determination of current–voltage characteristics and minority-carrier lifetimes in semiconductors from quasi-steady-state photoconductance data,” *Appl. Phys. Lett.*, vol. 69, no. 17, p. 2510, 1996, doi: 10.1063/1.117723.
- [141] K. R. McIntosh, “Lumps, humps and bumps: three detrimental effects in the current-voltage curve of silicon solar cells,” PhD Thesis, University of New South Wales, 2001.
- [142] I. L. Eisgruber and J. R. Sites, “Extraction of individual-cell photocurrents and shunt resistances in encapsulated modules using large-scale laser scanning,” *Prog. Photovoltaics Res. Appl.*, vol. 4, no. 1, pp. 63–75, 1996.
- [143] P. Vorasayan, T. R. Betts, and R. Gottschalg, “Limited laser beam induced current measurements: a tool for analysing integrated photovoltaic modules,” *Meas. Sci. Technol.*, vol. 22, no. 8, pp. 085702-1-085702-7, Jun. 2011, doi: 10.1088/0957-0233/22/8/085702.
- [144] T. J. McMahon, T. S. Basso, and S. R. Rummel, “Cell shunt resistance and photovoltaic module performance,” in *25th IEEE Photovoltaic Specialists*

## References

- Conference*, 1996, pp. 1291–1294, doi: 10.1109/pvsc.1996.564369.
- [145] Y. S. Kim, S. M. Kang, B. Johnston, and R. Winston, “A novel method to extract the series resistances of individual cells in a photovoltaic module,” *Sol. Energy Mater. Sol. Cells*, vol. 115, pp. 21–28, Aug. 2013, doi: 10.1016/j.solmat.2013.03.021.
- [146] L. De Bernardez and R. H. Buitrago, “Dark I-V curve measurement of single cells in a photovoltaic module,” *Prog. Photovoltaics Res. Appl.*, vol. 14, no. 4, pp. 321–327, 2006, doi: 10.1002/pip.665.
- [147] M. D. Yandt, J. P. D. Cook, K. Hinzer, and H. Schriemer, “Shutter technique for noninvasive individual cell characterization in sealed CPV modules,” *IEEE J. Photovoltaics*, vol. 5, no. 2, pp. 691–696, Mar. 2015, doi: 10.1109/JPHOTOV.2015.2392943.
- [148] G. Koutsourakis, R. Gottschalg, T. R. Betts, and M. Bliss, “Utilising digital light processing and compressed sensing for photocurrent mapping of encapsulated photovoltaic modules,” in *35th European Photovoltaic Solar Energy Conference and Exhibition*, Nov. 2018, pp. 1065–1071, doi: 10.4229/35THEUPVSEC20182018-5BO.11.6.
- [149] J. C. Blakesley, F. A. Castro, G. Koutsourakis, A. Laudani, G. M. Lozito, and F. Riganti Fulginei, “Towards non-destructive individual cell I-V characteristic curve extraction from photovoltaic module measurements,” *Sol. Energy*, vol. 202, pp. 342–357, May 2020, doi: 10.1016/j.solener.2020.03.082.
- [150] F. Fruehauf and M. Turek, “Quantification of electroluminescence measurements on modules,” *Energy Procedia*, vol. 77, pp. 63–68, Aug. 2015, doi: 10.1016/j.egypro.2015.07.010.
- [151] J. Bauer, F. Frühauf, and O. Breitenstein, “Quantitative local current-voltage analysis and calculation of performance parameters of single solar cells in modules,” *Sol. Energy Mater. Sol. Cells*, vol. 159, pp. 8–19, 2017, doi: 10.1016/j.solmat.2016.08.029.
- [152] A. A. Lacis and J. E. Hansen, “A parameterization for the absorption of solar radiation in the earth’s atmosphere,” *J. Atmos. Sci.*, vol. 31, pp. 118–133, 1974.
- [153] M. K. Juhl and T. Trupke, “The impact of voltage independent carriers on implied voltage measurements on silicon devices,” *J. Appl. Phys.*, vol. 120, no. 16, p. 165702, 2016, doi: 10.1063/1.4965698.
- [154] M. C. Alonso Garcí’a, W. Herrmann, W. Bohmer, and B. Proisy, “Thermal and electrical effects caused by outdoor hot-spot testing in associations of photovoltaic cells,” *Prog. Photovoltaics Res. Appl.*, vol. 11, no. 5, pp. 293–307, 2003, doi: 10.1002/pip.490.
- [155] H. Yang, H. Wang, and M. Wang, “Investigation of the relationship between reverse current of crystalline silicon solar cells and conduction of bypass diode,” *Int. J. Photoenergy*, vol. 2012, no. 57218, pp. 1–5, 2012, Accessed: Jun. 22, 2020. [Online]. Available: <https://www.hindawi.com/journals/ijp/2012/357218/abs/>.

- [156] “Sol 1.7 TE Cooled Linear InGaAs Array Spectrometer.” <https://bwtek.com/products/sol-1-7/> (accessed Jun. 23, 2020).
- [157] “PVEducation.” <https://www.pveducation.org> (accessed Jul. 19, 2020).
- [158] “Xeva-1713.” <https://applied-infrared.com.au/> (accessed Jun. 17, 2020).
- [159] “Bobcat-640-GigE.” [https://applied-infrared.com.au/images/pdf/Bobcat-640-GigE\\_Industrial\\_LowRes.pdf](https://applied-infrared.com.au/images/pdf/Bobcat-640-GigE_Industrial_LowRes.pdf) (accessed Aug. 31, 2020).
- [160] “Pleora iPORT CL-U3 External Frame Grabber.” <https://www.pleora.com/products/frame-grabbers/iport-cl-u3/> (accessed Jun. 17, 2020).
- [161] “LD400 - DC Electronic Load.” <https://au.element14.com/aim-tti-instruments/ld400/dc-load-fixed-80a-80v-400w/dp/2444043> (accessed Jun. 17, 2020).
- [162] “LTSpice XVII User Manual, General Structure and Conventions, Mike Englehardt, Linear Technology Corporation.” 2016, Accessed: Aug. 25, 2018. [Online]. Available: [http://www.ieca-inc.com/images/LTSPICE\\_Manual.pdf](http://www.ieca-inc.com/images/LTSPICE_Manual.pdf).
- [163] L. Hassaine, E. Olias, J. Quintero, and V. Salas, “Overview of power inverter topologies and control structures for grid connected photovoltaic systems,” *Renew. Sustain. Energy Rev.*, vol. 30, pp. 796–807, 2013, doi: 10.1016/j.rser.2013.11.005.
- [164] R. Fu, D. J. Feldman, R. M. Margolis, M. A. Woodhouse, and K. B. Ardani, “US solar photovoltaic system cost benchmark,” 2017. Accessed: Aug. 24, 2018. [Online]. Available: [www.nrel.gov/publications](http://www.nrel.gov/publications).
- [165] “5B - Solar Reinvented.” <https://5b.com.au/> (accessed Jul. 19, 2020).
- [166] “Solar inverter | SUNNY BOY | SMA Solar.” <https://www.sma-australia.com.au/products/solar-inverters/sunny-boy-30-36-40-50-60.html> (accessed Jun. 26, 2020).
- [167] “Power optimizer | Tigo TS4-O.” <https://www.tigoenergy.com/products/> (accessed Jun. 26, 2020).
- [168] “Solar inverter | Suzhou Universal-Power | UNIV-M248 .” <https://www.enfsolar.com/pv/inverter-datasheet/7457> (accessed Jun. 24, 2020).
- [169] D. Hinken, C. Schinke, S. Herlufsen, A. Schmidt, K. Bothe, and R. Brendel, “Experimental setup for camera-based measurements of electrically and optically stimulated luminescence of silicon solar cells and wafers,” *Rev. Sci. Instrum.*, vol. 82, no. 3, 2011, doi: 10.1063/1.3541766.
- [170] D. Chung, “Applications of photoluminescence imaging of silicon bricks Thesis / Dissertation Sheet,” no. October, 2018.
- [171] “High Performance SWIR Imaging Cameras.” <https://www.raptorphotonics.com/wp-content/uploads/2015/10/Ninox-White->

## References

- Paper-Final.pdf (accessed Oct. 14, 2020).
- [172] “SPIRE module flash tester.” <http://www.eternalsunspire.com> (accessed Mar. 05, 2020).
- [173] “6675A DC power supply.” <https://www.keysight.com/en/pd-839263-pn-6675A/2000-watt-power-supply-120v-18a> (accessed Mar. 05, 2020).
- [174] M. García, L. Marroyo, E. Lorenzo, J. Marcos, and M. Pérez, “Observed degradation in photovoltaic plants affected by hot-spots,” *Prog. Photovoltaics Res. Appl.*, vol. 22, pp. 1292–1301, 2014, doi: 10.1002/pip.2393.
- [175] J. Wong, “Griddler: Intelligent computer aided design of complex solar cell metallization patterns,” *Conf. Rec. 39th IEEE Photovolt. Spec. Conf.*, pp. 933–938, 2013.
- [176] R. Dumbrell, M. K. Juhl, T. Trupke, and Z. Hameiri, “Comparison of terminal and implied open circuit voltage measurements,” *IEEE J. Photovoltaics*, vol. 7, pp. 1376–1383, 2017, doi: 10.1109/JPHOTOV.2017.2729889.
- [177] “Sunswift.” <https://www.sunswift.com/> (accessed Jul. 07, 2020).
- [178] “SunPower Maxeon Gen III Solar Cells.” <https://us.sunpower.com/solar-resources/sunpower®-maxeon™-gen-iii-solar-cells> (accessed Sep. 16, 2020).
- [179] I. Zafirovska, M. K. Juhl, A. Ciesla, R. Evans, and T. Trupke, “Low temperature sensitivity of implied voltages from luminescence measured on crystalline silicon solar cells,” *Sol. Energy Mater. Sol. Cells*, vol. 199, pp. 50–58, 2019, doi: 10.1016/j.solmat.2019.04.009.
- [180] S. Spataru, D. Sera, T. Kerekes, and R. Teodorescu, “Monitoring and fault detection in photovoltaic systems based on inverter measured string I-V curves,” in *31st European Photovoltaic Solar Energy Conference and Exhibition*, 2015, pp. 1667–1674, doi: 10.4229/EUPVSEC20152015-5BO.12.2.
- [181] “SCHOTT KG-3 heat absorbing glass.” <https://www.edmundoptics.com.au/p/50mm-dia-kg-3-heat-absorbing-glass/9441/> (accessed Mar. 05, 2020).
- [182] “SR570 - Low noise current preamplifier.” <https://www.thinksrs.com/products/sr570.html> (accessed Mar. 05, 2020).
- [183] “Measurement Computing USB-1808.” <https://www.mccdaq.com/data-acquisition-and-control/simultaneous-daq/USB-1808-Series.aspx> (accessed Mar. 05, 2020).
- [184] R. A. Sinton, D. De Ceuster, K. Wilson, and L. R. Barbosa, “Flash testing high-efficiency silicon solar cells and modules,” 2005.
- [185] M. J. Kerr, A. Cuevas, and R. A. Sinton, “Generalized analysis of quasi-steady-state and transient decay open circuit voltage measurements,” *J. Appl. Phys.*, vol. 91, no. 1, pp. 399–404, 2002, doi: 10.1063/1.1416134.



- [186] T. Trupke and R. A. Bardos, “Self-consistent determination of the generation rate from photoconductance measurements,” *Appl. Phys. Lett.*, vol. 85, no. 16, pp. 3611–3613, 2004, doi: 10.1063/1.1807961.
- [187] Hugo Silva, “PID and LID: Devastating phenomena for PV plants.” <https://sinovoltaics.com/quality-control/pid-lid-devastating-phenomena-pv-plants/> (accessed Feb. 02, 2019).
- [188] D. Bredemeier, D. Walter, S. Herlufsen, and J. Schmidt, “Understanding the light-induced lifetime degradation and regeneration in multicrystalline silicon,” *Energy Procedia*, vol. 92, no. 0, pp. 773–778, 2016, doi: <http://dx.doi.org/10.1016/j.egypro.2016.07.060>.
- [189] R. Sinton and A. Cuevas, “A quasi-steady-state open-circuit voltage method for solar cell characterization,” in *16th European Photovoltaic Solar Energy Conference*, 2000, no. 1152, pp. 1–4, doi: citeulike-article-id:6901946.
- [190] M. Wolf and H. Rauschenbach, “Series resistance effects on solar cell measurements,” *Adv. Energy Convers.*, vol. 3, pp. 455–479, 1963, doi: 10.1016/0365-1789(63)90063-8.
- [191] O. Kunz, “Evaporated solid-phase crystallised poly-silicon thin-film solar cells on glass,” PhD Thesis, University of New South Wales, 2009.
- [192] Z. Hameiri, K. McIntosh, and G. Xu, “Evaluation of recombination processes using the local ideality factor of carrier lifetime measurements,” *Sol. Energy Mater. Sol. Cells*, vol. 117, pp. 251–258, 2013, doi: 10.1016/j.solmat.2013.05.040.
- [193] Z. Hameiri and K. R. McIntosh, “On the use of local ideality factor obtained from effective carrier lifetime measurements,” in *39th IEEE Photovoltaic Specialists Conference*, 2013, pp. 1412–1416, doi: 10.1109/PVSC.2013.6744408.
- [194] F. Hernando, R. Gutierrez, G. Bueno, F. Recart, and V. Rodriguez, “Humps, a surface damage explanation,” in *2nd World Conference on Photovoltaic Solar Energy Conversion*, 1998, pp. 1321–1323.
- [195] “Texas instruments LM35.” <http://www.ti.com/product/LM35> (accessed Mar. 05, 2020).